A Search for Charged Massive Long-lived Particles Using DØ Detector

by

Yunhe Xie

M. Sc. in Physics, Brown University, 2004

B. Sc in Physics, Zhejiang University, China, 2001

A dissertation submitted in partial fulfillment of the requirements for the

Degree of Doctor of Philosophy

in the Physics Department at Brown University

PROVIDENCE, RHODE ISLAND, U.S.A.

May 2009

This dissertation by Yunhe Xie is accepted in its present form by

the Physics Department as satisfying the

dissertation requirements for the degree of

Doctor of Philosophy

Date ....

Professor David Cutts, Advisor

Recommended to the Graduate Council

Date ....

Professor Greg Landsberg, Reader

Date ....

Professor Meenakshi Narain, Reader

Date ....

Professor Chung-I Tan, Reader

Approved by the Graduate Council

Date ....

Sheila Bonde, Dean of the Graduate School

Vitae

Yunhe Xie received Bachlor of Science degree with honor in Physics at Zhejiang University in 2001. In the same year, she started doctoral studies at Brown University. In 2004, she received her Master's of Science degree in Physics.

Acknowledgments

First of all, I want to thank my adviser, Prof. Dave Cutts, for his precious support and tireless guidance. Without his constant supervision, I cannot finish my graduate studies neither this work successfully. I appreciate all the skills and knowledge that I have learned from him, and I believe those will continue to benefit me in my future. I also extend my appreciation specially to Dr. Tulika Bose, who was our post-doc and now joins Boston University as a faculty. With her tremendous help and guidance, I can complete this analysis now.

Secondly, my appreciation to my committee members, Prof. Greg Landsberg, Prof. Meenakshi Narain, and Prof. Chung-I Tan. Thanks for their patience to share their time reading my manuscripts and provides valuable advices for further improvements. Special thanks to Greg and Meenakshi for offered lectures, which not only are the introductions to the field but also provide solid background knowledge in physics and experimental apparatus.

Thirdly, many thanks to my close colleagues who also involved in this research - Mike Eads, Sudeshna Banerjee, and Tulika Bose. Special thanks to dear Jean-Francois Grivaz for his great advise on the physics models. The same to the New Phenomena group members, all members in the Editorial Board 20, our physics conveners, spokenpersons, and those colleagues who shared their suggestions. Without their comments and suggestions, we cannot have our paper accepted so quickly.

Also, I would like to show my respects to all the L3 Data Acquisition development team. It has been a very nice and enjoyful experience to work with you together: Douglas Chapin, Sean E.K. Mattingly, Aran Garcia-Bellido, Gordon Watts, Thomas Gadfort, Andy Haas, Gustaaf Broijmans, John BackusMayes, and of course our Tulika and Dave.

I would also like to thank all the post-docs and students in our Brown group: Brendan Casey, Yuji Enari, Hwi-Dong Yoo, Monica Pangilinan, Duong Nguyen, Aram Avetisyan, and Patrick Tsang. It also has been a delightful experience working with the undergraduate students in our group: John Keller, Nikolas Logan, Erin Teich, and Miriam Klein.

Many thanks to the friends I got to know in Fermilab: Junjie Zhu, Jun Guo, Shaohua Fu, Yanjun Tu, Huishi Dong, Feng Guo, Chun Xu, Zhenyu Ye, Tingjun Yang, Chunlei Liu, Zhiyi Liu, and Yuan Hu. The same goes to all my friends and classmates in Brown, Weifeng Shen, Yanqiu Li, Lei Wang, Dapeng Wang, Liuliu Li, Yanhu Wei and his wife, etc. Sorry that I cannot mention all their names

here, because it will be really long list, like our authorlist in DØ. With all of them, my stay in both Fermilab and Providence turns to a lot more enjoyable and delightful.

Finally I would like to thank my family and my husband Kongbin. Without their deep love and continuous support, I would not be able to complete this work at this time.

Contents

List of Figures

Chapter 1

Introduction to Standard Model

There are four kinds of forces that govern the interactions between the elementary particles that make up the universe. These four fundamental forces are known as the gravitional, electromagnetic, weak, and strong forces. The gravitational forces dominate the interactions over long distances and large masses, e.g. at the astronomical scale.

The Standard Model (SM) of particle physics is a quantum field theory that currently describes the elementary particles and the interactions best. Three out of the above four fundamental forces - the electromagnetic, weak, and strong forces - are incorporated and unified under the Glashow-Weinberg-Salam model. The Standard Model theory [1, 2] is based on gauge symmetry $SU(3)_C \times SU(2)_L \times U(1)_Y$. $SU(3)_C$ is the symmetry group describing strong interactions. Here C refers to color, L refers to weak isospins, and Y is weak hypercharge, all of which will be detailed in the following sections. $SU(2)_L \times U(1)_Y$ is the symmetry for electroweak interactions, while $U(1)_{em}$, as the electromagnetic interaction symmetry group, is a subset of $SU(2)_L \times U(1)_Y$ symmetry in Standard Model. This can be considered a unification of the electromagnetic interactions with the weak interactions. Standard Model theory has been proved to be successful since the experimental measurements have high precise agreements with the predictions of the Standard Model.

However, the Standard Model is not a complete fundamental theory, due to the fact that it does not include gravity. Also, the recent observation of the neutrino oscillations shows incompatibility with the Standard Model predictions. Furthermore, in Standard Model theory, there are 19 free parameters, whose values need to be finely tuned, rather than being derived from first principles. Therefore, various theories have been developed as extensions of the Standard Model. Many exten-

sions are built based on the gauge structure of the Standard Model and expanded to larger groups. We will discuss several such models in Chapter 2.

1.1 History

The Standard Model was originated in the early 70's and has been well established through the decades since then. In the Standard Model, the unification of the electromagnetic and weak forces was discovered by Sheldon Glashow [3] in 1963. The modern form of the Standard Model was refined by the further incorporation of the Higgs mechanism by Steven Weinberg [4] and Abdus Salam [5] in 1967. This Higgs mechanism is the origin of the masses for all the fundamental fermions in the Standard Model.

1.2 Particles in Standard Model

The Standard Model, which provides the best current understanding of the nature of the fundamental particles and their interactions, will be introduced in this chapter. In the standard model, the fundamental particles in universe are divided into two categories: *fermions* (leptons and quarks) and *bosons* (gauge bosons and Higgs bosons).

1.2.1 Fermions

In the Standard Model framework, fermions are the elementary particles making up the known world. They carry half-integer spin, and hence follow the Pauli Exclusion Principles. Fermions are classified further into two categories: quarks and leptons. Each fermion has the same $\frac{1}{2}$-spin and mass, and opposite electric charge, as its corresponding anti-particle.

Leptons

There are six known leptons: electron (e), electron neutrino (ν_e), muon (μ), muon neutrino (ν_μ), tau (τ), and tau neutrino (ν_τ), with their charges and masses listed in Table 1.1.

Generation	Particle	Symbol	Charge (e)	Mass (MeV)
First	electron	e	-1	0.511
	electron neutrino	ν_e	0	<0.000002
Second	muon	μ	-1	105.7
	muon neutrino	ν_μ	0	<0.19
Third	tau	τ	-1	1777
	tau neutrino	ν_τ	0	<18.2

Table 1.1: Leptons of the Standard Model.

Leptons are grouped into three families/generations, where the corresponding particles in the different generations have similar properties with different masses. The first generation includes the electron (e) and electron neutrino (ν_e); the second generation includes the muon (μ) and muon neutrino (ν_μ); and the third generation includes the tau (τ) and tau neutrino (ν_τ). Leptons carry integer charges, either $-e$ or 0, where $-e$ is the charge of the electron. Each lepton family has an additional lepton quantum number, which is L_e, L_μ, and L_τ, respectively. The third component of this lepton quantum number is denoted as T^3 or I_3.

Quarks

Quarks can interact through the electromagnetic, weak and strong forces. There are six "flavors" of quarks: up (*u*), down (*d*), charm (*c*), strange (*s*), top (*t*), and bottom (*b*), as listed in Table 1.2. The flavor, as a quantum number, is conserved in strong and electromagnetic interactions; however, it can be changed in weak interactions.

Generation	Particle	Symbol	Charge (e)	Mass (MeV)
First	up	*u*	$+2/3$	1.5 ~ 3.3
	down	*d*	$-1/3$	3 .5~ 6.0
Second	charm	*c*	$+2/3$	1270
	strange	*s*	$-1/3$	104
Third	top	*t*	$+2/3$	1712
	bottom	*b*	$-1/3$	4200

Table 1.2: Quarks of the Standard Model.

Quarks are also grouped into three families/generations similar to leptons. The first generation includes the up (*u*) and down (*d*) quarks; the second generation includes the charm (*c*) and strange (s) quarks; and the third generation includes the top (*t*) and bottom (*b*) quarks. Quarks carry fractional charges, either $\frac{2}{3}e$, or $-\frac{1}{3}e$, where $-e$ is the charge of the electron. Beside the six "flavors" of the quarks, each quark also has a weak-hypercharge (Y), and a weak isospin (I). Furthermore, there are three kinds of color (*red*, *green*, and *blue*), which is the quantum number associated with the strong force. The "color" is a gauge $SU(3)$ symmetry.

Six quarks and their anti-particles can combine in particle-antiparticle pairs to form mesons, or in particle/anti-particle triplets to form baryons. In this way, all of the known hadrons can be constructed. Protons and neutrons are uud and udd bound states, respectively. The quantum number "color" allows the existence of baryons containing three quarks of the same flavor with parallel spins.

1.2.2 Bosons

The fermions interact with each other by exchanging the fundamental spin-1 bosons, which obey Bose-Einstein statistics.

Gauge bosons

In the Standard Model, three forces are contained - electromagnetic, weak, and strong - and different bosons are associated with each one separately. The electroweak theory is the unification of the electromagnetic theory and the weak theory. Both electroweak and strong theories are gauge field theories, in which the forces between fermions are modeled by their coupling to the mediating bosons. Because the Lagrangian of each mediating boson is invariant under gauge transformation, the mediating bosons are called gauge bosons.

The photon (γ) mediates the electromagnetic forces between electrically charged particles. It is massless and well-described in quantum electrodynamic theory.

The $W^{\pm}$ and Z^0 gauge bosons mediate the weak force between particles with different flavors (both quarks and leptons). The $W^{\pm}$ are involved in the weak interactions among left-handed particles and right-handed anti-particles, and participate the electromagnetic interactions, since the Ws

carry the electric charge $+e$ or $-e$. The electrically-neutral Z boson, which has a larger mass than $W^{\pm}$, interacts with both left-handed particles and anti-particles. The weak interactions are mediated by the $W^{\pm}$ and Z^0 gauge bosons as well as by the photons.

The strong force is mediated by the eight massless gluons (g) between color charged particles (quarks). The gluons must be "bi-colored", since color is always conserved. Due to their effective color charges, gluons then can interact with each other directly. The theory of quantum chromodynamics describes the gluons and their interactions, which are more complicated and richer than electrodynamics.

Mediator	Interaction	Charge (e)	Mass (GeV)
Gluon (g)	Strong	0	0
W^+	Weak	1	80.398 ± 0.025
W^-		-1	80.398 ± 0.025
Z^0		0	91.188 ± 0.002
Photon (γ)	EM	0	0

Table 1.3: Gauge bosons in Standard Model.

Higgs boson

The Higgs particle is a hypothetical scalar elementary particle with a mass predicted by the SM to be in the range of 115 – 190 GeV. It is the only fundamental particle that has not yet been directly observed through any experiments. It has zero intrinsic spin, and hence is classified as a boson, like force mediating particles with integer spin number (mainly gauge bosons).

The Higgs boson plays the key role in the Standard Model in explaining the origins of the mass of other elementary particles, especially the difference between the massless photon and the massive W and Z bosons. The Higgs mechanism is responsable for the mass of the fermions, and introduces a new scalar field; and through its interactions with the W and Z bosons, it gives those bosons their masses. The Higgs mechanism explicitly provides the electroweak symmetry breaking. However, there have been no experiments so far providing evidence of the existence of the Higgs boson, either directly or indirectly, which leaves the Higgs boson the only undiscovered particle predicted by the Standard Model.

1.2.3 Quantum Electrodynamics (QED)

The quantum theory of electrodynamics with corresponding $U(1)$ symmetry, was first proposed by P. A. M. Dirac in 1920s, and then perfected by Tomonaga, Feynman, and Schwinger in the 1940s. It is the oldest, simplest and most successful of the dynamical theories. It describes the forces between leptons as mediated by photons. The strength of the electromagnetic force is set by the coupling constant

$$g_e = e\sqrt{4\pi/\hbar c} = \sqrt{4\pi\alpha} \tag{1.1}$$

where e is the charge of the positron.

Leptons are represented in a four-component wave function in QED. Taking a free electron as an example, it has two spin substates, $J_z = \pm\frac{1}{2}\hbar$. Each spin substate has both positive and negative energies, while the negative energies should be interpretated as the corresponding anti-particles. The anti-particle of the electron is the positron, which was discovered in 1932.

The Lagrangian of a free Dirac field Ψ for a fermion with mass m, is:

$$\mathcal{L} = \bar{\Psi}\left(i\gamma^\mu\partial_\mu - m\right)\Psi \tag{1.2}$$

where γ^μ are the Dirac Matrices. This is unchanged under $U(1)$ transformation, and the invariance under local gauge transformation introduces the vector field A_μ, which is identified with the photon. Adding the kinematic term of the propagation of the vector field gives the total Lagrangian as:

$$\mathcal{L} = \bar{\Psi}\left(i\gamma^\mu D_\mu - m\right)\Psi - \frac{1}{4}F_{\mu\nu}F^{\mu\nu} \tag{1.3}$$

where $D_\mu \equiv \partial_\mu + iqA_\mu$ is the covariant derivative, and $F_{\mu\nu} = \partial\mu A_\nu - \partial_\nu A_\mu$ is added to make A^μ a dynamic variable of the Lagrangian. The gauge field (photon) is required to be massless, in order to preserve the invariance under local gauge transformations. This prediction of massless photon is consistent with the experiment results.

One important feature of the QED is the renormalizibility.

1.2.4 Quantum Chromodynamics (QCD)

As the QED describes the interactions of charged particles, the quantum chromodynamics (QCD) describes the interactions of the colored particles. In colored quark model, there are three colors coming with each flavor of the quark, red, $green$, and $blue$. Although each flavor carries different mass, the three colors of a given flavor have the same weight. The strength of the chromodynamic forces is set by the "strong" coupling constant

$$g_s = \sqrt{4\pi\alpha_s} \tag{1.4}$$

where the g_s can be treated as the unit of color, similar to g_e as the fundamental unit of charge in QED. This coupling constant, however, will change with the energy scale.

The three colors of the quark can be denoted as R, G, and B, for red, $green$, and $blue$, respectively. Then the anti-quarks will be represented symbolically with complementary colors, $\bar{R}$, $\bar{G}$, and $\bar{B}$. All particles are observed as "colorless", which means that the wave functions of the particles are invariant under $R-G-B$ rotations. Baryons are the bound states of triple quarks with different colors, and mesons are the bond states of a quark and an anti-quark with color and complementary color. The fundamental representation of a $SU(3)$ symmetry is a triplet consisting of three color charges of the quarks for $SU(3)_C$ in QCD. In this representation, the Gell-Mann "λ-matrices" are denoted as λ_i, $i = 1, 2...8$,

$$\lambda^1 = \begin{pmatrix} 0 & 1 & 0 \\ 1 & 0 & 0 \\ 0 & 0 & 0 \end{pmatrix}, \lambda^2 = \begin{pmatrix} 0 & -i & 0 \\ -i & 0 & 0 \\ 0 & 0 & 0 \end{pmatrix}, \lambda^3 = \begin{pmatrix} 1 & 0 & 0 \\ 0 & -1 & 0 \\ 0 & 0 & 0 \end{pmatrix},$$

$$\lambda^4 = \begin{pmatrix} 0 & 0 & 1 \\ 0 & 0 & 0 \\ 1 & 0 & 0 \end{pmatrix}, \lambda^5 = \begin{pmatrix} 0 & 0 & -i \\ 0 & 0 & 0 \\ i & 0 & 0 \end{pmatrix}, \lambda^6 = \begin{pmatrix} 0 & 0 & 0 \\ 0 & 0 & 1 \\ 0 & 1 & 0 \end{pmatrix},$$

$$\lambda^7 = \begin{pmatrix} 0 & 0 & 0 \\ 0 & 0 & -i \\ 0 & i & 0 \end{pmatrix}, \lambda^8 = \sqrt{\tfrac{1}{3}} \begin{pmatrix} 1 & 0 & 0 \\ 0 & 1 & 0 \\ 0 & 0 & -2 \end{pmatrix}.$$

The three color charges are the eigenvector simultaneously for the diagonal matricesλ^3 and λ^8, which are:

$$R = \begin{pmatrix} 1 \\ 0 \\ 0 \end{pmatrix} \quad B = \begin{pmatrix} 0 \\ 1 \\ 0 \end{pmatrix} \quad G = \begin{pmatrix} 0 \\ 0 \\ 1 \end{pmatrix} \tag{1.5}$$

Then the eight massless mediating vector gluons are in the "color octet":

$$\left\{ \begin{array}{cc} \sqrt{\frac{1}{2}}\left(R\bar{B} + B\bar{R}\right), & -i\sqrt{\frac{1}{2}}\left(R\bar{G} - G\bar{R}\right) \\ -i\sqrt{\frac{1}{2}}\left(R\bar{B} - B\bar{R}\right), & \sqrt{\frac{1}{2}}\left(B\bar{G} + G\bar{B}\right) \\ \sqrt{\frac{1}{2}}\left(R\bar{R} - B\bar{B}\right), & -i\sqrt{\frac{1}{2}}\left(B\bar{G} - G\bar{B}\right) \\ \sqrt{\frac{1}{2}}\left(R\bar{G} + G\bar{R}\right), & \sqrt{\frac{1}{6}}\left(R\bar{R} + B\bar{B} - 2G\bar{G}\right) \end{array} \right\} \tag{1.6}$$

There is a remaining "color singlet":

$$\sqrt{\frac{1}{3}}\left(R\bar{R} + B\bar{B} + G\bar{G}\right) \tag{1.7}$$

which is "colorless" and thus cannot mediate the strong forces in the color change interactions.

The strong force between quarks does not diminish in strength after the limiting space (in size of a hadron) is reached. This phenomenon is called "color confinement" in QCD, which implies that only hadrons can be observed. No single free quark has been observed and agrees with many free quark search results in experiments.

1.2.5 Weak Interactions

The weak interactions are mediated by the massive vector bosons, the Ws ($W^{\pm}$) and the Z^0, unlike the massless photons and gluons. Analogous to the coupling constants in QED and QCD, the weak coupling constant (for interactions mediated by the Ws) is

$$g_w = \sqrt{4\pi\alpha_w} \tag{1.8}$$

With the observed muon lifetime and mass, there is

$$G_F/(\hbar c)^3 = \frac{\sqrt{2}}{8}\left(\frac{g_w}{M_W c^2}\right)^2 = 1.166 \times 10^{-5}\ GeV^2 \tag{1.9}$$

Combined with the measured M_W, we can derive $g_w = 0.66$. Thus, the weak fine structure constant is

$$\alpha_w = \frac{g_w^2}{4\pi} = \frac{1}{29} \tag{1.10}$$

Note that this number is almost five times larger than the electromagnetic fine structure constant which is $\alpha = \frac{1}{137}$. The term "weak" does not come from the coupling constant value (which is actually large), but from the fact that experimentalists used to work at energy scale far below the masses of the force mediators (Ws and Z). Now the high energy machines run at energies close to or even much higher (like LEP, Tevatron and LHC) than $M_W c^2$, and the weak interactions are far beyond the electromagnetic interactions in strength.

The electromagnetic and weak interactions are unified in the electroweak theory. At low energy scale, they appear as two distinct types of forces. However, they combine into the electroweak forces, when reaching or above the unification energy ($\mathcal{O}(10^3\, GeV)$). The electric charge in $U(1)$ group is correlated with the hypercharge Y by

$$Q = I_3 + \frac{Y}{2} \tag{1.11}$$

The weak isospin and hypercharge are conserved, when the Lagrangian keeps invariant under the local gauge transformation $SU(2)_L \times U(1)_Y$. The $SU(2)_L$ term stands for the weak group symmetry, and the index L comes from the fact that the weak bosons only couple to the left-handed fermions. This term must be preserved when the isospin triplet of the weak currents is constructed. Then the $U(1)_Y$ term (the electromagnetic group generator) must be modified in order to represent the right-handed interactions as shown in Eq. 1.11.

The weak coupling constants are related to the electromagnetic coupling constant by the fundamental parameter "weak mixing angle" or Weinberg angle, θ_w as:

$$g_w = \frac{g_e}{\sin\theta_w}, \qquad g_z = \frac{g_e}{\sin\theta_w \cos\theta_w} \tag{1.12}$$

The value of the mixing angle is determined from experiment giving the result $\theta_w = 28.7$. The

masses of the Ws and Z are related by

$$M_W = M_Z \cos\theta_w \tag{1.13}$$

In the low energy scale, the masses of the bosons can be written as

$$M_{W^\pm} = \left(\frac{\sqrt{2}g^2}{8G_F}\right)^{1/2} = \left(\frac{\sqrt{2}e^2}{8G_F \sin^2\theta_w}\right)^{1/2} \tag{1.14}$$

$$M_Z^2 = \frac{M_W^2}{\rho \cos^2\theta_w} \tag{1.15}$$

$$M_\gamma = 0 \tag{1.16}$$

where G_F is the Fermi constant, and ρ is a factor which is observed to be 1 by all experiments to date.

However, the fundamental vector bosons are massless isovector triplets $W_\mu^i (i = 1,\ 2,\ 3)$ for the weak group and massless isosinglet B_μ for electromagnetic group. Spontaneous symmetry breaking (SSB) gives rise to the masses of the weak gauge bosons. This mechanism will automatically add a mass term to the Lagrangian, and break the gauge invariance. The consequence of this symmetry breaking is the new Higgs particle field, which is an isospin doublet of scalar particles and its self-interaction explains the masses of the weak bosons. Three bosons (W_μ^+, W_μ^-, and Z_μ^0) require masses, while one (A_μ, the photon) remains massless.

Yukawa interaction describes the coupling between the Higgs fields and massless quark and lepton fields. The fermions require masses proportional to the vacuum expectation value of the Higgs field through spontaneous symmetry breaking.

1.2.6 The Challenges

Although the predictions of the Standard Model have shown excellent agreement with the high energy physics experiments to high precision, it still is an incomplete theory. First of all, the Standard Model does not describe gravity, which is also a known fundamental force and dominates in the

macroscopic world. Secondly, it does not provide the origins of the fermion mass. The prediction of the Standard Model is not compatible with the recent observation of neutrino oscillations in experiments, which is the evidence that neutrinos have masses. Thirdly, the unification of the strong and electroweak interactions does not happen in its framework. Forthly, there are 19 arbitrary parameters, whose values are chosen to fit data instead of being derived from first principles.

Besides the above limitations, there are two more problems that the Standard Model cannot solve. One problem is the "hierarchy problem". The energy scales of various interactions in the SM are: $O(1GeV/c^2)$ for QCD (~M_{proton}), $O(100GeV/c^2)$ for electroweak (~$M_{W^{\pm},Z^0}$), and $O(10^{19}GeV/c^2)$ for the Planck mass ($M_{Planck} = \sqrt{\hbar c/G}$). The "hierarchy problem" in particle physics is technically a question about why the Higgs boson (a few hundred GeV) is much lighter than the Planck mass.

The other problem still existing in Standard Model is the "fine tuning" problem. The scalar Higgs boson is the source of spontaneous symmetry breaking in Standard Model and gives masses to the other particles. However, the scalar Higgs boson mass diverges quadratically in perturbation theory. The Higgs boson mass is:

$$m_H^2 = m_0^2 + \Delta m_H^2 \approx m_0^2 - g^2\Lambda^2 \tag{1.17}$$

to the lowest order in perturbation theory, where m_H is the scalar Higgs boson mass, m_0 is the "ground" Higgs boson mass parameter, g is a dimensionless coupling constant, and Λ is the energy scale. Compared with the recent empirically measured electroweak scale, the Higgs boson mass, m_H, should be of the same order. Assuming that $g \approx 1$ and Λ is in Planck mass scale, then m_0 must be finely adjusted so that the two terms in 1.17 should cancel to leave $m_0^2 - g^2\Lambda^2 \approx m_H^2 \sim O(10^4(GeV/c^2)^2)$. This means that a precise adjustment should be made on SM parameters, which is unnatural.

Chapter 2

Beyond the Standard Model

The Standard Model theory is not a complete theory in spite of all the success it has. As mentioned in the last chapter, gravity as one of the four fundamental forces is not described in the Standard Model. The origin of the quark and lepton masses is not explained either, nor the existence of the three families. Besides, the Standard Model will have to be extended in order to describe the physics at higher energies. Clearly, when quantum gravitational effects become important, a new framework should be developed at the reduced Planck scale $M_P = \sqrt{8\pi G_{Newton}} = 2.4 \times 10^{18}\, GeV$.

2.1 Physics Beyond The Standard Model

The incompleteness and the unsatisfactory features of the Standard Model motivate both new theories and experimental searches for physics beyond. Several areas are the focus of the physics beyond the Standard Model as listed:

- The hierarchy problem
- The dark matter and dark energy problem
- The cosmological constant problem
- The strong CP problem

In addition, there are attempts at interpretting different phenomena and parameters with more fundamental theories, e.g. gauge coupling unification, theory of quark masses and their mixings, theory

of neutrino masses and their mixings. We review several popular theories among many of those describing the physics beyond the Standard Model.

2.1.1 Supersymmetry

Supersymmetry (SUSY) [6] relates the bosons with the fermions in the Standard Model. Each particle in SM has a supersymmetric partner with a difference 1/2 in spin, while all other quantum numbers remaining the same. SUSY solves the hierarchy problem gracefully without any fine-tuning. In SUSY, the scalar mass term is never generated by quantum corrections. Then a SUSY theory is free from quadratic divergences. If SUSY is the solution to the naturalness problem, it must be an approximate symmetry above TeV scale. This is possible when SUSY is softly broken by terms which do not introduce quadratic divergences. The soft terms provide gauge-invariant masses to all supersymmetric partners of the known SM particles. The details will be discussed in sect. 2.2.

2.1.2 Strong Dynamics

The Higgs bosons help to introduce the electroweak symmetry breaking in the Standard Model. However, there is an alternative way to introduce spontaneous symmetry breaking without a scalar Higgs field. In these models, there is a larger number of fermion fields instead and a larger gauge group involved. This larger gauge group will spontaneously break down to the Standard Model group. The general idea is that the electroweak symmetry breaking is carried by the strong interactions. In these models, a dynamics similar to that in QCD is used to explain the rise of the masses of the W and Z bosons. This QCD-like theory at the higher energy scale gives the observed masses of the W and Z bosons. Technicolor theory is one of these models.

2.1.3 Grand Unified Theory

Grand Unified Theory (GUT) predicts that at the very high energy scale, the electromagnetic, the weak, and the strong forces will integrate into one single unified field. The gauge coupling strengths of QCD, the weak, and the electromagnetic (hypercharge) interactions seem to meet at the common length scale, the GUT scale, which is about $10^{16}\ GeV$. This numerical observation is called gauge

coupling unification, which works particularly well with the existence of the SUSY particles.

The simplest GUT representative is based on the $SU(5)$ gauge group, which is called the Georgi-Glashow model and was proposed by Howard Georgi and Sheldon Glashow. In this model, the $SU(3) \times SU(2) \times U(1)$ are combined. However, the predicted proton decay rate is inconsistant with the experimental observations, which rule out the $SU(5)$ model. More complicated models with longer proton lifetimes are constructed based on the $SU(5)$ because of its elegance. The most promising candidate is $SO(10)$, which contains no additional fermions besides the Standard Model fermions and the right-handed neutrinos. Each generation is unified into a single irreducible representation. Another candidate is the E_6 group, which contains $SO(10)$ and is significantly more complicated.

There are several interesting objects such as the monopoles, cosmic strings, etc., which are predicted by the GUT models but not observed. This is known as the monopole problem in cosmology.

2.1.4 Extra Dimensions

There have been hypotheses that extra dimensions exist beyond the normal four-dimensional world we live in. Extra dimension theories and models are developed to unify the fundamental forces, gravity and the electromagnetic forces. In those models, the normal four-dimensional gauge theories will be localized in higher dimensional spaces, and it is possible to localize gravity as well.

- Kalauz-Klein theory

  The theory was first published in 1921, when Kalauz and Klein [7, 8] attempted to unify gravity and electromagnetic forces in a five-dimensional spacetime. In this theory, the extra dimension must have a much smaller size than the wavelength of the observed particles, which keeps the extra dimension hidden from observation to date. Combined with the experimental observations, we can conclude that the extra dimension, in which the ordinary matter or gauge bosons can propagate, must have an extremely small size in the order of $10^{-30}\ cm$ or less.

- Large extra dimensions

  Arkani-Hamed, Dimopoulos, and Dvali [9] proposed a theory in which the Standard Model fields live on a plane embedded in 2 to 6 extra dimensions. Ordinary particles will not propagate in the extra dimensions so that the usual direct boundary conditions cannot be applied.

However, gravitational effects could provide the constraints. In this theory, the size of the extra dimensions could be as large as $1\ mm$. At scales smaller than the extra dimensions, gravity becomes much stronger, which allows for the possibility of identifying the scale where gravity is close to the weak scale. The smallest distance is $\sim 10^{-19}\ cm$, probed at the energetic Fermilab Tevatron $p\bar{p}$ collider by studying the products of the particles' collision. However, the gravitational interactions between the particles involved in the collisions are very weak because of their light masses. Studies have been carried out in both CDF and DØ and no evidence has been found so far for extra dimensions.

- Wrapped extra dimensions

  So far all the discussions are based on the assumption that the extra dimensions are flat or weakly curved. Randall and Sundrum [10] proposed another possibility in which the extra dimension is strongly curved or warped by a large negative cosmological constant. The reason for gravity being much weaker than the weak interactions is that the wavefunction of the graviton on our plane would be exponentially suppressed if the graviton is not localized. String theory also provides motivation for the Randall-Sundrum (RS) scenario.

2.1.5 Hidden Valley

Many theories beyond the Standard Model have new sectors beside the Standard Model section. These new sectors may decouple from the Standard Model (visible) sector at low energy and may contain many new particles, which could be relatives of the dark matter particles. Hidden Valley [11] theory is one example of such theory containing the new sector. This theory has a hidden sector which has not been observed yet and contains relatively light particles, which could have relatively long lifetimes. However, there is some barrier preventing us from finding them up to now. Some phenomenology of Hidden Valley models could be very distinct from that of the well-studied physics, like the Standard Model, SUSY, extra dimensions, etc.

In Hidden Valley models [12], the Standard Model gauge group G_{SM} is extended by a non-abelian group G_v. All SM particles are neutral under G_v, while all the new particles (v-particles) in the hidden sector are light, charged in G_v, and neutral in G_{SM}. At the TeV scale, higher dimensional operators allow the SM fields to interact with the v-particles. There is not a clear minimal

representative for Hidden Valley models, but many phenomena are common for a typical v-sector. Some examples are listed:

- There are some long-lived v-hadrons whose masses are typically in the order of the v-confinement scale Λ_v.
- Some v-hadrons may be stable such that they could be dark matter candidates and also leave signatures in collider detectors as missing energy.
- Some v-hadrons, in contrast, would decay into neutral combinations of the SM particles.
- v-hadrons could have lifetimes varying over many orders of magnitude. Some v-hadrons would decay promptly, leaving a displaced vertex in the detectors, or they can live long enough to decay outside the detector.
- The decay modes of the v-hadron could have different final states. Heavy flavor final states are preferred by some v-hadrons, while $f\bar{f}$ or $f\bar{f}$ plus another v-hadron final state dominate for others. Some v-hadrons even decay to final states which include two or three gluons, WW and ZZ.
- The production multiplicities of the v-hadrons may be large, especially when $\Lambda_v \ll 1\,TeV$, at the LHC. The typical cross-sections for the v-hadrons at the LHC are in the range of 1–100 fb, while they are 1 fb or less for Tevatron.

In some Hidden Valley models [13], there is the possibility that some v-particles have long lifetimes and may decay visibly with a displaced vertex. In one example studied, the Higgs decays to long-lived neutral particles, which may decay at macroscopic distances from the primary vertex. This possibility opens the window that the Higgs may serve as a probe to the new sector of particles, which are uncharged under the Standard Model gauge group. Also it suggests that the Higgs may be able to be observed through this channel at the Tevatron. The detector signature can be varied depending on the final states, which could contain displaced vertices and/or leptons.

In the models where there is one light flavor (1LF) [12], lepton pairs could be produced with a large variety of v-hadrons. The lepton pair resonance produced from the v-particles will be burried in the Drell-Yan background unless events are required to have many bs or an unusual displaced

vertex. The v-particle decay following the $f\bar{f}$ pair emission provides interesting final states, like $\mu^+\mu^- b\bar{b}$. These events may be difficult to observe because a) the lepton may be hard to isolate; b) the displaced vertex can be everywhere in the detector, the beampipe, the tracker, or the calorimeter; c) jet identification may be challenging when several v-hadrons are produced.

2.2 SUSY and soft SUSY breaking

The neutral part of the Standard Model Higgs field is a complex scalar H with a classical potential

$$V = m_H^2|H|^2 + \lambda|H|^4 \tag{2.1}$$

In the Standard Model, the vacuum expectation value (VEV) for H is required to be non-zero at the minimal potential. If $\lambda > 0$ and $m_H^2 < 0$, then $< H >= \sqrt{-m_H^2/2\lambda}$.

If the Higgs field couples to a Direc fermion f having mass m_f with a term $-\lambda H\bar{f}f$ in the Lagrangian, the correction of the Higgs mass is given by

$$\Delta m_H^2 = -\frac{|\lambda_f|^2}{8\pi^2}\Lambda_{UV}^2 + ... \tag{2.2}$$

where Λ_{UV} is an ultraviolet momentum cutoff. Figure 2.1a) shows the Feynman diagram of this one-loop correction from the coupling between the Higgs and the Dirac fermion f. Each lepton and quark in Standard Model can be f, and eq. 2.2 should be multiplied by 3 in order to count the color for quarks. Since the quarks, leptons, and electroweak gauge bosons (Z^0, $W^{\pm}$) in the Standard Model obtain their masses from $< H >$, the entire mass spectrum of SM is sensitive to Λ_{UV}.

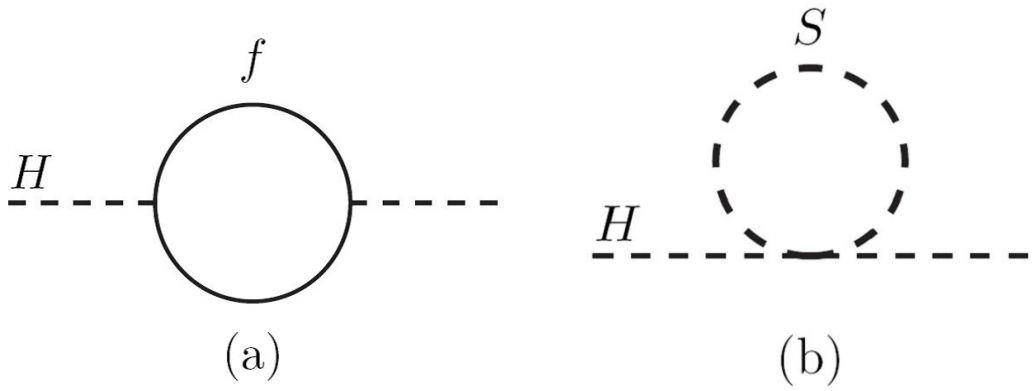

Figure 2.1: One-loop corrections to the Higgs squared mass parameter m_H^2, due to the coupling with a) a Dirac fermion f , and b) a scalar S.

If there is a heavy complex scalar particle S with mass m_S, which can couple to the Higgs in terms of $-\lambda_S|H|^2|S|^2$, the correction on the Higgs mass will be

$$\Delta m_H^2 = \frac{\lambda_S}{16\pi^2}\left[\Lambda_{UV}^2 - 2m_S^2 \ln\frac{\Lambda_{UV}}{m_S} + ...\right] \tag{2.3}$$

Similar to the Dirac fermion coupling, the Feynman diagram shown in Fig. 2.1b) is the one-loop correction arising from the coupling between the Higgs and the scalar S. The m_H^2 is sensitive to the masses of the heaviest particles to which the Higgs couples. A study of eq. 2.2 and eq. 2.3 strongly suggests that the contributions from the fermion loop and the boson loop to Δm_H^2 could cancel if there is a new symmetry between fermions and the bosons.

Supersymmetry is a symmetry relating fermions and bosons, which results in the cancellation between the fermion and boson contributions to Δm_H^2. The SUSY transformation turns a boson into a fermion, and vice versa. The operator Q that generates such transformations is given by

$$Q|boson>=|fermion>, \qquad Q|fermion>=|boson> \tag{2.4}$$

and it has to be an anticommuting spinor. $Q^\dagger$, the hermitian conjugate of Q, is also a symmetry generator. Both Q and $Q^\dagger$ are spin-1/2 fermionic operators, so that supersymmetry must be a spacetime symmetry. Q and $Q^\dagger$ must satisfy the algebra of anticommutation and commutation relations as the

following:

$$\begin{aligned} \left\{Q, Q^\dagger\right\} &= P^\mu, \\ \{Q, Q\} = \left\{Q^\dagger, Q^\dagger\right\} &= 0, \\ [P^\mu, Q] = \left[P^\mu, Q^\dagger\right] &= 0 \end{aligned} \tag{2.5}$$

where P^μ is the four-momentum generator of spacetime translations.

The boson state with the corresponding fermion state, known as the *superpartners* of each other, forms an irreducible representation of the supersymmetry algebra, which is called *supermultiplets*. Particles in the same supermultiplet must have equal masses, the same electric charges, weak isospins, and color degrees of freedom. Each supermultiplet contains an equal number of boson and fermion degrees of freedom.

In the supersymmetric extension of the Standard Model, every known fundamental particle has a superpartner with spin different by 1/2 of a unit, and is in either chiral or gauge supermultiplet. The names of the superpartners of the quarks or leptons with spin-0 are constructed by prepending an "s", which is for scalar. Generically, they are called *squarks* or *sleptons*, or *sfermions* standing for "scalar quark", "scalar lepton", and "scalar fermion", respectively. The symbols for sfermions are the same as for the corresponding fermion in the Standard Model, just with a tilde (~) to denote them as the superpartner of the SM particles.

The spin-0 Higgs scalar boson should be in a chiral supermultiplet, and there are two Higgs supermultiplets in order to keep the electroweak gauge symmetry. Each fermionic partner of a Higgs chiral supermultiplet must be a weak isodoublet with weak hypercharge $Y = 1/2$, or $Y = -1/2$. Only the $Y = 1/2$ Higgs chiral supermultiplet can have a Yukawa coupling to charge +2/3 up-type quarks (up, charm, and top) to give them masses. On the other hand, only $Y = -1/2$ Higgs chiral supermultiplet will have Yukawa couplings to the charge -1/3 down-type quarks (down, strange, and bottom), and to give them masses as well as the charged leptons. The $SU(2)_L$-doublet complex scalar fields are named as H_u and H_d for $Y = 1/2$ and $Y = -1/2$, respectively. The weak isospin components of H_u have electric charges 1, 0, so they are denoted as $\left(H_u^+,\ H_u^0\right)$. Similarly, the weak isospin components of H_d have electric charges 0, -1, so they are denoted as $\left(H_d^0,\ H_d^-\right)$. The neutral scalar corresponding to the physical Standard Model Higgs boson is a linear combination of H_u^0 and H_d^0. The fermionic partners of the Higgs scalars are called higgsinos, which are denoted by

Names		spin 1/2	spin 0	$SU(3)_C\, SU(2)_L\, U(1)_Y$
quarks, squarks	Q	$(u_L\ d_L)$	$\left(\tilde{u}_L\ \tilde{d}_L\right)$	$(3,\, 2,\, \frac{1}{6})$
	$\bar{u}$	$u_R^\dagger$	$\tilde{u}_R^\dagger$	$(\bar{3},\, 1,\, -\frac{2}{3})$
3 families	$\bar{d}$	$d_R^\dagger$	$\tilde{d}_R^\dagger$	$(\bar{3},\, 1\ \frac{1}{3})$
leptons, sleptons	L	$(\nu\ e_L)$	$(\tilde{\nu}\ \tilde{e}_L)$	$(1,\, 2,\, -\frac{1}{2})$
3 families	$\bar{e}$	$e_R^\dagger$	$\tilde{e}_R^\dagger$	$(1,\, 1,\, 1)$
Higgs	H_u	$\begin{pmatrix} H_u^+ & H_u^0 \end{pmatrix}$	$\begin{pmatrix} \tilde{H}_u^+ & \tilde{H}_u^0 \end{pmatrix}$	$(1,\, 2,\, +\frac{1}{2})$
higgsinos	H_d	$\begin{pmatrix} H_d^0 & H_d^- \end{pmatrix}$	$\begin{pmatrix} \tilde{H}_d^0 & \tilde{H}_d^- \end{pmatrix}$	$(1,\, 2,\, -\frac{1}{2})$

Table 2.1: Chiral supermultiplets in the Minimal Supersymmetric Standard Model. The spin-0 fields are complex scalars, and the spin-1/2 fields are left-handed two-component Weyl fermions.

$\tilde{H}_u$ and $\tilde{H}_d$ for the $SU(2)_L-$doublet left-handed Weyl spinor fields, with weak isospin components $\tilde{H}_u^+$, $\tilde{H}_u^0$, and $\tilde{H}_d^0$, $\tilde{H}_d^-$.

All the chiral supermultiplets of a minimal phenomenologically viable extension of the SM are summarized in Table 2.1.

All the superpartners of the Standard Model particles are new particles, and cannot be identified with other Standard Model states. The superpartners of the vector bosons of the Standard Model are referred to as gauginos and are in gauge supermultiplets. Gluons (g) mediate the color gauge interactions of QCD, while the spin-1/2 octant superpartners are the gluino ($\tilde{g}$). The spin-1 gauge bosons associated with the electroweak gauge symmetry are W^+, W^0, W^-, and B^0, and their spin-1/2 superpartners are $\tilde{W}^+$, $\tilde{W}^0$, $\tilde{W}^-$, and $\tilde{B}^0$, named as *winos* and *binos*. The mass eigenstates Z^0 and γ are the mix of the W^0 and B^0 gauge eigenstates after the electroweak symmetry breaking. The corresponding gauginos are called zino ($\tilde{Z}^0$) and photino ($\tilde{\gamma}$). Table 2.2 summarizes the gauge supermultiplets of a minimal supersymmetric extension of the Standard Model (MSSM).

Names	sping 1	spin 1/2	$SU(3)_C,\ SU(2)_L,\ U(1)_Y$
gluon, gluino	g	$\tilde{g}$	(8, 1, 0)
W bosons, winos	$W^\pm\, W^0$	$\tilde{W}^\pm\, \tilde{W}^0$	(1, 3, 0)
B boson, bino	B^0	$\tilde{B}^0$	(1, 1, 0)

Table 2.2: Gauge supermultiplets of in the Minimal Supersymmetric Standard Model (MSSM).

None of the superpartners of the Standard Model particles have been found. If the supersymmetry were unbroken, the superpartners should had exactly the same masses as the Standard Model particles, therefore they should have been discovered. The supersymmetry is a broken symmetry in the vacuum state chosen by Nature. The effective Lagrangian of the MSSM can be written in the form

$$\mathcal{L} = \mathcal{L}_{SUSY} + \mathcal{L}_{soft} \tag{2.6}$$

where $\mathcal{L}_{SUSY}$ has all the gauge and Yukawa interactions and is supersymmetery invariant, and $\mathcal{L}_{soft}$, the "soft" supersymmetry breaking term, violates supersymmetry but contains only mass terms and couplings parameters with *positive* mass dimension. The additional non-supersymmetric corrections to the Higgs scalar squared mass should be in the form

$$\Delta m_H^2 = m_{soft}^2 \left[\frac{\lambda}{16\pi^2} \ln\left(\frac{\Lambda_{UV}}{m_{soft}}\right) + ... \right] ... \tag{2.7}$$

where λ is schematic for various dimensionless couplings, m_{soft} is the largest mass scale associated with the soft term, and the ellipses are both for terms independent of Λ_{UV} and for higher loop corrections.

The superpartner masses cannot be too huge since the parameters m_{soft} in $\mathcal{L}_{soft}$ determine the mass splittings between the Standard Model particles with their superpartners. Furthermore, the difference between the superpartner masses is within an order of magnitude. With $\Lambda_{UV} \sim M_P$ and $\lambda \sim 1$, m_{soft} should be at the most about 1 TeV or so, in order for the MSSM scalar potential to provide a Higgs VEV resulting in $m_W,\ m_Z = 80.4,\ 91.2$ GeV without miraculous cancellations. Therefore, at least the masses of the lightest superpartners should be at most in 1 TeV scale.

All the particles in MSSM found so far share a common property that they must be massless in the absense of electroweak symmetry breaking. However, the massess of the $W^{\pm}$, Z^0 bosons are equal to dimensionless coupling constants times the Higgs VEV. The same is the case with all the quarks and leptons. Meanwhile, the photon and gluons are required to be massless by electromagnetic and QCD gauge invariance. However, all the undiscovered particles share exactly the opposite property. Each of those particles can have a Lagrangian mass term in the absence of electroweak symmetry breaking. For the sfermions and Higgs scalars, this results from a general property of

complex scalar fields that a mass term $m^2|\phi|^2$ is always allowed by all gauge symmetries. As for the higgsinos and gauginos, they obtain their mass because they are fermions in a real representation of the gauge group.

The superpartners listed in Tables 2.1 and 2.2 are not necessarily the mass eigenstates of the theory. After the electroweak symmetry breaking and supersymmetry breaking effects are included, there can be mixings between the electroweak gauginos and the higgsinos. The same mixing can also happen within the various sets of sfermions and Higgs scalars which have same electric charge. The gluino is the only exception, because it is a color octet fermion and does not have the appropriate quantum numbers to mix with other particles.

2.3 Gauge Mediated SUSY Breaking (GMSB)

2.3.1 GMSB

In general, SUSY as an extension of the Standard Model in principle could have an infinite number of parameters. In order to have a manageable parameter space, it is normal to restrict to the "General MSSM", in which the particle contents are limited to the minimum containing the Standard Model. The mass eigenstates of this theory includes 12 squarks, 6 sleptons, 3 sneutrinos, 1 gluino, 4 neutralinos, 2 charginos, and 3 neutral and 1 charged Higgs scalars. In this model, there are still 296 new parameters besides those in the Standard Model. By removing all R-parity violating couplings, the "R-parity-conserving MSSM" contains 105 new parameters, which is still unmanageablely large for most studies. Further reducement in parameter space can be obtained by the "Flavor-respecting-MSSM". In this framework, all SUSY-breaking parameters are assumed to respect flavor-symmetry and no new CP-violating phases are introduced.

The model parameters are the following:

- Gaugino masses M_1, M_2, and M_3,
- Family-independent squark and slepton squared masses $m^2_{\tilde{Q}_L}$, $m^2_{\tilde{u}_R}$, $m^2_{\tilde{d}R}$, $m^2_{\tilde{L}_L}$, $m^2_{\tilde{e}_R}$,
- Higgs squared masses $m^2_{H_u}$, $m^2_{H_d}$,
- Scalar cubic coupling which are 3 $\times$3 matrices proportional to the corresponding Yukawa

couplings, with constants of proportionality A_{u0}, A_{d0}, A_{e0},

- The ratio of Higgs expectation values $\tan\beta \equiv < H_u^0 > / < H_d^0 >$,
- The sign of the supersymmetric Higgs mass parameter μ.

The Gauge-Mediated SUSY-Breaking (GMSB) framework [14, 15, 16] is a subcase of the Flavor-respecting MSSM parameter space. In GMSB models, the appearance of soft supersymmetry breaking results from the ordinary gauge interactions. New chiral supermultiplets, messengers, are introduced, which couple to the supersymmetry breaking source. Messengers also couple indirectly to the (s)fermions, and Higgs(inos) through the ordinary $SU(3)_C \times SU(2)_L \times U(1)_Y$ gauge boson and gaugino interactions. In GMSB, the flavor-preservation is automatic, since SUSY-breaking is transmitted from a hidden sector to the MSSM particles by messenger fields which only share gauge interactions with the ordinary particles. The gravitional communication between the MSSM and the source of the supersymmetry breaking also exists; however, the effect is relatively unimportant compared to the gauge interaction effects.

The parameters in minimal GMSB is

- Λ, the effective mass scale of the SUSY-breaking. The SUSY particle masses have a near linear dependence on the Λ.
- M_m, the common messenger particle mass. The sparticle masses will increase logarithmically by increasing M_m.
- N_5, the number of complete $SU(5)$ $5 + \bar{5}$ multiplets of messengers. Increasing N_5 tends to decrease squark and slepton masses relative to gaugino masses.
- $\tan\beta$,
- $sign(\mu)$,
- C_G, a suppression factor of the goldstino coupling. The lifetime of the next-to-lightest SUSY particle will increase by raising C_G.

As a result of the spontaneous supersymmetry breaking, the physical spectrum contains a massless spin-1/2 fermion, the goldstino ($\tilde{G}$). The goldstino provides the longitudinal modes of the gravitino,

the spin-3/2 partner of the graviton, when the global supersymmetric theory is coupled to gravity and promoted to a local supersymmetric theory. This is the super-Higgs mechanism, in which the gravitino requires a mass. The mass of the gravitino is given by

$$m_{3/2} = \frac{F}{k\sqrt{3}M_P} = \frac{1}{k}\left(\frac{\sqrt{F}}{100TeV}\right)^2 2.4\,eV \tag{2.8}$$

where the model-dependent coefficient k, $k \equiv F/F_0$, is such that $k < 1$, and possibly $k \ll 1$, F is the scale of supersymmetry breaking felt by the messenger particles, F_0 is the fundamental scale of supersymmetry breaking, $M_P = (8\pi G_N)^{-1/2} = 2.4 \times 10^{18}\ GeV$ is the reduced Planck mass. In gauge-mediated models, the gravitino is the lightest supersymmetric particle (LSP) for any value of F. Assuming that the R-parity is conserved, all the supersymmetric particles will follow the decay chains leading to gravitinos. The dominant gravitino interactions come from the spin-1/2 component, when $\sqrt{F} \ll M_P$ is true. The interactions of goldstino with derivative couplings are suppressed by $1/F_0$, which are typically larger than the gravitional couplings suppressed by $1/M_P$. It is adequate for our purpose to describe the LSP in terms of the goldstino properties and the only role of gravity is to generate the LSP mass.

The next-to-lightest supersymmetric particle (NLSP) plays an important role in the phenomenology of gauge mediation. With the R-parity conservation, all supersymmetric particles will decay into cascades leading to the NLSP, where the NLSP then decays into the gravitino via 1/F interactions. In principle, the NLSP can be any MSSM superpartner. However, a neutralino or a slepton plays this role in most GMSB models. The reason is that those superpartners with only $U(1)_Y$ interactions tend to have the smallest masses. The gauge-eigenstate sparticles with this property are the bino and the right-handed sleptons, so the appropriate corresponding mass eigen-states should be the good NLSP candidates. Depending on the parameter choice, the NLSP candidate can be the neutralino, the stau, or the sneutrino within a very restricted parameter region.

2.3.2 Stau in Model Line D

The concept "model lines" [17, 18] are introduced so that each model line consists of a one-parameter family of models. Typically the one parameter is the overall superpartner scale, like Λ in GMSB. Other dimensionful model parameters are then chosen proprotional, while dimension-

less parameters are fixed like $\tan\beta$, and $sign(\mu)$. The SM quantities are set to the default values, e.g. $m_{top} = 175$ GeV.

One NLSP candidate can be a charged slepton. Actually, there are more than one slepton could actively be the NLSP candidate, even though one of them is slightly lighter than the other two. However, if all sleptons are close enough in mass, then only the decay to the goldstino is allowed kinematically. The squared masses of $\tilde{e}_R$, $\tilde{\mu}_R$, and $\tilde{\tau}_R$ arising from the flavor-blindness of the gauge couplings are equal. However, they are no longer the same after taking the mixing with $\tilde{e}_L$, $\tilde{\mu}_L$, and $\tilde{\tau}_L$, and the renormalizationg group running into account. These effects are much larger for $\tilde{\tau}_R$ than $\tilde{e}_R$ and $\tilde{\mu}_R$, due to the significant mixing between $\tilde{\tau}_R$ and $\tilde{\tau}_L$, which is proportional to the tau Yukawa coupling. Thus, the lighter mass eigenstate $\tilde{\tau}_1$ has lower mass than $\tilde{e}_R$ and $\tilde{\mu}_R$ with the amount strongly dependent on $\tan\beta$.

If $\tan\beta$ is small, then $\tilde{e}_R$, $\tilde{\mu}_R$, and $\tilde{\tau}_1$ degenerate with mass differences less than 1.8 GeV. The only allowed decays for the three lightest sleptons are $\tilde{l} \rightarrow l\tilde{G}$. This is the "slepton co-NLSP" scenario, where the three lightest sleptons act effectively as co-NLSPs.

In case of large $\tan\beta$, the lighter mass eigenstate $\tilde{\tau}_1$ is more than 1.8 GeV lighter than the $\tilde{e}_R$ and $\tilde{\mu}_R$. $\tilde{\tau}_1$ is the sole NLSP, and all other MSSM supersymmetric particles are kinematically allowed to decay into it. This is the "stau NLSP" scenario.

In our analysis, we choose one particular model, which is "model line D". In this GMSB model, the NLSP is stau. The model parameters are $M_m = 2\Lambda$, $N_5 = 3$, $\tan\beta = 15$, and $sign(\mu) > 0$, where Λ is the varying parameter. The parameters of this model are shown in Table 2.3.

Parameter	Description	Value
Λ_m	Scale of SUSY breaking	19 to 100 TeV
M_m	Messenger mass scale	$2\Lambda_m$
N_5	Number of messenger fields	3
$tan\beta$	Ratio of Higgs VEVs	15
$sgn\mu$	Sign of Higgsino mass term	$+1$
C_{grav}	Factor multiplying effective mass of gravitino	1

Table 2.3: GMSB Model Parameters

The NLSP stau decay rate is

$$\Gamma(\tilde{\tau} \to \tau \tilde{G}) = \frac{m_{\tilde{\tau}}^5}{16\pi F^2} = \left(\frac{m_{\tilde{\tau}}}{100\,GeV}\right)^5 \left(\frac{100\,TeV}{\sqrt{F}}\right)^4 \cdot 2 \times 10^{-3} eV \tag{2.9}$$

and the decay length of a stau with energy E in the lab frame is

$$d = 9.9 \times 10^{-3} \sqrt{\frac{E^2}{m_{\tilde{\tau}_1}^2} - 1} \left(\frac{100\,GeV}{m_{\tilde{\tau}_1}}\right)^5 \left(\frac{\sqrt{F}}{100\,TeV}\right)^4 cm \tag{2.10}$$

The decay length can vary from sub-micron to multi-kilometer, depending on the supersymmetry breaking scale $\sqrt{F}$. If $\sqrt{F}$ is larger than 10^3 TeV or the gravitino is heavier than a keV or so, the NLSP would be long-lived experimentally so that it can escape from a typical collider detector.

2.4 Charginos

The MSSM and the supersymmetry breaking sectors can be partitioned as geography. The visible sector and the hidden sectors are physically separated in distance. This general assumption opens up possiblities for numerous models. Anomaly-mediated sypersymmetry breaking (AMSB) [6, 19, 20] is only one of them. In AMSB, the gauge supermultiplet fields are confined to the MSSM plane, and supergravity effects are the only source responsible for the transmission of the supersymmetry breaking. The term "AMSB" comes from the fact that the MSSM soft terms in this model can be understood in terms of the anomalous violation of a local superconformal invariance, which is an extension of scale invariance. The AMSB framework is another sub-case of the flavor-preserving MSSM parameter space. The parameters that minimal phenomenologically-viable version (mAMSB) depends on are:

- $m_{3/2}$ = the auxiliary mass, which sets the overall SUSY-breaking scale,
- m_0^2 = a common scalar squared mass,
- $\tan\beta$,
- sign(μ).

In order to keep the charged sleptons with non-negative squared masses, the m_0^2 must be large enough in these models. The nearly-degenerate neutral and charged wino are often the LSP in

AMSB models, which leads to very unique phenomenology. AMSB can also be denoted as "model line G", where $m_{3/2}$ varies as the dimensionful parameter, $m_0 = 0.0075 m_{3/2}$, $\tan\beta = 15$, and $\mu > 0$.

The Planck mass scale is set by the VEV of a scalar field ϕ which obtains a VEV of $< \phi >= 1$, spontaneously breaking the local invariance. In presence of spontaneous supersymmetry breaking $< F >\neq 0$, the auxiliary field component obtains a non-zero VEV, $\frac{<F>}{M_P} \sim m_{3/2}$.

Due to the small mass difference between $\tilde{\chi}_1^{\pm}$ and $\tilde{\chi}_1^0$, the chargino could live long enough that it could deposit anomalous ionization energy in the tracking system while leaving little associated energy in the calorimeters. The average traveling distance of a chargino with energy E is given by

$$L = \left(\frac{GeV}{m_{\tilde{\chi}_1^{\pm}} - m_{\tilde{\chi}_1^0}} \right)^5 \sqrt{\frac{E^2}{m^2_{\tilde{\chi}_1^{\pm}}} - 1} \times 10^{-2}\, cm \tag{2.11}$$

where $\Delta m_{\tilde{\chi}_1} \cong m_{\tilde{\chi}_1^{\pm}} - m_{\tilde{\chi}_1^0} \sim M_W^3/\mu^2$. This travel path could be macroscopic and exceed the typical collider detector size if μ is in the order of the gravitino mass. In the case in which $\Delta m_{\tilde{\chi}_1} \lesssim 150\, MeV$, the lifetime of the charginos becomes so long that they would appear as a charged "stable" particles. Here "stable" means that the particle will penetrate through the whole collider detector and not decay within the detector.

When the $\tilde{\chi}_1^{\pm}$ and $\tilde{\chi}_1^0$ are degenerate in mass, discoverying SUSY would be very challenging and difficult to fully interpret. Two scenarios arise naturally. One is that charginos are mainly gaugino-like, and the other is when higgsino-like charginos dominate. The parameters for these two models are shown in Table 2.4. The analysis strategy is the same as for the stau search, and also only the pair-production of the lightest chargino is considered.

Model	gaugino-like chargino	higgsino-like chargino
μ(GeV)	$10,000$	varies from 60 to 300
M_1(GeV)	$3M_2$	$100,000$
M_2(GeV)	varies from 60 to 300	$100,000$
M_3(GeV)	500	500
$\tan\beta$	15	15
Squark Mass (GeV)	800	800

Table 2.4: Model Parameters for Stable Charginos.

2.4.1 Gaugino-Like Charginos

This is the scenario where gauginos are the major components of the charginos. It satisfies $M_2 < M_1 \ll |\mu|$. This occurs when the gaugino masses are dominated by loop corrections, which could arise in the O-II superstring model and the models where SUSY breaking results entirely from the conformal anomaly.

In the O-II model with $\delta_{GS} = 0$, which is equivalent to the simplest version of the conformal anomaly approach, the gaugino masses have the relation as $M_3 : M_2 : M_1 = 3 : 0.3 : 1$. This means that M_2 would be lighter than M_1, and the tree-level mass difference value can be very small. Also in this model, $m_{\tilde{\chi}_2^0}$ and $m_{\tilde{g}}$ are typically close to the common $\tilde{\chi}_1^\pm$, and $\tilde{\chi}_1^0$ masses, and it is natural for the sfermions (squarks and sleptons) to have much heavier masses than any of the gaugino masses. $|\mu|$ has large values typically, and the higgsino $\tilde{\chi}_2^\pm$, $\tilde{\chi}_3^0$, and $\tilde{\chi}_4^0$ states are very heavy. Also, normally the gluino is much heavier than the chargino.

A good approximation to the tree-level correction of the $\Delta m_{\tilde{\chi}_1}$ is given by

$$\Delta m_{\tilde{\chi}_1}(tree) \simeq \frac{m_W^4 \tan^2\theta_W}{(M_1 - M_2)\mu^2} \sin^2 2\beta \tag{2.12}$$

If $M_1 - M_2 > 0$, then $\Delta m_{\tilde{\chi}_1}(tree)$ will be positive and it is inevitable that $\Delta m_{\tilde{\chi}_1} > m_\pi$. Also there is possiblity that $\Delta m_{\tilde{\chi}_1} < m_\pi$, when $|M_2| < |M_1|$ but with negative $M_1 - M_2$.

The production rates for the light charginos follow the pattern that the $Z \to \tilde{\chi}_1^0\tilde{\chi}_1^0$, $Z \to \tilde{\chi}_1^0\tilde{\chi}_2^0$, $Z \to \tilde{\chi}_2^0\tilde{\chi}_2^0$, and $W^\pm \to \tilde{\chi}_1^\pm\tilde{\chi}_2^0$ will have very small cross sections. However, the cross sections for $Z/\gamma \to \tilde{\chi}_1^+\tilde{\chi}_1^-$, and $W^\pm \to \tilde{\chi}_1^\pm\tilde{\chi}_1^0$ are much larger. This is because the neutralio and chargino couplings to W and Z bosons depend on M_1, M_2, μ, and tanβ, in the absence of CP violation.

2.4.2 Higgsino-Like Charginos

Another scenario is when the $\tilde{\chi}_1^\pm$, the $\tilde{\chi}_1^0$, and the $\tilde{\chi}_2^0$ are all closely degenerate in mass and higgsino-like. This scenario requires that $|\mu| \ll M_{1,2}$, and the gaugino states are much heavier than the charginos. The sfermions, squarks, and sleptons, might also have large masses. This is a less theoretically motivated scenario. The exact value of $\Delta m_{\tilde{\chi}_1}$ depends on model parameters, although generally it is difficult to achieve $\Delta m_{\tilde{\chi}_1} < m_\pi$. The reason is that the one-loop electroweak radiative corrections contribute positively to the $\Delta m_{\tilde{\chi}_1}$with a typical value larger than m_π. Thus the

$\Delta m_{\tilde{\chi}_1}$is normally in a range from slightly above m_π up to a few GeV. This is the range where supersymmetry signals are very difficult to detect.

Similarly as in the gaugino-like chargino scenario, the production rates for the $Z \rightarrow \tilde{\chi}_1^0\tilde{\chi}_1^0$, and $Z \rightarrow \tilde{\chi}_2^0\tilde{\chi}_2^0$, will be suppressed instead. Meanwhile, the cross sections for $Z/\gamma \rightarrow \tilde{\chi}_1^+\tilde{\chi}_1^-$, $Z \rightarrow \tilde{\chi}_1^0\tilde{\chi}_2^0$, $W^\pm \rightarrow \tilde{\chi}_1^\pm\tilde{\chi}_1^0$, and $W^\pm \rightarrow \tilde{\chi}_1^\pm\tilde{\chi}_2^0$ are large although still smaller than the unsuppressed channels in gaugino-like scenario.

In this analysis, we only consider an extreme case in both scenarios, which is that $\Delta m_{\tilde{\chi}_1}$ is sufficiently small (typically less than 200 MeV). In this case, the lightest chargino could have a liftime long enough for it to penetrate through the entire DØ detector, and the average $c\tau$ is in the order of a meter or even more. Although it is unlikely to have $\Delta m_{\tilde{\chi}_1} < m_\pi$ in most existing models, there is still a tail of events with long enough lifetimes even when $\Delta m_{\tilde{\chi}_1} > m_\pi$.

2.5 Detector Signature of Heavy Particles

The lightest supersymmetry particles (LSPs) are normally electrically neutral (carrying no electric charge) [6] and have no interactions with the detector. So the detector signatures for the LSPs would be very similar to neutrinos, which make them hard to detect directly. In contrast, the next lightest supersymmetry particles (NLSP) could have electrical charge, which means that they can interact with materials and leave hits in the tracking system. These particles also have larger masses than their superpartners in SM. The charged NLSPs have rather striking signatures in the collider detector. If they are long-lived, they usually escape a typical collider detector and leave tracks (or possibly decay kinks) inside the detector [21]. The anomally long time-of-flight and/or high ionization rate for a track in the detector are the key signature of charged massive NLSPs and can be used as selection criteria.

2.5.1 Time-of-flight for heavy particles

The method of time-of-flight is one technique that can be employed to detect massive stable particles. Massive particles are produced and travel with a smaller speed than light particles. Thus, they would have much larger flying time in the detector. Various variables could be derived from the measured time-of-flight, such as the time-of-flight mass of the particle. Further requirements can be

applied to classify the signal from the background.

The time decay in TOF would indicate the particle mass, and such events could be background free. This is because all the known found particles in the Standard Model should travel faster than their superpartners, which have much larger masses. Thus, there is no physics background from the Standard Model, which means that this is a clean channel. No real physics background from the Standard Model makes this method a very powerful technique for hunting for any new massive charged long-lived particles appearing in physics beyond the Standard Model.

The principal background in the time-of-flight measurement arises from the instrumental effects, such as mismeasured timing, or mismatched hits in the scintillator counter detectors. Cosmic rays could also contribute as a substantial background.

2.5.2 Electronic energy loss by charged heavy particles

Charged particles other than electrons, traveling relativistically, will lose energy in matter by either interactions with atomic electrons or collisions with atomic nuclei [22]. The first process results in the liberation of electrons from the atoms in the material, which is the ionization. The second process is called Non-Ionising Energy Loss, which results in the atomic excitations. At the high velocity region, the energy loss in the material is dominated by ionization. The energy loss rate or stopping power of a fast particle in a medium is given by the Bethe-Bloch formula:

$$-\frac{dE}{dx} = Kz^2\frac{Z}{A}\frac{1}{\beta^2}\left[\frac{1}{2}\ln\frac{2m_ec^2\beta^2\gamma^2T_{max}}{I^2} - \beta^2 - \frac{\delta}{2}\right] \tag{2.13}$$

where the T_{max} is the maximum kinetic energy which can be transferred to a free electron in a single collision. Other variables are defined in Table 2.5.

Symmbol	Definition	Value or Unit
M	Incident particle mass	MeV/c^2
r_e	Classical electron radius $e^2/4\pi\epsilon_0 m_e c^2$	2.82 fm
$m_e c^2$	Electron mass	$0.511 MeV/c^2$
z	Charge of incident particle	
Z	Atomic number of absorber	
A	Atomic mass of absorber	$g\,mol^{-1}$
K	$4\pi N_A r_e^2 m_e c^2$	$\frac{K}{A} = 0.31 MeV g^{-1} cm^2$ for $A = 1\,g\,mol^{-1}$
I	Mean excitation energy	eV

Table 2.5: Summary of variables used in Bethe-Bloch formula.

For a particle with mass M and momentum $M\gamma\beta c$, $T_{max}$is

$$T_{max} = \frac{2m_e c^2 \beta^2 \gamma^2}{1 + 2\gamma m_e/M + (m_e/M)^2} \tag{2.14}$$

The stopping power computed for muons in copper is shown in Fig. 2.2 as the solid curve. Figure 2.3 compares the energy deposit in the same material by different particles. 185 samples are measured with 8.5 atm and the ratio of Ar-CH_4 at 80:20 [22]. From Fig.2.3, we can observe that different types of particles would have different energy loss when they travel in the same material. In other words, we can distinguish different particles by studying the energy deposit in the same detectors.

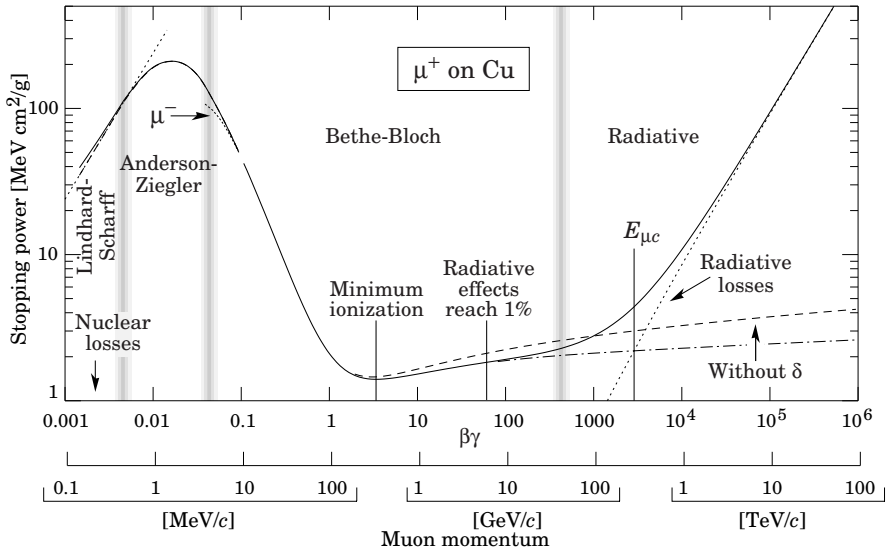

Figure 2.2: Stopping power (=$< -dE/dx >$) for positive muons in copper as a function of $\beta\gamma = p/Mc$ over nine orders of magnitude in momentum. Solid curves indicate the total stopping power [22].

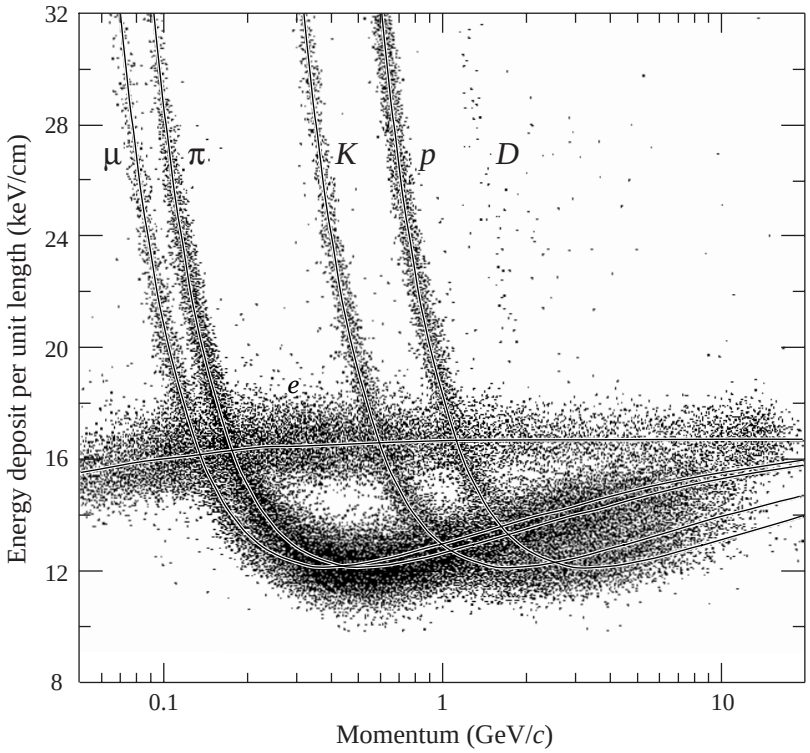

Figure 2.3: The PEP4/9-TPC energy deposit measurement. The ionization rate at the Fermi plateau (high β) is 1.4 times that for the minimum at lower β [22].

The energy loss rate in the same material is mainly dependent of the velocity of the incident charged particles. The charged massive particles normally deposit more energy than the faster particles due to their lower speed value resulting from their heavier mass. Beside the energy loss rate, the path length of the incident particle also contributes to the total energy deposit of the particle. Since the material in the detector is fixed and mainly uniformly distributed, the particle's distance of travel depends on its type, which determines how far it can penetrate, as well as on the angle at which it traverses the material.

2.6 Previous and Present Searches

Hunting for new particles has always been an active and attractive topic in the experimental physics community. Many physics theories beyond the Standard Model predict many new particles which may have very different properties compared with the particles in the SM. In past decades, people has paid keen attention to the possible models predicting long-lived particles in both theory and phenomenology. On the experimental side, searches for the relatives of the dark matter particles are being undertaken with astronomy experiments, underground dark matter servies, and the energy frontier colliders. Although cosmological observations place severe limits on absolutely stable massive particles [23][24], these limits do not rule out the particles predicted by the models considered in this analysis.

Since long-lived NLSPs have more striking detector signatures than the LSPs, several collider experiments have performed searches for long-lived NLSPs. In particular, studies have been carried out at the CERN e^+e^- collider (LEP), resulting in mass limits on the long-lived NLSPs in different models. For long-lived staus, the lower mass limit has been set as 97.5 GeV[25], while the lower mass limit is 102.5 GeV for long-lived charginos[26]. Similar searches have been performed at Fermilab Tevatron $p\bar{p}$ collider at Run I. CDF [27] searches placed a limit of $\mathcal{O}(1)$ pb on the cross section for stable sleptons. A search has also been performed at DØ experiment during Run II stage using collected data corresponding to an integrated luminosity of $\sim 400pb^{-1}$ [28]. In the DØ search, the time-of-flight information of the particle registered at the muon system was used to classify the signal candidates from the background, and the result was interpretated with three SUSY models.

These three models, tau sleptons in GMSB and charginos in AMSB-motivated models, are the ones discussed in earlier sections. Only direct pair production of the NLSPs are studied, and no cascade decays are considered. The 95% C.L. limits were set on the cross section of the pair production of staus, which varies from 0.62 pb^{-1} to 0.06 pb^{-1} with masses from 60 GeV to 300 GeV. The lower mass limits were set on the pair-produced charginos, which are 174 GeV for gaugino-like charginos and 140 GeV for higgsino-like charginos.

Tevatron is performing stablely and well during the past few years, more than 5 fb^{-1}data events have been delivered and recorded. The searches for long-lived NLSPs will be continued at DØ.

One of the goals for the Large Hadron Collider (LHC) pp experiments is to investigate the physics at the energy scale beyond the Standard Model. Searches for new particles in different models have been started at both ATLAS and CMS. Long-lived charged massive particles predicted in many theories beyond the Standard Model are undertaken due to their striking detector signature.

Chapter 3

Experimental Apparatus

The events were produced in the Tevatron Collider with $p\bar{p}$ collisions at the center-of-mass energy of 1.96 TeV, and the products of the collisions were measured by the DØ detector. This chapter provides an introduction to the Fermilab Tevatron and a description of the DØ detector.

3.1 The Tevatron Collider

The Fermi National Accelerator Laboratory (Fermilab)[29], located in Batavia, IL, is home of the Tevatron proton-antiproton Collider[30], which is the highest energy particle collider in the world until the Large Hadron Collider (LHC) becomes operational at CERN. Two collider detectors, CDF and DØ, are located along the Tevatron ring.

The particles which are collided at the detectors are produced and accelated in a series of stages[31]. The starting point for the protons is the Cockcroft-Walton accelerator, where electrons are added to hydrogen atoms which are pulled toward a positive voltage. These negative ions with an energy of 750 keV are injected into a 150 meter long linear accelerator called the Linac, where they are accelerated to 400 MeV. At the end of the Linac, protons are produced by removing the electrons from the hydrogen ions using carbon foil. Then the protons are injected into the Booster, a 150 meter diameter synchrotron; they are bent together, merged into one bunch and accelerated to an energy of 8 GeV.

The protons are injected into the Main Injector from the Booster. The Main Injector is a rapid cycling synchrotron with a 2 mile circumference. It accelerates the proton beam to 120 GeV, at

which point it can be either extracted to the antiproton production target or to the next stage of acceleration. For injecting either proton or antiproton beams into the Tevatron, the Main Injector accelerates the beam to 150 GeV.

The antiprotons are created at the Antiproton Source where 120 GeV protons are collided with a nickel target. The antiprotons in the debris from those collisions are collected using a lithium lens, which produces an azimuthal magnetic field to focus the antiprotons. A bending magnet after the lens selects antiprotons with energies of about 8 GeV, which are transfered to the Debuncher. The Debuncher is a 8 GeV storage ring, where the antiprotons are arranged in bunches, reduced in momentum spread and increased in longitudinal distance spread. Then the antiprotons are transported to the Accumulator, another 8 GeV strorage ring. The antiprotons are cooled (reduced in momentum spread and transverse oscillations) and accumulated to be transferred to the Recycler. The Recycler ring is located directly above the Main Injector beam line in the same tunnel.

The Tevatron is the final stage of the acceleration. It is a synchrotron with superconducting magnets in a 4 mile long tunnel. Protons and antiprotons injected from the Main Injector are accelerated to 980 GeV from 150 GeV. 36 bunches of protons and 36 bunches of antiprotons are circulated in opposite directions in the same beam pipe. There are in total six desired interaction points along the ring, where the collisions could happen. The CDF and DØ detectors are located at two such interaction points (B0 and D0 respectively). The two beams collide in bunches at each interaction point and $p\bar{p}$ bunches pass through each other every 396 ns. The time interval between collisions is 396 ns.

3.2 The DØ Detector

The DØ detector is designed to study proton-antiproton collisions at the Fermilab Tevatron Collider. The focus of the detector design is the study of high mass states and large p_T phenomena. The DØ detector was proposed in 1983 and completed in 1992. A full description of Run I DØ detector can be found in [32]. During Run I, the DØ experiment recorded approximatedly 130 pb^{-1} of data with a center-of-mass energy of 1.8 TeV and 3500 ns between bunch crossings. In Run II, which began in March 2001, the upgraded Tevatron is operated with 36 bunches of the protons and antiprotons with a 396 ns bunch spacing at an increased center-of-mass energy of 1.96 TeV. The DØ detector was

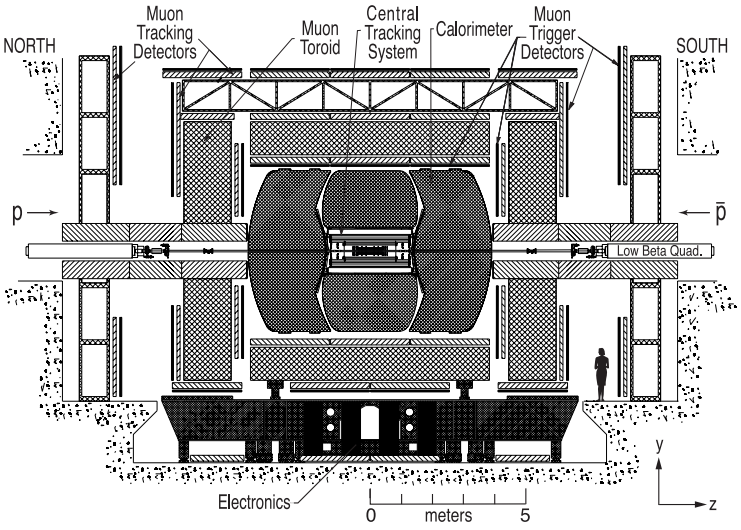

Figure 3.1: Diagram of the upgraded DØ detector as installed in the collision hall and viewed from the inside of the Tevatron ring. The forward proton detector is not shown [33].

upgraded to enhance its capabilities for Run II and to take advantage of the Tevatron improvements [33]. Figure 3.1 shows schedmatic side view of the Run II DØ detector. The data used in this thesis are recorded between 2002 and 2006 corresponding to an integrated luminosity of $1.1\ fb^{-1}$.

The detector has an onion-like structure like most general purpose high energy collider detectors. There are three principal subsystems: central tracking detectors, uranium/liquid-argon calorimeters, and a muon system. The innermost layer is the central tracking system, which consists of silicon micro-strip tracking system (SMT) and central fiber tracking system (CFT), located within a 2 Tesla solenoidal magnet. The calorimeter itself remains unchanged from Run I, although the readout electronics has been completely replaced. Preshower detectors have been added between the solenoidal magnet and the central calorimeter and in front of the foward calorimeters, to improve electron identification. New muon trigger detectors have been added to improve muon triggering. Also a foward proton detector has been added for study of diffractive physics. The upgraded trigger system provides three full trigger levels to complement the higher collision rate and new hardware.

Different types of particles leave different traces in different detector systems, which are called the detector signatures of the particles. Figure 3.2 shows the path depths of typical particles pena-

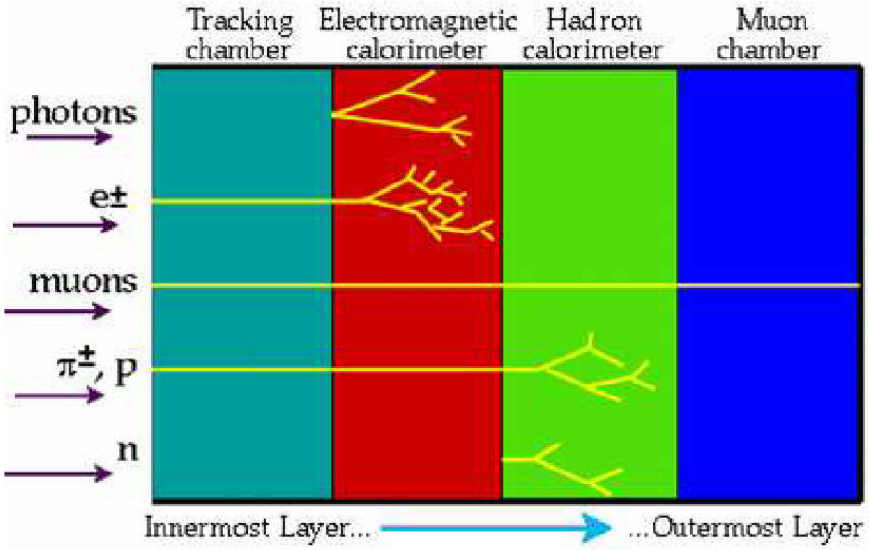

Figure 3.2: Path depths of different particles in the collider detector [34].

trating through the typicall collider detectors. The detailed DØ detector system will be discussed in the following sections.

3.2.1 DØ Coordinate System

In its detector description and data analysis, the DØ experiment uses a right-handed Cartesian coordinate system (x, y, z). The z-axis is along the proton direction pointing south, the y axis is pointing upward and the x axis is directed outward from the center of the Tevatron, which is East at DØ. In additional to these Cartesian coordinates, the cylindrical coordinates (r, ϕ, z) and the spherical angles (ϕ, θ) are also used. The angles ϕ and θ are the azimuthal and polar angles respectively and the r coordinate denotes the perpendicular distance from the z axis. The pseudorapidity η is more convenient to use for relativistic particles, defined as $\eta = -\ln[\tan(\theta/2)]$. It approximates the true rapidity, $y = 1/2 \ln[(E + p_z c)/(E - p_z c)]$, for finite angles, in the limit that $(mc^2/E) \to 0$.

3.2.2 Central Tracking System

The central tracking system consists of the silicon microstrip tracker (SMT) and the central fiber tracker (CFT) and is located inside a 2 Telsa magnetic field produced by a super-conducting solenoid. The main goals of the central tracking system are to measure the helical trajectories of the charged

particles originating from collisions, determine the location of the primary vertex, and identify the b-quark jets. Figure 3.3 is a schematic view of the central tracking system.

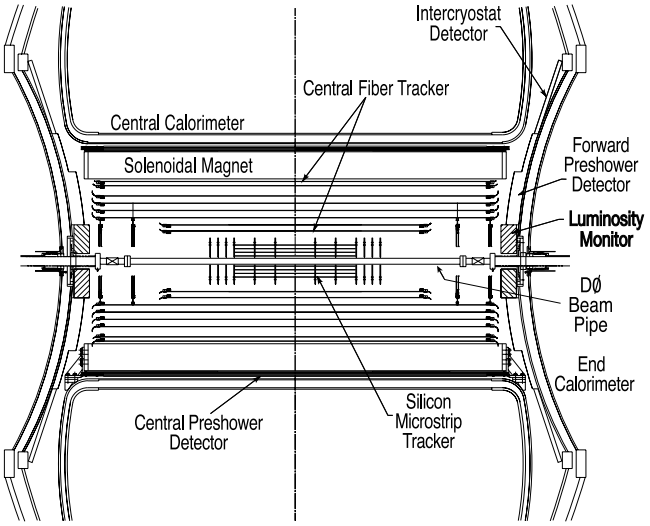

Figure 3.3: Cross-section view of the central tracking system in $x - z$ plane [33].

Silicon Microstrip Tracker

The SMT provides both tracking and vertexing over the nearly full η region covered by the calorimeter and the muon system. The detector has six barrels in the central region, twelve F-disks in forward region, and four H-disks in far forward region. The barrel detectors primarily measure the $r - \phi$ coordinate for the vertices of the particles at low η region, and the disk detectors meausre $r - z$ as well as $r - \phi$ of the vertices for particles at high η. An isometric view of the SMT is shown in Figure 3.4.

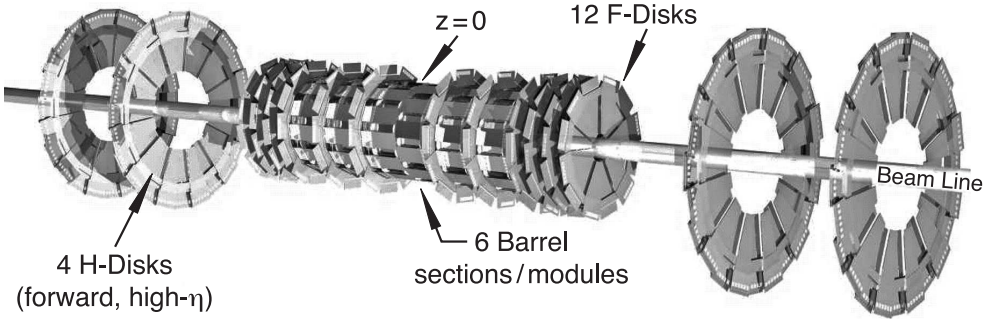

Figure 3.4: The disk and barrel design of the silicon microstrip tracker [33].

In the central region, there are six barrels, each of which has four silicon readout layers. Layers 1 and 2 have twelve silicon modules called "ladders". Layers 3 and 4 have twenty-four ladders each and 432 ladders in total, with 2.7 cm < r < 10.5 cm and $|z|$ < 38 cm. Each barrel is capped with a F-disk at high $|z|$. The F-disks are centered at $|z|$ =12.5, 25.3, 38.2, 43.1, 48.1 and 53.1 cm, while the barrels are located at $|z|$ =6.2, 19.0, and 31.8 cm. Tracking at high $|\eta|$ is provided by the H-disks, which are located at $|z|$ =100.4 and 121.0 cm.

Central Fiber Tracker

The CFT consisits of scintillating fibers mounted on eight concentric support cylinders and occupies the radial space from 20 to 52 cm from the center of the beampipe. The two innermost cylinders are 1.66 m long and the outer six cylinders are 2.52 m long which provide a coverage of $|\eta| \leq 1.7$. Each cylinder supports one doublet layer of fibers oriented along the beam direction and a second doublet layer at a stereo angle in ϕ of $\pm 3^{\circ}$. The scintillating fibers are coupled to clear fiber waveguides which converts the scintillation light to visible light photon counters (VLPCs) for read out. The small fiber diameter (835 μm) gives the CFT an inherent doublet layer resolution of about 100 μm as long as the location of the individual fibers is known to better than 50 μm. Discriminator signals from the axial doublet layers are used to form a fast Level 1 hardware trigger based on the number of track candidates above specified p_T thresholds. Level 1 track candidates are used by the Level 2 trigger, while the L3 trigger uses the full CFT readout information.

3.2.3 Solenoidal magnet

The superconducting solenoidal magnet, added to the detector after Run I, was designed to optimize the momentum resolution, $\delta p_T/p_T$, and tracking pattern recognition within the constraints imposed by the Run I detector. The overall size of the magnet was determined by the available space within the central calorimeter vacuum vessel: 2.73 m in length and 1.42m in diameter. A central field of 2 T was chosen. The solenoid was specified to operate safely and reliably over a twenty-year lifetime with up to 150 cool-down cycles, 2500 energization cycles, and 400 fast dumps.

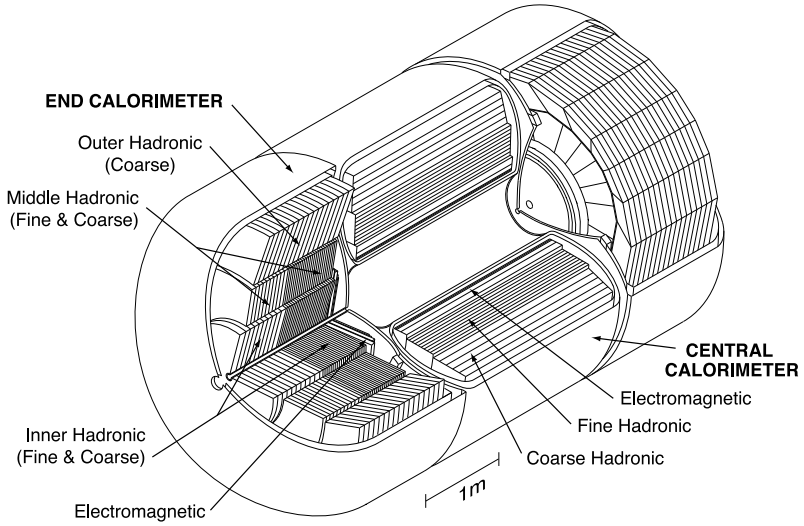

Figure 3.5: Isometric view of the central and two end calorimeters [33].

3.2.4 Calorimetry

The calorimeters are designed to provide energy measurements for electrons, photons, and jets, as well as to assist in identification of electrons, photons, jets, and muons and to measure the transverse energy balance in events. When high energy particles, like electrons, muons, photons, as well as protons, neutrons, travel through the calorimeter, they produce more low energy particles. And those low energy particles, in turn, produce even more particles with even lower energy in a cascade, which is called a "shower". A shower consists of many particles, among which lots of particles carry electric charge. When those charged particles travel through the liquid argon, they cause ionizations. The ionizations are collected giving the electric signals, which are recorded. The depth to which a shower travels and the amont of the collected charges in a shower are proportional to the total energy of the particle that initiated the shower. The energy of both electrically charged and neutral particles can be measured in the calorimeter.

The DØ calorimeter systems consists of three sampling calorimeter (primarily uranium/liquid-argon) and an intercryostat detector. The calorimeters are divided into three parts as shown in Figure 3.5: the central calorimeter (CC) covering $|\eta| \lesssim 1$ and the two end calorimeters, ECN (north) and ECS (south), extending coverage to $|\eta| \approx 4$. Liquid argon is the active medium for each calorimeter, which is located within its own cryostat and kept at temperature of approximately 90 K.

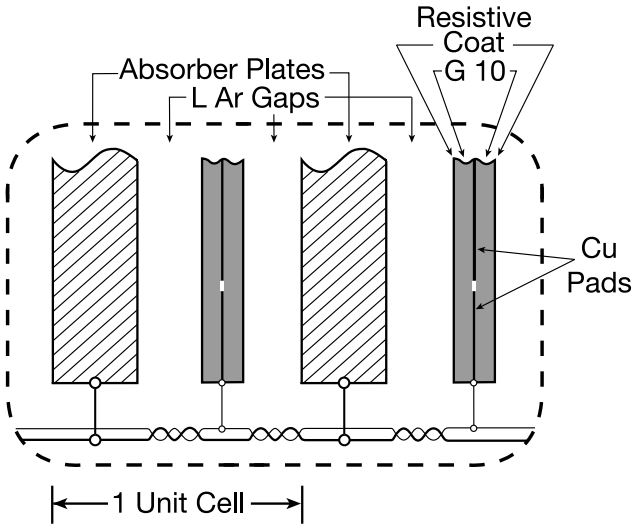

Figure 3.6: Schematic view of the liquid argon gap and signal board unit cell for the calorimeter [33].

Each calorimeter contains an electromagnetic section (EM) closest to the beam line, followed by fine and then coarse hadronic sections. The EM sections use thin plates (3 or 4 mm in the CC and EC, respectively), made from nearly pure depleted uranium. The fine hadronic sections (FH) are made from 6 mm thick uranium-niobium (2%) alloy. The coarse hadronic modules (CH) contian 46.5 mm thick plates of copper (CC) or stainless steel (EC). A typical calorimeter cell is shown in Figure 3.6. It takes approximately 450 ns for the electrons to drift across the 2.3 mm liquid argon gaps when the electric field is established.

The coverage of the calorimeter is incomplete in the pseudorapidity region $0.8 < |\eta| < 1.4$, which corresponds to the gaps between the three separate cryostats. The substantial unsampled material in this region degrades the energy resolution. The intercryostat detector addresses this problem. It consists of the single-cell structures between the central and end cryostats, providing additional layers of scintillator samplings which are attached to the exterior surfaces of the end cryostats.

There are four separate depth layers forming the EM modules in the CC and EC. In the CC, there are three FH modules and a single CH module. In the EC, therer are two inner cylindrical hadronic modules. The FH portion consists of four readout cells; the CH portion has a single readout cell.

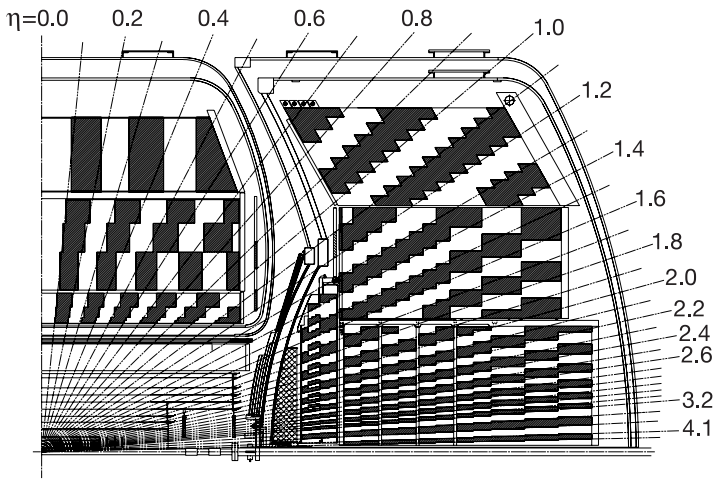

Figure 3.7: Schematic view of a portion of the DØ calorimeters showing the transverse and longitudinal segmentation pattern. The shading pattern indicates groups of cell ganged together for signal readout. The rays indicate pseudorapidity intervals from the center of the detector [33].

Four FH readout cells and one CH section consist each EC middle hadronic modules. The outer hadronic modules of the ECs are made from stainless steel plates. The size of the calorimeter readout cells is shown in Figure 3.7. The FH and CH layers have the size of $\delta\eta + \delta\phi = 0.1 \times 0.1$, and the EM layers have $\delta\eta + \delta\phi = 0.05 \times 0.05$ and larger at $|\eta| > 3.2$.

3.2.5 Muon Detector

The upgraded muon system [35] is divided to two subsystems: the central muon system covering $|\eta| \lesssim 1.0$, and the forward muon system extending coverage to $|\eta| \approx 2.0$. The central muon detector uses the orignal Run-I proportional drift tubes (PDTs), toroidal magnets, and the central scintillation counters. The new forward muon detectors use mini drift tubes (MDTs), including trigger scintillation counters and beam pipe shielding. Figure 3.8 shows the view of the muon wire chambers and the scintillation counter detectors.

The central muon detector consists of a torroidal magnet, drift chambers, the cosmic cap and bottom scintillation counters, and the $A\phi$ scintillation counters. The torroidal magnets, visible in

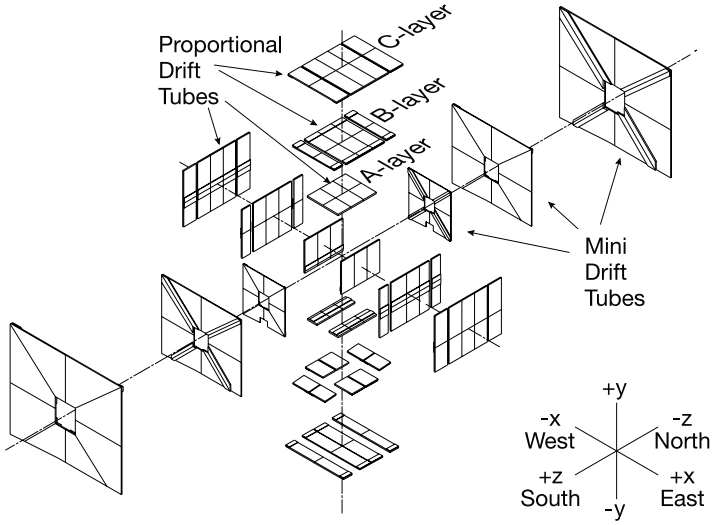

(a) Exploded view of the muon wire chambers.

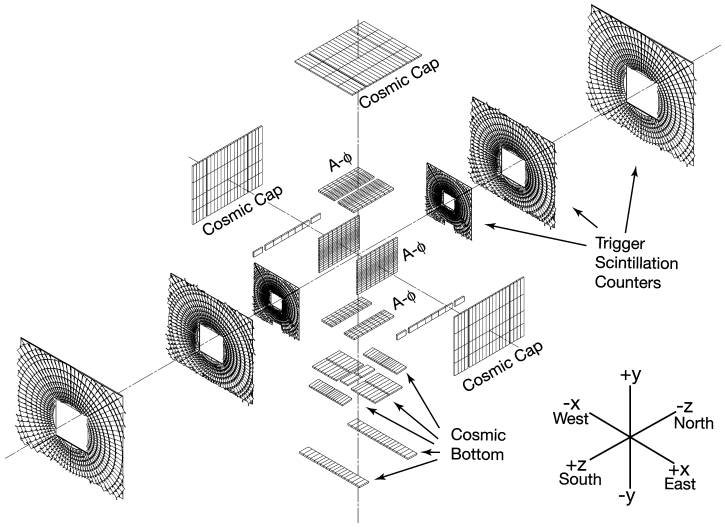

(b) Exploded view of the muon scintillation detectors

Figure 3.8: DØ muon system [33].

Figure 3.1, provide a stand-alone muon system momentum measurement. The torroid coils are operated in series at a current of 1500 A and the magnetic field is about 1.9 T. There are three layers of drift chambers (PDTs) located inside (A layer) and outside (B and C layers) of the central toroidal magnet covering $|\eta| \lesssim 1$. For hits in a PDT, the recorded information is: the electron drift time, the difference ΔT in the signal arrival time between the end of the hit cell's wire and its readout partner's wire, and the charge deposition on the inner and outer vernier pads. The drift distance resolution is $\sigma \approx 1$ mm, dependent on both ΔT and the charge deposition. The cosmic cap and bottom scintillation counters are located on the top, side and bottom of the outer layer of the PDTs. They provides a fast timing signal to associate a muon in PDT with the bunch crossing and to reject the cosmic rays. The $A\phi$ scintillation counters covers the A-layer PDTs between the calorimeter and torroid, and provide a fast detector for triggering on and identifying muons while rejecting out-of-time backgrounds. The time-of-flight of the particles are measured in the scintillation counters and used in our search.

The forward muon system covers $1.0 \lesssim |\eta| \lesssim 2.0$ as shown in Figures 3.1 and 3.8. It is divided into four major sub-detector: the end toroidal magnets, three layers of MDTs, three layers of scintillation counters, and shielding around the beam pipe. Mini drift tubes (MDT) were used for muon track reconstruction and chosen for their short electron drift time, good coordinate resolution, radiation hardness, high segmentation, and low occupancy. The efficiency of the MDTs is 100% in the active area of the cells for tracks that are perpendicular to the MDT plane and the overall plan efficiency is approximately 95 %. The momentum resolution of the forward muon system is limited by multiple scattering in the torroid and by the coordinate resolution of the tracking detector, which is about 0.7 mm per hit. The standalone momentum resolutions of the forward muon system is about 20% for p_T below 40 GeV/c. The overall muon momentum resolution is defined by the central tracking system for muons with momentum up to approximately 100 GeV/c. Three layers of scintillation counters are mounted inside (A layer) and outside (B and C layers) of the torroid and employed for triggering on events with muons. The shielding around the beam pipe significantly reduces the background from beam halo, those due to proton and antiproton remnants. The long-term reliable operation of the muon system is ensured by the reduction in this background along with the use of radiation-hard detectors.

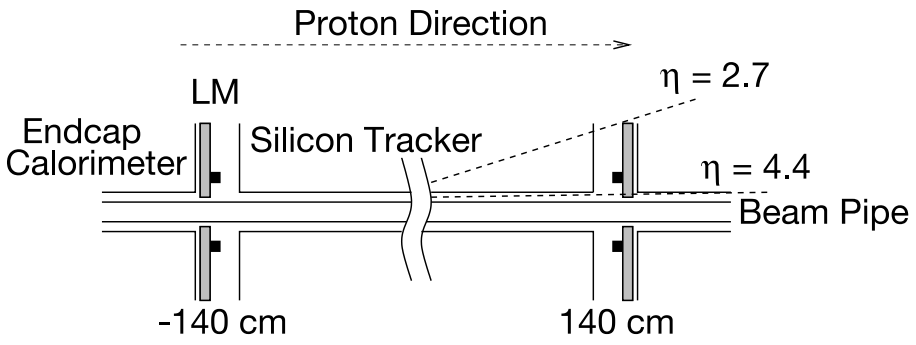

Figure 3.9: Schematic drawing showing the location of the LM detectors [33].

3.2.6 Luminosity

The Tevatron luminosity at the DØinteraction region is determined by the luminosity monitor (LM) which detects inelastic $p\overline{p}$ collisions using a dedicated detector. The LM also measures the beam halo and makes a fast measurement of the z coordinate of the interaction vertex.

The LM detector consists of two arrays of twenty-four plastic scintillation counters with photomultiplier (PMT) readout located at $z = \pm 140$ cm covering $2.7 < |\eta| < 4.4$, as shown in Figure 3.9.

The luminosity $\mathcal{L}$ is determined from the average number of inelastic collisions per beam crossing $\overline{N_{LM}}$ measured by the LM

$$\mathcal{L} = \frac{f\overline{N_{LM}}}{\sigma_{LM}} \tag{3.1}$$

where f is the beam crossing frequency and σ_{LM} is the effective cross section from the LM that takes into account the acceptance and efficiency of the LM detector. Distinguishing $p\overline{p}$ inelastic interactions from the beam halo backgrounds is the key to measuring the luminosity accurately. Precise time-of-flight measurements of the particles traveling at small angles with respect to the beams are used to reject the backgrounds.

3.2.7 Triggering

A trigger system is necessary to select the interesting physics events to be recorded with the high luminosity and interaction rate delivered by the upgraded Tevatron. The maximum collision rates at

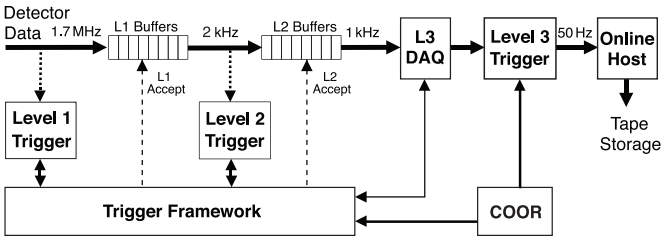

Figure 3.10: Overview of the DØ trigger and data acquisition systems.

the interaction point inside the DØ detector is 2.5 MHz, and only 100 of the most interesting events per second are written to tape storage for later analysis. The rate deduction is realized by a three-level trigger system, which was upgraded based on the original Run I trigger and data acquisition system. An overview of the trigger and data acquisition system is shown in Figure 3.10.

The first level (L1) trigger system is built from custom fast electronics. It comprises a collection of hardware trigger elements and provides an accept rate at about 2 KHz from the 2.5 MHz input rate. Every event is examined for interesting features. The calorimeter trigger (L1Cal) looks for transverse energy deposition patterns; the central track trigger (L1CTT) and the muon system trigger (L1Muon) compare tracks, separately and combined, measuring the transverse momentum. The L1 forward proton detecter trigger (L1FTD) is used to select diffractively produced events by triggering on the protons or antiprotons scattered at samll angles. The trigger framework (TFW) gathers digital informations from all specific L1 trigger devices and decides whether an event is to be accepted for further trigger examination. The L1 trigger must arrive at the trigger framework within 3.5 μs in order to participate in the trigger decision. The maximum readout rate of the participating subsystems and the minimal readout deadtime limit the rate of the L1 trigger acceptance rate. All events awaiting L1 tirgger decisions are pipelined to minimize the deadtime.

The second stage (Level 2 or L2) is built from a combination of custom electronics and generic processors. It combines information from sub-detector systems and applies more complicated selection criteria in order to reduce the accept rate by a factor of two at approximately 1 KHz. The L2 was designed to handle an input rate up to 10 KHz, although the output rate from the Level 1 has a maximum at 2 KHz. The Level 2 trigger uses the preprocessors which collect data from the front-ends of detector subsystem and the L1 trigger system to form physical objects. Across-detector data

are combined at L2 to form even higher level physical objects. The L2 Global processor makes an event selection decision based on the set of the L1 128 trigger selection bits and on additional criteria. Events passing the L2 selection are tagged and all the data chunk associated with them are sent to L3.

The candidate events passing the L1 and L2 triggers are sent to the third level (L3) trigger, a commodity processor farm. Complicated algorithms combine and reconstruct the full data for each events and on average reduce the acceptance rate to approximately 100 Hz. Those selected events are recorded to tape for offline reconstruction and further analysis purpose. L3 performs a limited reconstruction of events as a high level fully programmable software trigger. At an L3 input rate of 1 KHz, about 235 ms/event are avaible for unpacking, reconstruction, and filtering. Both the complete physics objects and the relationships among them are used to make the L3 trigger decisions. Candidate physics objects and their relations are generated by object-specific software algorithms (filter tools). All tools cache their results to expedite possible multiple calls within the same event, and add L3 object parameters to the data block if the event is accepted. Filters make the individual calls to the tools, and define the specific selection criteria employed by a tool or imposed on its results. Filters can access the results of other filters so that the results of a previous filter can be included in the parameter sets. Each trigger list download can change this information as part of the trigger programming. The trigger list programming includes blocks of filter scripts specifying filters and defining the L3 trigger condition for each L3 trigger bit. Each L3 filter script is associated with a L2 bit and each L2 bit can be associated with multiple L3 scripts. Only if all filters in a script are fired, does the event pass the L3 trigger and is sent to be recorded on tapes.

The COOR package, the central coordination process, handles the overall coordination and control of the trigger system. Running on the online host, COOR interacts directly with the trigger framework (L1 and L2 triggers) and the DAQ supervisior (L3 triggers).

3.2.8 Data acquisition systems

The Level 3 data acquisition (L3DAQ) [36] transports fully digitized data from the sub-detector systems to L3 trigger filter processors running on the L3 trigger farm. The L3 DAQ system is built based on commodity hardware installed with the Linux operating system and Ethernet communications. The system is built around a single Cisco 6509 Ethernet switch.

When an event passes the L2 trigger, up to 63 VME crates will be read out, each containing 1 to 20 kB of data distributed among VME modules. The total event size can reach more than 300 kB under normal physics running conditions. The event size can be 2 MB under calibration run conditions.

A single board computer (SBC) in each crate reads out the VME modules and send the event fragments over an Ethernet to a L3 farm node. The dedicated SBC called Routing Master (RM) sends out routing instructions selecting a specific L3 trigger farm node for each event. Each Level 3 farm node sends information to the RM about its load and the RM makes a decision as to which event is sent to which node.

After all the fragments of an event arrive at the node, an Event Builder (EVB) process collates all the fragments into a complete event and places it in shared memory buffers where it is processed by several Level 3 filter process. The RM makes the routing decision based on the fired L2 triggers, the number of available buffers in each farm node, and the run partition information. On the farm nodes, complete events are built by collecting all the event fragments and processed by L3 trigger processes. Events passing L3 trigger criteria are sent via a seperate network to be stored to tape. Further information about the hardware, software, and monitoring programs are detailed in Appendix A.

The peak instantaneous luminosity of the Tevatron Collider has steadily increased during the Run II period from less than $100 \times 10^{30} cm^{-2} s^{-1}$ to $350 \times 10^{30} cm^{-2} s^{-1}$. The L3 DAQ system has been upgraded to accommondate the increasd luminosity [37]. The event size has grown, due to the higher occupancy of the detectors. At the highest current luminosities the average event size has peaked at 350 kB, compared to a size of 250 kB at the lowest luminosities. The L2 accept rate is kept at around 1 kHz, which is the design value. The L3 output rate was limited to 50 kHz before 2006, while 100 Hz is now standard, and in routine operation an even higher rate is used at the beginning of the store. Increasing the number of farm nodes (from 82 in 2004 to more than 300 at present) and other upgrades in the system help to achieve this goal.

Chapter 4

Event Reconstruction

The data recorded by the DØ data acquisition system is stored on tape in raw data format, which contains the information directly from the detector as hits in the central tracking system, digitized counts in the calorimeter cells, etc. The raw data needs to be reprocessed and converted to the physics objects for analysis. The offline process is called event reconstruction, accomplished by a collection of complex software algorithms, "d0reco". There are six types of phyics objects, which are vertex, track, electron, jet, missing transverse energy ($\not\!\!E_{\rm T}$) , and muon. The reconstruction process is performed in the following steps:

- **Detector specific processing**
  - Detector data blocks are unpacked
  - Raw information is decoded
  - Readout channels are associated with physical detector channels
  - Calibration constants are applied
- **Pre-reconstruction**
  - Spatial locations of hits in the tracking system are converted from the recorded digitized signals.
  - The signals from calorimeter cells are converted to energies.
- **Tracking and Clustering**

  - The track hits are combined to form tracks, and the energy deposits in calorimeter are grouped into clusters.

- **Vertexing**

  - The calculation of the location of the $p\bar{p}$ interaction to determine various kinematic quantities.
  - Reconstruction of primary vertex candidates
  - Identification of displaced secondary vertices

- **Particle Identification**

  - The tracks and clusters are combined to form candidates of electrons, photons, jets, and muons.
  - Identification of heavy-quark (b and c) jets, as well as τ candidates
  - Reconstruction of the missing transverse energy $\not\!\!E_{\mathrm{T}}$

In this chapter, we discuss the details of the above steps that are relevant to this analysis.

4.1 Tracking

The goal of global tracking is to find and fit the tracks in an event with the data from one or more DØ subdetectors. Charged particles deposit energy in the central tracking system of DØ detector, either silicon strips (SMT) or scintillating fibers (CFT), or both. The energy deposit in SMT and CFT will be converted to electric signals called hits. Two or more adjacent hits clustered together are defined as a cluster. These clusters are the put into the track fitting algorithm to reconstruct tracks.

There are three track finding algorithms supported and developed by DØ Global Track Finder (GTR) group, which are the Histogramming Track Finder (HTF), the Alternative Algorithm (AA), and a road-following method (GTR) providing a common infrastructure for propagation, refitting, and multiple scattering and energy loss correction.

The HTF [38] method is based on the Hough transform, which reduces the combinations of hits so that the HTF method is well suited for complicated cases with $10^4 - 10^6$ hits with high

local detector occupancies. It starts with the hit preselection using the histogramming technique. The trajectory of the charged particle in the plane perpendicular to the direction of the field can be characterized by three parameters, e.g. $(\rho, d_{0,}\phi)$, where $\rho = qB/p_t$ is the curvature (q is charge, B is the magnetic field, and $p_t = \sqrt{p_x^2 + p_y^2}$ is the transverse momentum), d_0 is the distance of closet approach to (0, 0) (*impact parameter*), and ϕ is the direction of the track at the point of closest approach to (0, 0). In case of small impact parameters $d_0 \sim 0$, every pair of points for each trajectory in *coordinate space* (x, y) is transformed into a single point in *parameter space* (ρ, ϕ) by the Hough transformation. Figure 4.1 is an example of the Hough transformation. Each hit in the coordinate space corresponds to a line in the parameter space (a band if the errors are included). The intersect point of all those lines corresponds to the parameters of the trajectory. In the real algorithm, all the hits from the same track will produce a peak in the histogram, while points from different tracks will distribute randomly. The output of the preselection is a set of templates. Each template is a track candidate consisting of several hits, with approximately known trajectory parameters. These templates are further processed applying the 2D Kalman filter with material effects in order to discard the fake templates, remove the wrong hits, and accurately calculate the track parameters.

The Alternative Algorithm (AA) [39, 40] is based on well-known methods of pattern recognition and developed specially for the needs of the Higgs search and many other studies at Tevatron. It can perform track reconstruction with high efficiency, reduce the fake track rate, and reconstruct the low momentum and large impact parameter tracks with the same high quality as the high momentum tracks. AA starts from any combination of three 2D-measurements (hits) in SMT barrels or disks, and extraplotes each track to the next layer of the SMT or CFT repeatly. Track reconstruction starting from SMT is motived by significantly fewer combinations from association of axial and stereo measurements. This track reconstruction allows particles to decay, interact or scatter in the detector material. A certain number of misses (i.e., no hits) in layers are allowed to improve the efficiency. The fitting algorithm continues until there are three consecutive misses in a row or the end of the detector is reached. The overall fit must satisfy a χ^2 cut when adding hits to the track. Since the fitted tracks can share hits with other tracks, the AA requires that the number of shared hits be less than 2/3 of the total hits in the track. Primary vertices are used to reduce the fake track

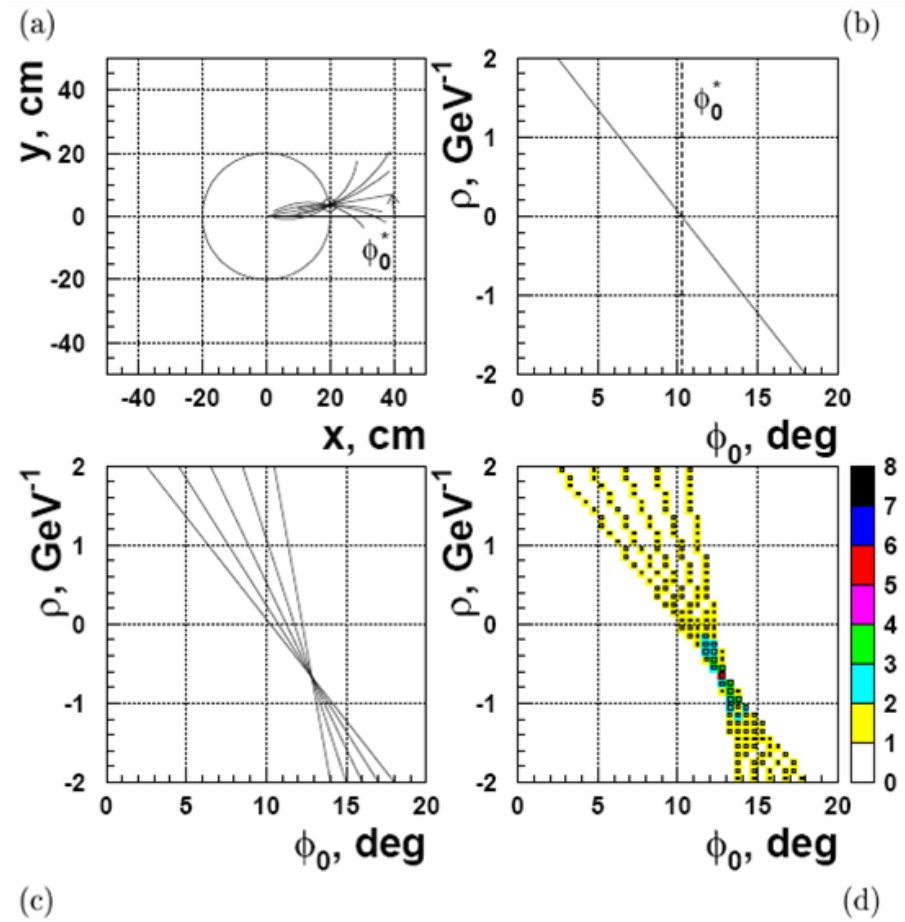

Figure 4.1: Illustration for an example of the Hough transformation. This example is for 1.5 geV muon track. (a) The family of trajectories containing a given hit. (b) The geometric place of all trajectories containing a given hit in parameter space. (c) Curves from different hits intersect at one point corresponding to the track parameters. (d) The point of intersection can be seen as a peak in the (ρ, ϕ) histogram [38].

rate. "CFT only" tracks are also allowed to be reconstructed if there are fewer than three hits in SMT.

The Global Track Finder (GTR) algorithm is based on TRF++ with specific paths (roads) during track finding. TRF++ is a software system for finding and fitting tracks in any particle physics detector. It is object-oriented, designed with considerable emphasis on reusablility and extensibility.

4.2 Vertices

The goal of vertexing is to provide reliable primary and secondary vertices with the global tracks as inputs for an event. The primary vertex (PV) is the location of the hard scatter, which triggers the event (i.e. the interaction point). The position of the primary vertex is the source of precise measurement of many kinematic quantities, such as the transverse momentum of tracks and the transverse energy of the jets for many physics analyses. The x and y locations of the PV fluctuates within $40\,\mu m$ (1σ) between events, while the z location is roughly a Gaussian distribution with a σ of ~ 30 cm.

Vertex reconstruction consists of two main steps: vertex finding, which is a pattern recognition problem determining which particle tracks belong to each vertex, and vertex fitting, which is an statistical problem in accurate estimation of the vertex position and the momentum of the tracks from the vertex. One main challenge, especially at high luminosities, is to discrimate tracks from secondary vertices with small decay length and additional minimum bias interactions close to the primary vertex. An adaptive algorithm for primary vertex reconstruction [41] is employed in order to improve the recongition of the outliers (association of tracks to vertices) and to better separate between primary and secondary vertices. The main idea of the method is to reduce the contribution from distant tracks to the vertex fit.

In the adaptive algorithm, the reconstruction and identification of PV consists of three steps: track selection, vertex fitting, and vertex selection. First, the tracks are required to have $p_T > 0.5\,GeV/c^2$ and two or more hits in SMT if they are in the SMT geometric acceptance. Then tracks are clustered within $2\,cm$ of each other by a z-clustering algorithm, which is used to identify tracks belonging to different interactions. During the vertex fitting stage, the location and width of the beam is determined by fitting all selected tracks within each z-cluster into a common vertex, which

is performed with the Kalman Filter vertex fitting algorithm. Tracks with the highest χ^2 contribution to the vertex are removed, until the total vertex χ^2 per degree of freedom is smaller than 10. Then, the tracks are selected to have $(DCA/\sigma_{DCA} < 5)$, where σ_{DCA} is the standard deviation of the distance of closest approach (DCA) to the previously determined beam position.

The selected tracks are then fitted into a common vertex using the Adaptive vertex fitter algorithm. In the Adaptive fitting algorithm, each track error is re-weighted by the following funcion according to the χ^2contribution to the vertex:

$$w_i = \frac{1}{e^{(\chi_i^2 - \chi_{cutoff}^2)/2T} + 1} \tag{4.1}$$

where χ_i^2 is the χ^2contribution of track i to the vertex, χ_{cutoff}^2 is the distance where the weight function drops to 0.5, and T is a parameter that controls the sharpness of the function. At the beginning, all PV track candidates are fitted with the Kalman Filter algorithm and all track weights $(w_i(\chi^2))$ are set to 1.0. The weight of each track used in the fit is recalculated according to the χ^2 distance to the new fitted vertex. Track i will be removed from the fit if $w_i(\chi^2) < 10^{-6}$. The algorithm iterates until the total weight error in each iteration $(max|w_i - w_{i-1}| < 10^{-4})$ and the total number of iterations is smaller than 100.

Identification of the hard scatter and of additional minimum bias (MB) vertices of the event is the last step in the PV reconstruction. An assumption is made that tracks from hard interactions have higher p_T than those from MB. For each cluster, the highest multiplicity vertex is selected and stored in the "selected" vertices list. Then all tracks within certain distance around the selected vertex are used to compute the probability that the vertex comes from an MB interaction. The vertex with the smallest MB probability is selected as the PV.

4.3 Calorimeter Precessing

The unphysical energy deposits and noise are removed from the calorimeter data before reconstructing the objects. During data taking, due to hardware problems, high energy deposits can show up in individual cells, which are called "hot". Those hot cells should be suppressed in order to keep data taking rates acceptable. At the L3 trigger and in the early stages of the offline processing, such hot cells are further suppressed and the resulting unphysical high energy deposits are reset. Noise

is similarly removed. There are several sources for the noises: electronics, uranium decays, pile-up from interactions in previous bunch crossing, etc.

Electrons, photons, and jets are reconstructed using the cone algorithm. Energy deposits in a cell are represented in a massless four-vector pointing along the cell's direction from the center of the detector. The cone algorithm starts by selecting seeds with the highest E_T calorimeter towers in the event above the threshhold. The cone is defined as

$$\Delta\mathcal{R} = \sqrt{(\Delta\eta_{det})^2 + (\Delta\phi_{det})^2} \tag{4.2}$$

where $\Delta\eta_{det}$ is the difference in pseudorapidity between a tower and the seed tower, and $\Delta\phi_{det}$ is the difference in the azimuthal angle. The four-vectors of towers within a fixed cone size are summed to the seed vector. The centroid of the cone is calculated from contributions from all the particles within the cone. The cells within a cone are the removed from consideration, and a new seed is formed from the remaining highest E_T tower.

4.4 Electrons

High-transverse momentum isolated electrons are crucial for many analyses, including top quark measurements, electroweak processes and searches for physics beyond Standard Model (SM). Therefore, the identification of such electrons is essential in order to selecting real electrons efficiently while suppressing the mis-identification rate. Hig-p_T electrons [42] are reconstructed using signatures they leave in three sub-detector systems: the energy deposits in both the calorimeter and central preshower detector and the trajectory in the central tracking system. The identification of high-p_T electrons involves three stages.

First, localized energy deposits in the calorimeter are used to reconstruct the electrons and photons, which have very similar shower shapes. The concentrated clusters of energy for electrons and photons are mainly deposited in the electromagnetic (EM) layers of the calorimeter. The standard EM clustering algorithm at DØ is the tower based cone algorithm, where the calorimeter cells with the same η and ϕ are grouped together to form towers. A readout-tower is of size 0.1×0.1 in $\Delta\eta \times \Delta\phi$ and a trigger tower is of the size 0.2×0.2 in $\Delta\eta \times \Delta\phi$. In calorimeter, an EM tower is

defined as the sum of the measured energy in all four EM layers plus the first hadronic (FH1) layer. Starting with the highest transverse energy (E_T) EM tower, adjacent EM towers ($E_T > 50\,MeV$) within the cone, $\mathcal{R} = \sqrt{\Delta\eta^2 + \Delta\phi^2} = 0.4$, around the hottest tower, are added together to form EM clusters in the central calorimeter (CC). In the endcap calorimeter (EC), EM clusters are a set of adjacent cells with a transverse distance of less than 10 cm from an initial cell. The fraction of energy in the EM layers, defined as the EM fraction, is

$$f_{EM} = \frac{E_{EM}}{E_{tot}} \tag{4.3}$$

where E_{EM} is the cluster energy in the EM layers and E_{tot} is the total energy of the cluster deposited in all layers within the cone. The cluster must have $f_{EM} > 90\%$ in order to be selected as an EM cluster or electron/photon candidate. Also, the cluster must be isolated in $(\eta - \phi)$ space with an isolation fraction < 0.2. The isolation fraction is defined as

$$f_{iso} = \frac{E_{tot}(R < 0.4) - E_{EM}(R < 0.2)}{E_{EM}(R < 0.2)} \tag{4.4}$$

where $E_{tot}(R < 0.4)$ is the total energy in the towers within a cone of radius $R = 0.4$ around the cluster direction and is the sum over the entire depth of the EM and FH; the $E_{EM}(R < 0.2)$ is the energy in the towers in a cone of radius $R = 0.2$, which is summed over EM only. EM showers will appear in the preshower detectors for electrons and high-p_T photons. The 3D clusters reconstructed in the preshower detectors are then matched to the EM clusters.

After the electrons are reconstructed, the EM clusters are identified to reject the background which contaminates the reconstructed sample. The shower shape information is used to differentiate electrons (and photons) from hadrons due to the different development of EM and hadronic showers. In order to obtain the best classification from hadrons, both longitudinal and transverse shower shapes are considered, as well as the correlations among the energy deposits in the calorimeter (preshower) cells. A covariance matrix (H-Matrix) [43] technique is used, in which a 7-dimensional covariance matrix is built up with a set of variables describing the shower shapes.

The EM cluster is required to have an associated central track in order to suppress the QCD background. The track is extrapolated into the EM layer of the calorimeter. A $Prob(\chi^2_{spatial})$ is

defined as

$$\chi^2_{spatial} = \left(\frac{\delta\phi}{\sigma_\phi}\right)^2 + \left(\frac{\delta z}{\sigma_z}\right)^2 \tag{4.5}$$

where $\delta\phi$ is the angle difference in ϕ and δ_z is the spatial difference in position between the track impact and cluster; and σ_ϕ and σ_z are the experimental resolutions. $Prob(\chi^2_{spatial})$ is computed for every availible track, and the one with the highest $Prob(\chi^2_{spatial})$ is matched to the EM object.

The track match confirmation does suppress the QCD background efficiently. However, there is still a serious problem with the "fake electron" background. In order to distinguish real electrons from fakes, certain characteristics of the fakes should also be taken into account. Likelihood-based confirmation has been proven to be an efficient technique of discrimating the electron signals from backgrounds since the entire shape of the signal and background distributions are considered. The informations from several detector sub-systems is combined in the likelihood function with just one signal output variable. A likelihood discriminant is computed as :

$$\mathcal{L}_n(\mathrm{x}) = \frac{P_{sig}(\mathrm{x})}{P_{sig}(\mathrm{x}) + P_{bkg}(\mathrm{x})} \tag{4.6}$$

where $P_{sig}(\mathrm{x})$ and $P_{bkg}(\mathrm{x})$ are the probability for a given EM object to be signal or background, and x is the vector of likelihood variables. By assuming that these variables are uncorrelated, the overall probability for the event is simply the product of all these probabilites from the probability distributions, i.e. $P(\mathrm{x}) = \prod_i P(x_i)$. The candidate is more signal-like if $\mathcal{L}_n(\mathrm{x})$ is closer to 1; the closer $\mathcal{L}_n(\mathrm{x})$ tends to 0, the candidate is more background-like. The current version of electron likelihood methods takes seven quantities as inputs, which are the information from both calorimeter and the central tracking sytem:

- f_{EM}.
- H-Matrix χ^2_{Cal7}.
- E_T/p_T.
- $Prob(\chi^2_{spatial})$.
- Distance of closest approach (DCA), the shortest distance of the selected track to the line parallel to the z-axis passing through the primary vertex positon.

- Number of tracks in a $\Delta R = 0.05$ cone, around and including the candidate track. This is designed to suppress the fake electrons from photon conversions. A real electron should just show one track, while in these background events more than one track is expected.

- Total track p_T in a $\Delta R = 0.4$ cone, around, but excluding the candidate track. This is to remove π^0 produced accompanied with charged hadrons. The tracks from jets tend to have large p_T, however, good electrons tend to have extremely low p_T.

In addition, two more variables are also considered:

- Isolation fraction f_{iso}.

- Total track p_T in the halo $0.05 < \Delta R < 0.4$.

4.5 Jets

Jets are reconstructed with the cone algorithm with calorimeter information. Towers of size $\Delta\eta \times \Delta\phi = 0.1 \times 0.1$ with energy above 1 GeV are used as seeds in preclusters, which are formed by combining adjacent calorimeter towers with a radius of 0.3 to the seed tower. Jet clusters are defined by preclusters in a cone size $\Delta\mathcal{R} = 0.5$ or 0.7 around the jet centroid. Jets with $E_T < 6\,GeV$ are discarded. If two jets share the same tower a split/merge fraction is calculated, which is the ratio of the shared energy of the jets to the energy of the least energetic jet. If the ratio is larger than 50%, the jets are merged and a new centroid is calculated. Otherwise, the shared towers are split between the jets. The cone reconstruction algorithm [44] can be applied both at the stable particle (particle jet) and the reconstructed calorimeter tower (calorimeter jet) level.

After jets are reconstructed with the cone algorithm with $\Delta\mathcal{R} = 0.5$, they are selected by the listed cuts [45] below:

- Electromagnetic (EM) fraction >0.05,

- EM fraction < 0.95,

- CH fraction < 0.40,

- ratio of energy in hottest cell to that in the second hottest cell < 10,

- Minimal number of cells containing 90% of the cell's energy > 1.

For jets with $|\eta| < 2.0$ with a hard matched track, further requirements need to be fulfilled:

- $p_T > 2.0\, GeV$,
- $d\mathcal{R} < 0.5$,
- $\chi^2 < 3$.

Similarly, jets with no track match are required to pass a track veto:

- $p_T > 0.5\, GeV$,
- $d\mathcal{R} < 0.5$,
- $\chi^2 < 3$.

The jet ID has uniform and high efficiencies for all jet kinematics after taking the detailed geometry and noise characteristics of the DØ calorimeter into account. The efficiency of all the jet ID for physical jets is at 98-99% level at all η and p_T , except for Electro Magnetic Fraction (EMF). The motivation for the EMF cuts is to remve the jets dominated by hadronic noise and leads to 95% efficiency. The cut on the Coarse Hadronic Fraction (CHF) is driven clearly by removing jets dominated by noise typical to the CH calorimeter. Better understanding of such jets from and dominated by CH noise results in a higher signal efficiency for CHF. New signal efficient L1 cuts start to use the better performance from the new L1 confirmation algorithm and warrant further study which is likely to result in tighter cuts for most jets.

The jet ID cuts for p17 (Run IIa) data are:

A jet passes the maximal CHF cuts if:

- it has $CHF < 0.4$, or
- it has $CHF < 0.6$ and $8.5 < |\eta_{det}| < 12.5$ (in the ECMH) and $n90 < 20$, or,
- it has $CHF < 0.44$ and $|\eta| < 0.8$ (central), or,
- it has $CHF < 0.46$ and $1.5 < |\eta| < 2.5$ (end cap excluding forward regions).

A jet passes the minimal EMF cuts if:

- it has $EMF > 0.05$, or
- it has $1.3 > ||\eta_{det}| - 12.5| + max(0, 40 \times (\sigma_\eta - 0.1))$ (in the No EM Gap).
- it has $EMF > 0.03$ and $11.0 < |\eta_{det}| < 14.0$ (in the No EM Gap), or,
- it has $EMF > 0.04$ and $2.5 < |\eta|$ (forward).

A jet passes the minimal $L1_{ratio}$ cuts if:

- it has $L1_{ratio} > 0.5$,or,
- it has $L1_{ratio} > 0.35$ and$p_T < 15$ and $1.4 < |\eta|$ (end cap), or,
- it has $L1_{ratio} > 0.1$ and$p_T < 15$ and $3.0 < |\eta|$ (forward), or,
- it has $L1_{ratio} > 0.2$ and $p_T \geq 15$ and $3.0 < |\eta|$ (forward).

where $L1_{ratio}$ is calculated excluding the massless gap energies from the precision (and L1) sum.

The accurate knowledge of the energy of jets plays a very important rule on many physics measurements at hadron colliders. The precise determination of the jet energy scale (JES) [46, 47] is a challenging project and involves corrections from physics, instruments, and the jet-reconstruction algorithm. Figure 4.2 is the sketch of the evolution of a jet in the calorimeter from the hard scatter parton. The goal of the JES correction is to correct the calorimeter jet energy back to the particle jet level before interacting with the detector. During parton evolution, there is some energy found at large angles with respect to the original parton direction resulting from hard gluon radiation, which JES is not designed to correct for.

The JES correction is defined in Equation 4.7

$$E_{jet}^{particle} = \frac{E_{jet}^{raw} - O}{E_\eta \times R \times S} \tag{4.7}$$

where quantities in the equation are defined as following:

- $E_{jet}^{particle}$: corrected particle jet energy

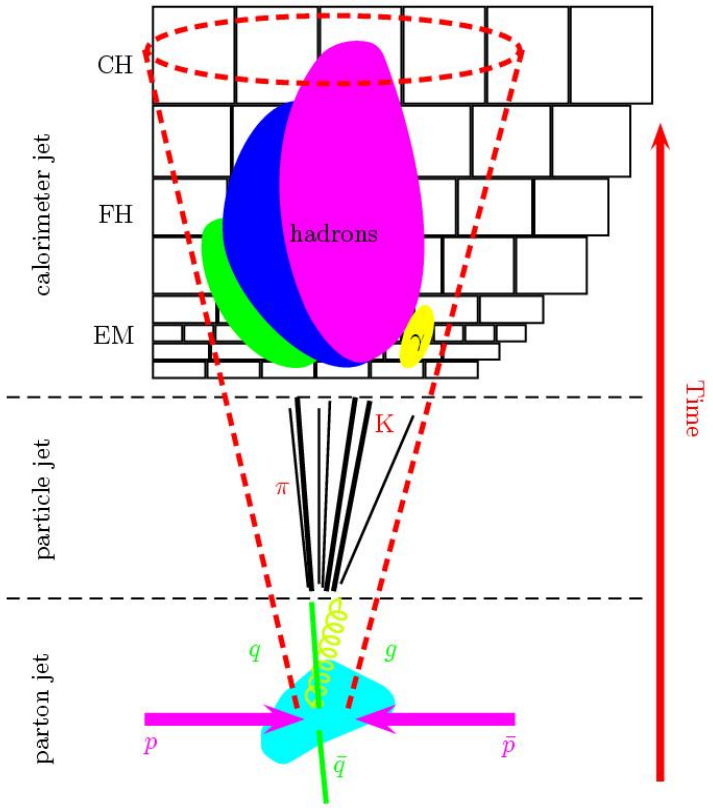

Figure 4.2: Sketch of the evolution from the hard scatter parton to a jet in the calorimeter [47].

- E_{jet}^{raw}: uncorrected jet energy
- O : offset energy correction
- E_{η}: relative response correction (η-intercalibration)
- R : absolute response correction
- S : showering correction

As shown in the above equation, a series of subcorrections is involved in the JES correction procedure. These corrections are derived and applied in a sequential order and estimated separately for collider and simulated data (i.e. Monte Carlo). The offset correction is the first step, which subtracts the energy not associated with the hard scatter (e.g. electronic noise or multiple proton interactions in the same bunch crossing). An absolute response correction is the second step, which is applied to calorimeter central jets and determined by balancing the transverse momentum in the photon+jet events. This correction is ~30%, the largest in magnitude and accounts for effects such as energy loss in uninstrumented detector regions, the lower calorimeter response to hadrons as compared to electrons or photons, etc. Relative response correction is introduced in order to calibrate the response in energy of the calorimeter as a function of jet pseudorapidity. Then, the showering correction takes into account the energy deposited outside/inside the calorimeter jet cone from particles inside/outside the particle jet as a result of shower development in the calorimeter, magnetic field bending, etc. In the end, the remaining biases are applied to JES, which includes calorimeter zero suppression effects, "topological" bias in absolute calibration due to kinematic cuts in selection of $\gamma + jet$ events, etc.

4.6 Muons

The three-layer muon detector in DØ is designed to identify muons in combination with the central tracking system and the calorimeter. The muon detector system covers up to a pseudo-rapidity $|\eta| = 2$, which is more than 90% of the angular acceptance for DØ. Muon detectors lay outside the central tracking system and the calorimeter as the outmost system of the DØ detector. As another type of tracking system with its toroid magnet, the momentum of muons is also measured in the

muon system. Since most of the particles cannot penetrate through the calorimeter, the particles registered in muon system are dominated by real muons. In other words, the muon system provides unambiguous muon identification. A muon, identified based on the muon detector information, is defined as a "local muon".

The central tracking system (SMT and CFT) provides a more accurate momentum measurement and a higher spatial resolution than the muon detector. It also finds tracks in the angular acceptance of the muon system with high efficiency. A muon with a matched central track is called as a "central track-matched muon". In the case of the central track-matched muons, the default muon kinematics come directly from the matched central tracks, which have better resolution than the local muons.

A third independent confirmation of a muon can be derived from the minimum ionization particle (MIP) signature in the calorimeter. The capability to identify muons in calorimeter is called as "Muon Tracking in the Calorimeter" (MTC) and is under development.

The certified Muon Identification (MuonID) definitions are described for p17 data in[48]. They are obtained from versions of the DØ event reconstruction software and the p18 version of d0correct package.

At the reconstruction level, several improvements have been applied. For example, during the combination of the local tracking in the muon system, the number of hits and χ^2 are both considered for quality control. As described in sect. 3.2.5, the muon system consists of three layers in which position measurements are made: the A-layer before the iron torroid, and the B- and C-layers after the torroid. The matching of the central tracks to the BC segments in the muon system are also improved. PDT information is used to improve ϕ resolution in the central A-layer.

Two parameters are used to classify the reconstructed muon candidates, which are muon *type* and muon *quality*. Muon *type* is defined by the variable *nseg*. If *nseg* is positive, then the reconstructed local muon has a successfully matched central track. Negative value of *nseg* means that there is no matched central track to the local muon. Value zero means that there is a central track however no local muon. In this case, either there are not enough hits in the muon system to format a local muon, or there is only MTC found. The absolute value of *nseg* indicates that the local muon is made of only A-layer hits ($|nseg| = 1$), only B or C-layer hits ($|nseg| = 2$), or both A- and B- or C-layer hits ($|nseg| = 3$). Table 4.1 lists the different muon types with their corresponding $nseg$ values.

nseg	Muon type	Central Track matching algorithm	MTC matching criteria
3	Central track + local muon track (A and BC layer)	Muon to central if local muon track fit converged. Central to muon otherwise	$\Delta\eta, \Delta\phi$ between MTC and central track extrapolated to calorimeter
2	Central track + BC only	central to muon	as above
1	Central track + A only	central to muon	as above
0	Central track + muon hits or central track + MTC	central to muon central to calorimeter	as above
-1	A segment only	no match	$\Delta\eta, \Delta\phi$ between MTC and A-layer segment
-2	BC segment only	no match	$\Delta\eta, \Delta\phi$ between MTC and BC-layer segment
-3	loca muon track (A + BC)	no match	$\Delta\eta, \Delta\phi$ between MTC and local muon track at A-layer if fit converged or else A-segment position

Table 4.1: Overview of the different muon types.

The second parameter for muon classification is *quality*, which can be "Loose", "Medium", and "Tight". The definitions for *quality* values are given below. The detailed information about the p17 Muon Id software and object definitions can be found in [49].

- **Tight muons**

  Only $|nseg| = 3$ muons can be Tight. A muon can be Tight if it satisfies the following:

  - at least two A layer wire hits
  - at least one A layer scintillator hit
  - at least three BC layer wire hits
  - at least one BC scintillator hit
  - a converged local fit ($\chi^2_{loc} > 0$)

- $|nseg| = 3$ **Medium/Loose muons**

If a $|nseg| = 3$ muon candidate fails the above Tight criteria, its quality can still be Medium or Loose. Such a muon is Medium if it satisfies the following:

- at least two A layer wire hits
- at least one A layer scintillator hit
- at least three BC layer wire hits
- at least one BC scintillator hit (except for central muons with fewer than four BC wire hits)

A $|nseg| = 3$ muon is Loose if it only fails in one of the above criteria, in which the A wire and scintillator requirement is treated as one test and at least one scintillator hit is required.

- $nseg = +2$ **Loose/Medium muon**

  Muon candidates with $|nseg| < 3$ can be only Medium or Loose if they are matched to central tracks. Loose quality requires:

  - at least one BC layer scintillator hit
  - at least two BC layer wire hits

  A $nseg = 2$ muon is defined as Medium if it passes the above criteria and if it is located in the bottom part of the detector (octant is 5 or 6 with $|\eta^{detector}| < 1.6$).

- $nseg = +1$ **Loose/Medium muons**

  A $nseg = 1$ muon is Loose if it has:

  - at least one scintillator hit
  - at least two A layer wire hits

  A $nseg = 1$ muon candidate is defined as Medium if it fulfills the above requirements and if it is located in the bottom part of the detector (octant is 5 or 6 with $|\eta^{detector}| < 1.6$). Low momentum muon $nseg = 1$ muons are also defined as Medium. A $nseg = 1$ muons is qualified as low momentum muon if its probability to reach the BC layer is less than 0.7.

Muons from cosmic rays are not constrained to pass through the beam position in x-y plane. A cut on the track DCA is very effective against cosmics, when a muon is a central track-matched moun. The track quality requires that DCA is less than 0.02 cm for tracks with SMT hits, and DCA is less than 0.2 cm for tracks without SMT hits. When the primary vertices are used, a cut on the z between the vertex and the muon track within 3 cm is very effective.

In di-muon events where both muons have matched central tracks, acollinearity, $\Delta\alpha$, between the two muon tracks is defined as:

$$\Delta\alpha = \pi - |\Delta\phi| + |\sum\theta - \pi|, \tag{4.8}$$

where $\Delta\phi$ and $\sum\theta$ are the angles between the two tracks. Cosmic muons pass straight through the detector and leaves two back-to-back tracks with small acollinearity. Most cosmic muons will be rejected by requiring $\Delta\alpha > 0.05$.

In the Common Analysis Format (CAF), the implementation of muon objects make analysis easier. Three types of muon objects have been defined and are stored in the muon branch: Local muon, Central track-matched muon, and Smeared MC muon. The default variables providing the best information is used, depending on the context. For example, p_T is the central track value for a track-matched muon, smeared value for a MC muon, and value from the track in muon system for a local muon. The corrections of the DATA/MC difference are done by applying three efficiencies: muon-id efficiency, tracking efficiency, and isolation efficiency. All these efficiencies are stored in the standard package provided by the Muon Id group. The trigger efficiency is modeled and is valid only for high p_T muons ($p_T > 15GeV$).

4.7 Missing Transverse Engergy

Neutrinos and other non-interacting particles travel through the detector with undetected energy. The missing transverse energy ($\not\!\!E_{\rm T}$) is defined to describe the signature of those invisible particles. At the dectector level, the calculation combines quantities from many sub-systems: calorimeter, central tracking (for PV determination), and muon detectors (for the muon correction to the event energy). At the physics level, the $\not\!\!E_{\rm T}$ needs to be calibrated with other reconstructed objects. The reconstructions of the electromagnetic objects and its scale, jets and jet energy scale, and muons, all

contribute to the corrections. Therefore, the $\not\!\!E_{\mathrm{T}}$ uses the inputs from other reconstruction algorithms and is the last reconstructed object. By vectorially summing the energy in calorimeter cells and the corrections from the muon momentum penetrating through calorimeter, the $\not\!\!E_{\mathrm{T}}$ is reconstructed. Due to the lack of detector coverage in the forward region including the beam pipe, only in the transverse plane can the momentum imbalance from invisible particles be estimated.

Chapter 5

Data and Monte Carlo Signals

In this chapter, we discuss both the data events recorded by the DØ detector and the simulated signal events. The data collection and event reconstruction processes were discussed in Section 4. After the data events are reconstructed, they are selected based on the fired triggers and detector signatures associated with each event. The simulated signal samples are produced through a series of processes. Among these processes, both the signal event generation and the corresponding detector response simulation use the Monte Carlo technique.

5.1 CAF trees and cafe framework

Both the recorded real events and the Monte Carlo signal samples are stored in the same format for further analysis. At the beginning, the thumbnail file is a compact format, which stores all the information about the event in different blocks. In each event, there is a list of the objects which are classified into different types based on their property. The objects and their information are stored in different blocks depending on the object type. The thumbnail files have an advantage that they are compact while still keeping every piece of information. However, there are also some drawbacks when doing the analysis with the thumbnail files. For instance, the content in the thumbnail file is hard to view without installing the DØ packages. Also every researcher constructs his or her own working area in different ways since there are no common regulations. This results in a waste of manpower and makes it hard to compare or transfer the analysis tools or results.

In the past several years, a new analysis framework has been designed and developed to replace

the analysis packages based on the old thumbnail files. The challenges of working with the thumbnail files are solved by this new framework, which is called "Common Analysis Format" framework (CAFe)[50]. In the CAFe framework, the rules of how to develop the analysis processors (or running executables) are regulated, which makes it easier for people other than the original developer to understand and modify the codes. Also, there are packages developed by some users and shared with all through the CVS system. This reduces the redundant work and allows analyzers to continue despite decreases in manpower.

The file style is now an object-oriented and ROOT [51] based data format, which is named "Common Analysis Format" (CAF) [52]. The basic storage mechanism uses the TTree in ROOT. It contains the global information, reconstructed objects, trigger information, object identification information, and detector data, e.g. Calorimeter cells. The Monte Carlo information is also included for the Monte Carlo events. There are two types of objects. One inherits from the "TMBLorentzVector" and contains a four-dimension vector. And the other inherits from "TObject". It is much easier to view the object-oriented tree structure and the stored information in the ROOT environment.

Both the CAF structure and the CAFe packages are under development all the time. Old bugs are fixed and new features are implemented in different versions. It is important to decide which version should be used for one's data analysis. For our analysis purpose, we follow the instructions on the CAFe webpage [53].

5.2 Data collected at DØ

The data events used for this analysis were collected with the DØ detector at the Fermilab Tevatron $p\bar{p}$ collider at $\sqrt{s} = 1.96$ TeV between July 2002 and February 2006. The data sample used for this analysis is the p17 "MUinclusive" data skim produced by the Common Samples Group[54]. The term "p17" means that all the data events are collected and reconstructed by the DØ packages in the p17 version release. The "MUinclusive" means that in every event there is at least one reconstructed muon object satisfying certain requirements. The skimmed data set consists of both the skimmed refixed data and the reskimmed unfixed data. The latter includes both the non-cable-swap and cable-swap data. The "refixed" stands for the bugs existing in the earlier package version so that those events had to be reprocessed; the "unfixed" means that the events are processed with the packages

which have inherited the bug fixing code from the earlier version. For the "unfixed" data events, there was a period when some cables in the calorimeter detector were switched. In order to fix this, the events were processed with a different package version, which is different from those data collected after the cables were switched back. The complete skimmed data set therefore includes three predefined data sets (thumbnails) which consist of

1. CSskim-MUinclusive-PASS3-p17.09.03 (refixed),
2. CSskim-MUinclusive-PASS3-p17.09.06 (unfixed, cable-swap),
3. CSskim-MUinclusive-PASS3-p17.09.06b (unfixed, non-cable-swap).

Every event in this data sample was recorded because it fired at least one trigger, which is designed to select good events for further physics analysis. The triggering system at DØ has been introduced in Section 3.2.7. The trigger list, which is a combination of triggers, is designed and used on the on-line data taking process. The combinations and the component triggers are varied and adjusted in order to keep data taking rate acceptable with the increasing luminosity at the Fermilab Tevatron. Thus, the trigger list has different versions, according to the highest instant luminosity delivered at DØ in different time periods, and is labeled with ascending numbers. The data samples were taken mainly with trigger list version v14 and v15.

During the data collection, there is a chance that some detector system(s) or parts of them malfunction. For example, there could be hot cells in the Calorimeter, or a high voltage power supply failure in the Muon system. In those conditions, the recorded data event would be affected, and the physics objects, especially those based on the faulty measurement readouts, would be reconstructed with wrong properties. Such runs are called "bad runs" and the data events in those runs should not be labeled as "good quality events". Sometimes, the problems could be fixed by the operation shifters and experts in a short time; then only part of the events are recorded with bad quality. In this case, the luminosity blocks, corresponding to those time slots, should be excluded from the further physics analysis. During the normal data taking process, all the events passing at least one trigger selection are recorded on our tapes, no matter whether there is any detector system that malfunctions. Those events are also reconstructed with the same software as the good events. In order to keep the high quality of the data sample, bad runs (for CALORIMETER, CFT, MUON and SMT) and bad luminosity blocks were removed during the CAFe process for further physics analysis.

Since in this analysis we study only the direct pair production of the interesting signals, each event is required to have exactly two good quality muons. Di-muon triggers in DØ trigger lists are designed to select those events which have two good muons. Each trigger consists of different requirements at the three trigger levels, which are detailed in the following. The events passing the di-muon trigger, are required to fire two separate scintillator triggers at L1. Each of these L1 scintillator triggers must have scintillator hits in more than one layer, which will be used in the calculation of particle speed. At L2, a "MEDIUM" quality muon is required for all the dimuon triggers used. As mentioned above during the data taking period, the triggers and trigger lists were often changed, which is reflected in different L3 conditions being used for each trigger in different trigger lists. It is possible for the triggers to share the same name while requiring various L3 criteria. The full Run IIa sample can be divided into separate periods, where the “Run IIa” means the data taken before the Layer-0 detector was installed between the beampipe and the central SMT. The whole Run IIa di-muon samples are summarized in Table 5.1, which lists the dimuon trigger used from each trigger list version in each period and its corresponding integrated luminosity. The integrated luminosity for the di-muon trigger events is calculated by using the "getLuminosity" program [55]. The total luminosity is $1.1\,\text{fb}^{-1}$ for the data sample analyzed in this study.

Run Start	*Run Stop*	*Version*	*Trigger*	*Luminosity* $\left(pb^{-1}\right)$
160582	*167015*	*v8*	*2MU_A_L2M0*	*5.91323*
167019	*170246*	*v9*	*2MU_A_L2M0*	*39.4677*
170247	*174802*	*v10*	*2MU_A_L2M0*	*17.3911*
174896	*178721*	*v11*	*2MU_A_L2M0_TRK10*	*69.9599*
178722	*180956*	*v12a*	*2MU_A_L2M0_TRK5*	*47.3961*
184951	*190370*	*v12b*	*2MU_A_L2M0_TRK5*	*88.5615*
191266	*194597*	*v12c*	*2MU_A_L2M0_TRK5*	*105.848*
194567	*196584*	*v13a*	*DMU1_LM6*	*59.1665*
201485	*201936*	*v13b*	*DMU1_LM6*	*4.61323*
202152	*204805*	*v13c*	*DMU1_TK8*	*127.539*
204807	*206161*	*v13d*	*DMU1_TK8*	*82.1435*
206162	*208144*	*v13e*	*DMU1_TK8*	*110.448*
207728	*211213*	*v14a*	*DMU1_LM6_TK12*	*172.449*
211214	*212107*	*v14b*	*DMU1_LM6_TK12*	*69.635*
212804	*215670*	*v14c*	*DMU1_LM6_TK12*	*90.0956*
				1090.627

Table 5.1: *Integrated luminosity by trigger list*

The data events in the p17 data skims are saved as "CAF-trees" [50]. However, the timing information of the hits in scintillation counters of the muon system is unavailable in these CAF-trees. Other information about each hit associated with the muon particle is also unavailable. Therefore, we developed our own customized version of the CAF-tree maker to produce the CAF-trees in order to access all the information of each single hit found in the muon system no matter which hit type it is. Under the instructions from the Common Sample Group, the DØ product release version "p18.09.00" is used as the base release, where the modifications are added in order to compile our own local built executables for format conversion. New variables and functions related to the hits associated with each muon are added in the "TMBMuon" class, which is designed to access the muon information. The standard container one-dimensional arrays are used to store the information, and the standard vectors are used to access the hit information. All the codes follow the programming rules in C++ [56, 57] and ROOT [51].

We reskimmed the whole "MUinclusive" data skim not only the "2MUhighpt" skim, because we wanted it to be possible to conduct any further studies and corrections with single or multiple muon events. Since the full "MUinclusive" skim contains too many events which do not qualify as high transverse momentum events, we imposed an additional requirement (muon $p_T \geq 15$GeV) to select potentially useful events. By doing this, our working load for this format convertion is reduced by two thirds, as is the output data size, which is now more manageable.

5.2.1 Run-to-run corrections on clock shift

The master clock of the DØ experiment, which is used to synchronize the experiment to the time structure of the accelerator, has been studied carefully and shown to have a drift of a few nanoseconds on a seasonal basis. This drift is reflected in Fig. 5.1, which plots the mean of the muon timing distribution versus the run number for the forward A-layer scintillation counters. The mean is determined in two ways. When there are enough statistics (> 10 scintillator hits) for one run, a Gaussian fit will be applied to the histogram and the mean of the fit (μ) is the mean of the timing distribution of that run. However, when there are 10 or fewer scintillator hits in a run, the mean is the average value of the timing. A run-to-run correction factor is obtained from the mean of the timing distribution for each run. By observing the distributions of the mean value for each run, we noticed that the shift becomes smaller and flatter for later events with larger run numbers. This

is because the master clock is re-adjusted four times per year in order to reduce the seasonal drift basis.

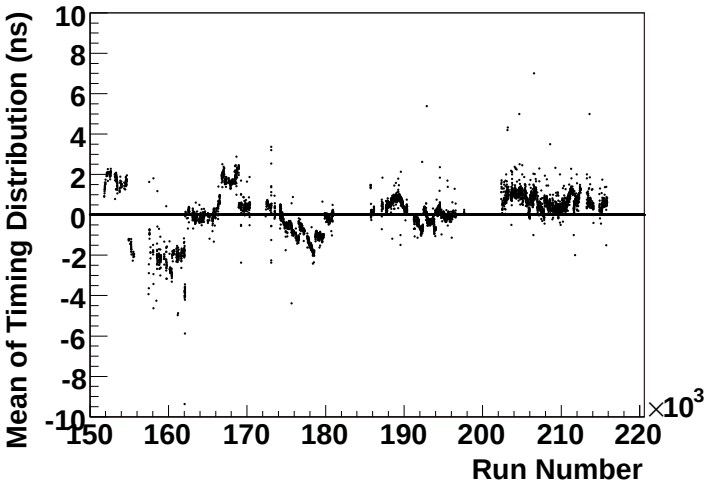

Figure 5.1: Mean timing value for the forward A-layer scintillation counters, for each run in the complete data set.

There are some runs with large timing shifts, especially in the data taken in early Run II time. The large shifts come from those runs with small statistics (around 10 hits per run) in pacific scintillation counter planes. The accuracy has been improved for runs with later run numbers due to the increased instantaneous luminosity. For further analysis with even high luminosity, the minimal number to use Gaussian fit can be increased for higher accuracy.

The timing distributions for each run in the Run IIa period are derived from the tight muons in the selected $W \rightarrow \mu\nu$ events. W samples are used because the cross section for W events is about an order of magnitude higher than the $Z \rightarrow \mu\mu$ events. In other words, the statistical uncertainty is much smaller in W samples than in Z samples. The reskimming of MUinclusive skim instead of the 2MUhighpt skim makes this study possible. The selection criteria for choosing $W \rightarrow \mu\nu$ events are the following:

- There must be one but only one good muon in the event. The "good" muon should have quality "medium" or "tight" (according to the MuonID requirement) with scintillator hits in

both A- and B-/C-layer [48] and have a matched track in the central tracking system. The matched track should have $p_T \geq 20$ GeV.

- The muon should satisfy the isolation requirements both in the calorimeter and in the central track.
  - $\sum_{cone0.5}(p_T) < 2.5$ GeV, where $\sum_{cone0.5}(p_T)$ is the sum of p_T of tracks contained within a cone around the muon direction with distance $\Delta R < 0.5$.
  - $\sum_{halo}(E_T) = \sum_{cone0.4}(E_T) - \sum_{cone0.1}(E_T) < 2.5$ GeV, where $\sum_{cone0.1}(E_T)$ and $\sum_{cone0.4}(E_T)$ are sums of the E_T of calorimeter clusters in cones around the muons with distance $\Delta R < 0.1$ and $\Delta R < 0.4$, respectively. Only cells in the EM (electromagnetic) and FH (fine hadronic) calorimeters are taken into account, while those in the CH (coarse hadronic) calorimeter are not considered.
- The MET (missing transverse energy) of the event should be corrected with the matched central track and should be larger than or equal to 20 GeV.

There are in total eight plots drawn for all the scintillator counter planes in the muon system because there are several different types of scintillation counters used in the DØ muon system. Those counters are divided into eight different groups based on their types and their geometry locations. The groups are the forward pixel planes in the A-, B-, and C-layer, the central A-layer, central side B-layer, central top/side C-layer, central bottom B-layer, and central bottom C-layer. Therefore there are also eight separate corrections to those individual scintillation counter planes.

The timing in the DØ muon system is adjusted so that a particle traveling at the speed of light will register a time of zero at the scintillators. This is accomplished by subtracting a value, known as T0, in the front-end electronics. Corrections have been applied for those runs during the early Run II data-taking period when the T0s had not been properly calculated.

The timing resolution of the muon scintillators was determined from a sample of data collected during DØ Run IIa period and selected for $Z \rightarrow \mu\mu$ events. The events must have two muons with medium quality. As mentioned above, the timing corrections are done in eight groups, the time resolutions for those counters are also obtained individually in each corresponding group. The registered scintillator hit times associated with the muons are plotted in eight histograms separately.

The Gaussian fit is applied to each histogram; the σ of the Gaussian fit is taken as the timing resolution of that scintillator counter plane.

The seasonal timing drifts of the DØ master clock have visible effects on the registered timing in the muon system. Applying those run-to-run corrections based on the detector's geometry information leads to a slight improvement in the time resolution of the muon scintillators, which is summarized in Table 5.2.

Scintillation counter	*Resolution before correction (ns)*	*Resolution after correction (ns)*
Forward A-layer	*2.3*	*2.2*
Forward B-layer	*2.4*	*2.3*
Forward C-layer	*2.5*	*2.4*
Central A-layer	*2.4*	*2.1*
Side B-layer	*2.5*	*2.5*
Bottom B-layer	*3.3*	*3.5*
Side C-layer	*4.0*	*3.8*
Bottom C-layer	*3.6*	*3.3*

Table 5.2: *Scintillation time resolutions before and after run-by-run corrections.*

The mean of the Gaussian fit is the offset of the scintillator counters. It is possible that the value of the mean is non-zero, since the timing distributions may not be centered exactly at zero. This demonstrates that it is necessary to apply the run-to-run timing corrections when deriving the time resolutions. Similar effects are expected on the offset values, which are adjusted to be more close to zero by applying these corrections. The resolutions and offsets obtained from the real data are shown in Table 5.3.

Scintillation Counter	*resolution (ns)*	*offset (ns)*
Forward A-layer	*2.2*	*-0.06*
Forward B-layer	*2.3*	*-0.20*
Forward C-layer	*2.4*	*-0.34*
Central A-layer	*2.1*	*-0.12*
Side B-layer	*2.5*	*0.12*
Bottom B-layer	*3.5*	*-0.45*
Side C-layer	*3.8*	*-0.35*
Bottom C-layer	*3.3*	*0.25*

Table 5.3: *Measured scintillation counter resolutions and offsets.*

Each region of the muon system consists of three separate layers, referred to as the A-, B- and C-layers. The A-layer is closest to the interaction region and is inside a 1.8 T iron toroid. The B- and C-layers are outside the toroid. Each layer consists of drift tubes, used in muon tracking, and scintillator counters, used for triggering. Each scintillation counter registers the time and the position of a passing muon. This time and position information can be used to measure the speed of the muon. The read-out gates are applied at L1 in the muon system. The read-out gates are set that the light-speed muons arrive at zero ns and are asymmetric around zero ns. The gate width is 120 ns from -40 ns to 80 ns. The asymmetric structure of the read-out gates allows the particles moving at low speed to be recorded, which is important for our analysis. Meanwhile, there are electronic devices in each scintillation plane, which set the restriction on the registered timing. This timing restriction is the L1 Muon trigger gate, whose values are shown in Table 5.4.

Section	*Trigger Gate (ns)*
Central A-layer	*24*
Central side B-layer	*84*
Central bottom B-layer	*50*
Central side C-layer	*46*
Central bottom C-layer	*60*
All forward layers	*30*

Table 5.4: *Muon System Trigger Gates.*

5.3 Signal Samples

The signal samples are generated through a sequence of processes, involving the Monte Carlo method. First, the events are produced with a generator using the MC method. In this stage, PYTHIA 6.323 [58] was used to generate pair-produced stable CMSPs. Samples were generated for three different models, where the NLSP is either a stable stau, or a stable higgsino-like chargino, or a stable gaugino-like chargino in the model. The details are discussed in Sections 2.32.4. In every model, seven typical mass points were chosen: 60, 80, 100, 150, 200, 250, and 300 GeV. 50,000 events were generated for each model and mass point.

The second stage is to simulate the responses of the DØ detector to each particle/object in the generated event. The DØ full detector GEANT simulation (D0GSTAR) [59] is employed to simulate

the detector response for Monte Carlo (MC) samples. The default GEANT3 in D0GSTAR would treat the CMSPs in our model as unknown particles which only contribute to the missing transverse energy (MET). Since the CMSPs in our models should be weakly interacting charged particles, the detector signature of such particles would be very striking. The CMSPs should first leave traces in the central tracking system, penetrate through the calorimeter as minimal ionization particles (MIPs), and register in the out-most muon detector. In short, the CMSPs would be recognized as the heavy muons based on the detector signals. The modifications have been added so that the CMSPs can propagate through the detector and register in the muon system; we expect them to appearing as heavy muon-like particles. The energy deposited in the central tracking system will be simulated depending on the particle mass and kinematics at the generator level, as well as the registered timing in the muon system. Basically, this modification can be used for any weakly interacting muon-like particles, but not for those with strong interactions, e.g. stop quarks.

The output from D0GSTAR is processed with another DØ package "d0sim". In this stage, all the analog signals from the D0GSTAR are converted to digitized signals. Afterwards, the events are further processed with the reconstruction package "d0reco", which is the same for the recorded real data events.

Finally, all the reconstructed events are converted from the thumbnail files to our customized CAF trees, where the muon hit information is stored.

5.3.1 Muon System Geometry

As mentioned above, D0GSTAR is developed based on the GEANT code and adjusted to describe the response simulation of the DØ full detector. The adjustment to DØ is done by providing the files which contain the detector information, both for the full geometry and for the materials. For example, the silicon trackers in the SMT system are listed with their plane position in three dimensional coordinate system and the properties of the materials in the tracker, e.g. the thickness of the silicon layer.

For our research, the description of the muon system is the most important component of this muon-based analysis. The muon detector geometry information is in the default setting of D0GSTAR. It can provide the position information of the scintillation counters. The 3D coordinates (x, y, z) are also provided for each scintillator hit associated with each muon particle.

Figures 5.2 to 5.5 show the hit distance distributions in both central and forward A-, B-, and C-layer for $Z \rightarrow \mu\mu$ events in real data and MC samples. The distance was calculated from the origin of the DØ coordinate system, which is the center of the detector, to the hit position recorded in the muon system. The $Z \rightarrow \mu\mu$ events were selected using the selection criteria listed in Section 6.2 with the invariant mass of the pair of muons in the events between 70 and 110 GeV.

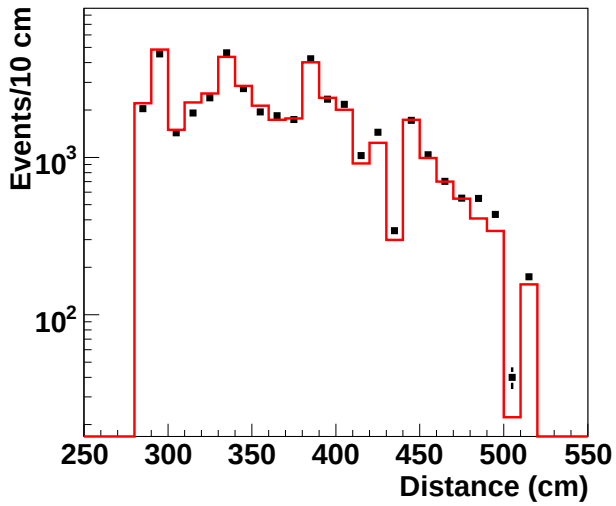

Figure 5.2: Comparison of the calculated distance from the center of the detector to the central A-layer muon region, for Z$\mu\mu$ events in real data (black points with errors) and MC samples (red line). The histograms in the plots are normalized to have the same number of events.

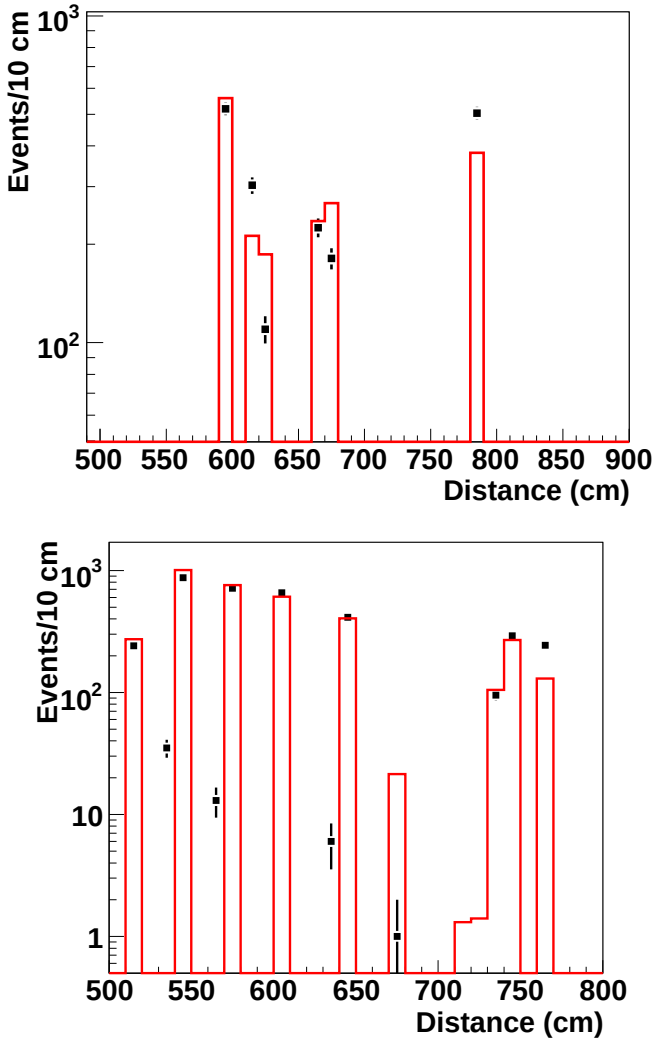

Figure 5.3: Comparison of the calculated distance from the center of the detector to the central B-layer muon region, for Z$\mu\mu$ events in real data (black points with errors) and MC samples (red line), for side region (top) and bottom region (bottom) scintillation counters. The histograms in the plots are normalized to have the same number of events.

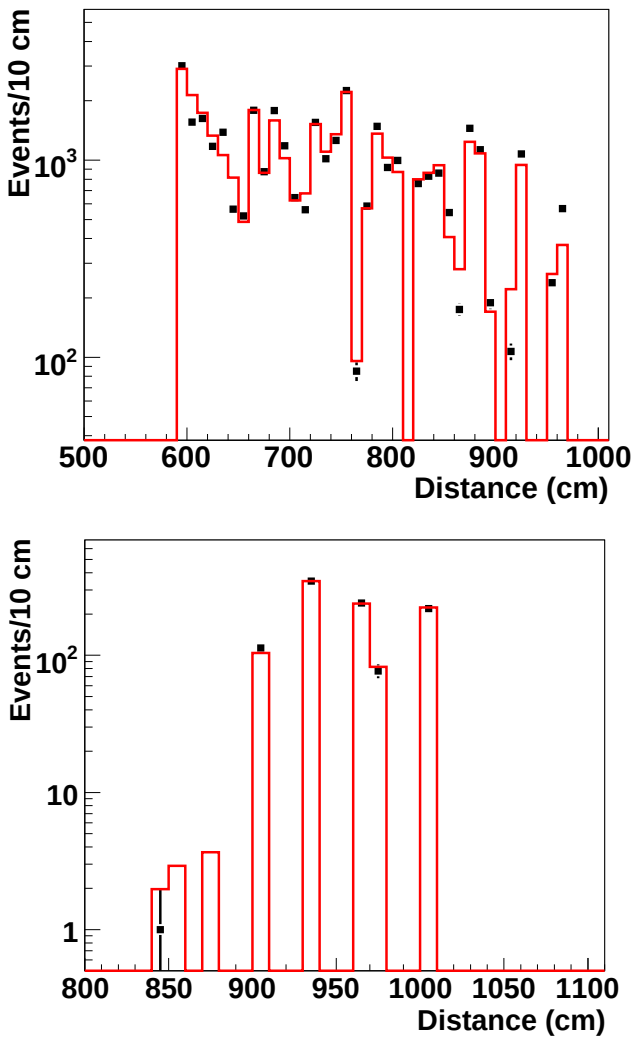

Figure 5.4: Comparison of the calculated distance from the center of the detector to the central C-layer muon region, for Z$\mu\mu$ events in real data (black points with errors) and MC samples (red line) for side/top region (top) and bottom region (bottom) scintillation counters. The histograms in the plots are normalized to have the same number of events.

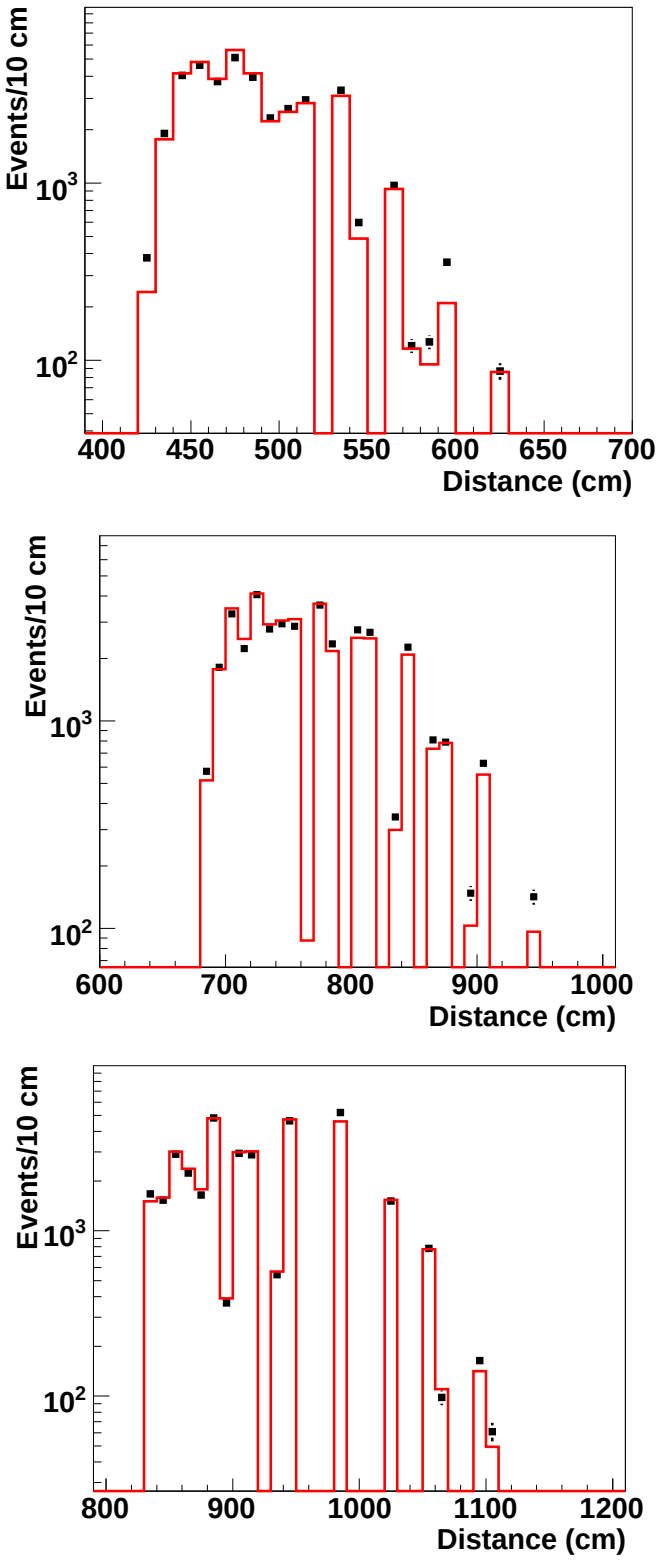

Figure 5.5: Comparison of the calculated distance from the center of the detector to the forward muon region, for Z$\mu\mu$ events in real data (black points with error) and MC samples (red line), for A-layer (top), B-layer (middle) and C-layer (bottom) scintillation counters. The histograms in the plots are normalized to have the same number of events.

Generally there is a good agreement of the calculated distance between the real data and the MC. However, there is still some discrepancy between the real data and the MC samples for some counters, especially the bottom region in the central B-layer. This can also be observed in Figs 5.2 to 5.5. After all from the above distributions, it can be concluded that the MC distance distributions compare well with the real data.

As a short summary, the D0GSTAR does an excellent job of providing geometry information for both the scintillation counters and the hits registered in the muon system.

5.3.2 Muon Timing Smearing

After the confirmation of the detector geometry information, the following step was undertaken to ensure that the time-of-flight implementation in the Monte Carlo simulation is accurate.

We calculate the time-of-flight for simulated CMSPs to reach a given muon scintillation counter by the combination of the known speed of the particle (based on the generator-level Monte Carlo information) and the distance of the muon scintillation counter from the collision point. As mentioned above, the readout time in the DØ muon system recorded in the real data is adjusted so that a particle traveling at the speed of light will register a time of zero at the scintillation counters. In order to accurately model the readout of the registered timing of a particle reaching a muon scintillator, it is necessary to subtract this T0 from the MC simulated time. Since signal carrying cable lengths vary for different scintillation counters, the actual T0s used by the front-ends cannot be used. So, each scintillator's T0 used for the MC is taken as the time for a particle traveling at the speed of light from the center of the DØ detector to reach the center of the scintillation counter.

The readout time of a particle's hit in a scintillation counter is simulated in the following steps:

1. Determine the vertex position which is the production point of the particle.

2. Calculate the distance (d) between the production point and the hit position in the scintillation counter.

3. Calculate the travel time of the particle t_0 from the travle distance divided by the generator level speed.

4. Calculate the travel time of a light-speed particle (T0) from the center of the DØ detector to the scintillation counter.

5. Derive the difference, $t' = t_0 - \mathrm{T0}$, between the particle travel time and T0.

6. The final readout time is the sum of the t' and a random number from the smearing timing distribution for that scintillation counter, i.e. $t = t' + rnd$.

As discussed above, the final step in deriving the scintillation counter times in a simulated event is to apply smearing that reflects the observed measurement uncertainty in the hit times. Figures 5.6 through 5.9 show the timing distributions in different regions for A-, B- and C-layer scintillation counters for $Z \rightarrow \mu\mu$ events, comparing real data with MC samples. In the plots, the run-to-run timing corrections have been applied to the data events, and the estimated T0s have been subtracted for the MC events. The smearings on the positive time have more entries thatn the negative tside because the timing gates are asymmetric and are wider in positive side to allow slow moving particles.

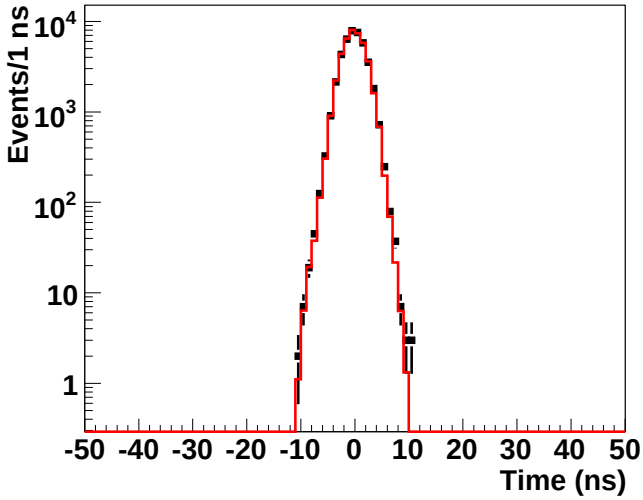

Figure 5.6: Timing smearing comparison plot in central A-layer muon region for Z$\mu\mu$ events in real data (black points with errors) and MC samples (red line). The histograms in the plots are normalized to have the same number of events.

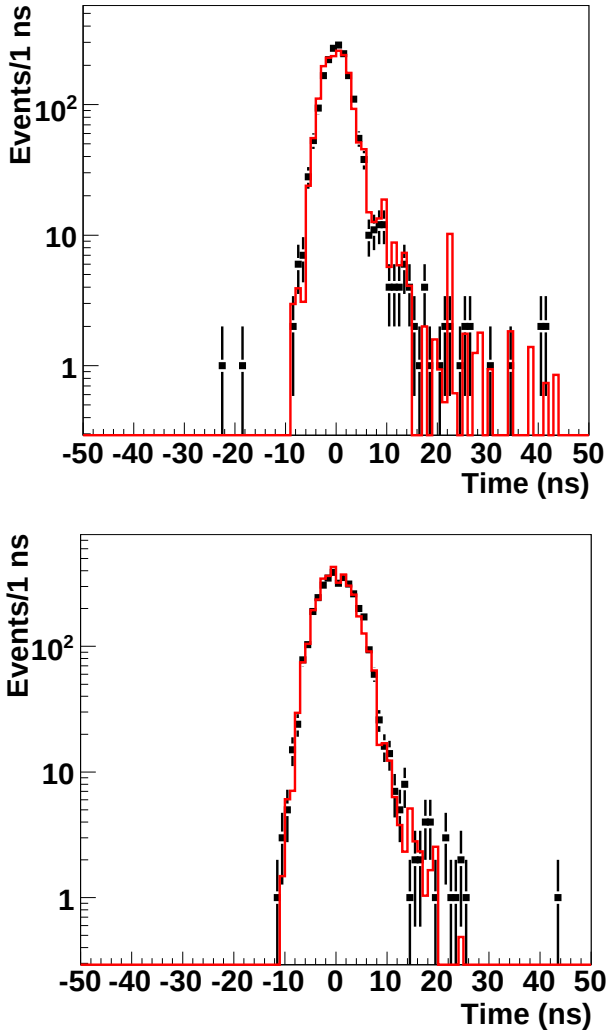

Figure 5.7: Timing smearing comparison plot in central B-layer muon region for Z$\mu\mu$ events in real data (black points with errors) and MC samples (red line) for side region (top) and bottom region (bottom) scintillation counters. The histograms in the plots are normalized to have the same number of events.

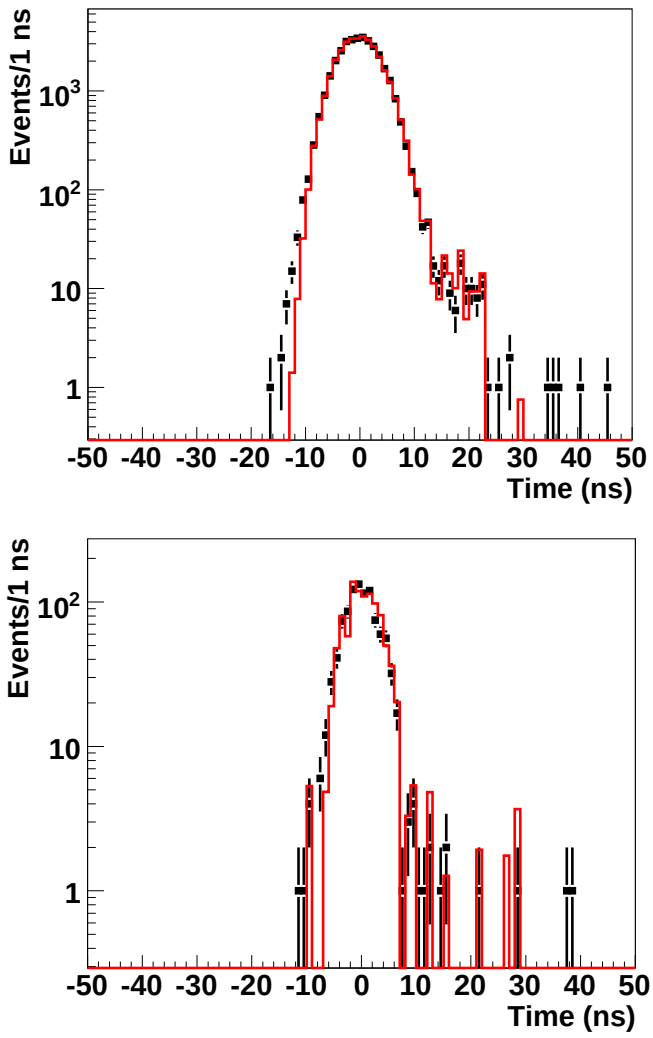

Figure 5.8: Timing smearing comparison plot in central C-layer muon region for Z$\mu\mu$ events in real data (black points with errors) and MC samples (red line) for side/top region (top) and bottom region (bottom) scintillation counters. The histograms in the plots are normalized to have the same number of events.

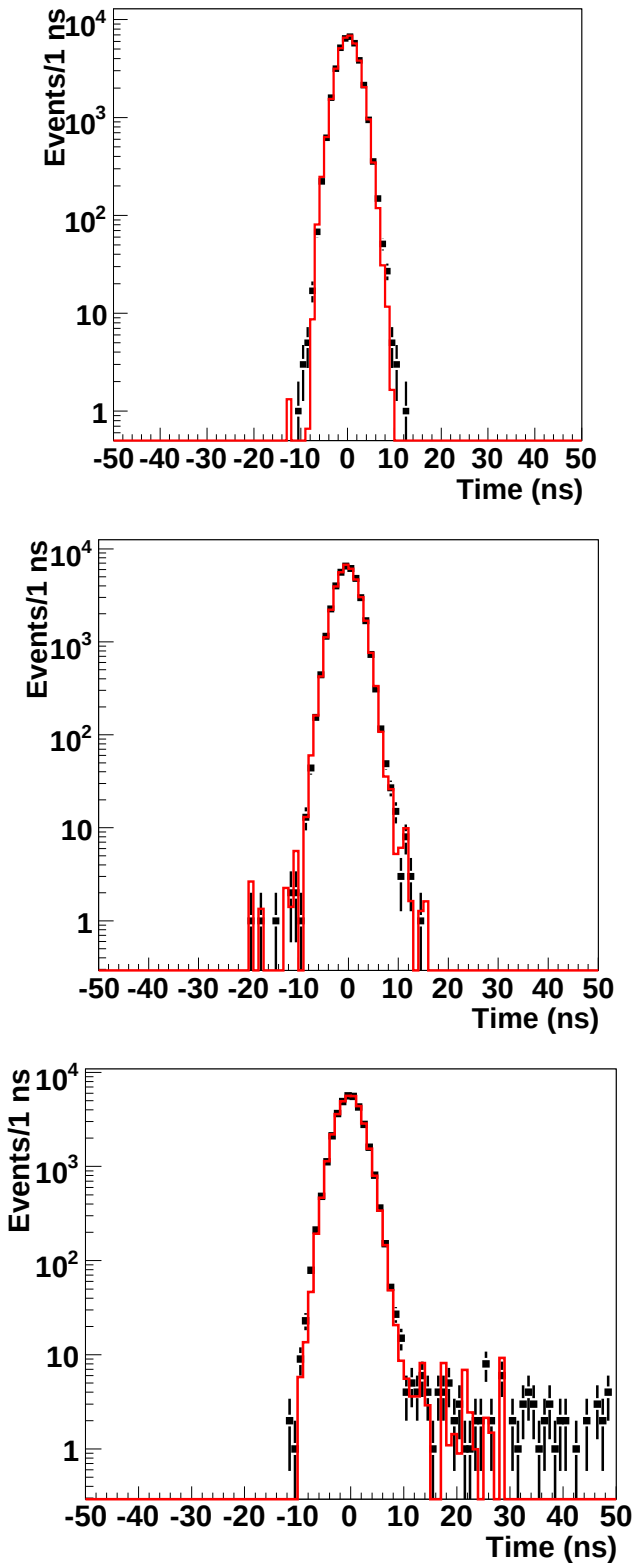

Figure 5.9: Timing smearing comparison plots in forward muon region for Z$\mu\mu$ events in real data (black points with errors) and MC samples (red line) for A-layer (top), B-layer (middle) and C-layer (bottom) scintillation counters. The histograms in the plots are normalized to have the same number of events.

There is a discrepancy between the data and smeared MC times as seen in Fig. 5.8, which is $O(10^{-3})$ of the peak and on the negative side. One contribution to this discrepancy is the statistics of the MC events is a factor of 3 below the recorded real data. This discrepancy between data and MC in the C top/side region time smearing is treated as a systematic uncertainty in the final results. As shown in Section 6.5.2, the simulated MC timing distributions from using $W \rightarrow \mu\nu$ samples have higher tails but lower peaks. We study the systematic uncertainty by using the timing smearing from the $W \rightarrow \mu\nu$ samples.

This smearing has been implemented in the CAFe framework as an additional processor only for the Monte Carlo samples. The data and MC distributions generally agree well, indicate the suitability of the Monte Carlo simulations for the DØ detector responses.

5.3.3 Muon Trigger Timing Gate Effects

Since only direct pair-production of the CMSPs particles are considered, one selection criteria should be applied in order to classify events with two good muons. Di-muon triggers require that there must be two muons in the events satisfying all the criteria at three trigger levels. The L1 muon trigger gate, as the first requirement in di-muon triggers, requires that the A-layer hit must be within the trigger gate, while either the B- or C-layer hit should be within the trigger gate. When the particles have both B- and C-layer scintillation counter hits, the trigger will be fired if one of the hits is within the trigger gate even if the other one is outside with a large registering time in the muon system. One thing to remember is that the two muons firing the di-muon triggers do necessarily have to be the good quality muons selected for further analysis.

The trigger gates are adjusted so that muons produced in $p\overline{p}$ collisions, traveling at the speed of light, will arrive in the center of the trigger gate. The gates help to reduce the cosmic ray contamination. However, due to the limited gate lengths shown in Table 5.4, the particles arriving outside the trigger gate will be rejected, so that that particle cannot fire the L1 muon trigger.

This analysis uses triggers based on hits in the muon scintillation counters. The effects of the muon trigger timing gate on the signal efficiency should be studied and understood. If the CMSP is moving too slowly due to its heavy mass, it will arrive at the scintillation counter outside of

the trigger gate. This inefficiency increases when the mass of the CMSPs increases. The trigger efficiency is defined as the number of events firing the trigger divided by the total number of the events generated. Since a large portion of the CMSPs would move at a speed substantially smaller than the speed of light, they will have a larger chance to be outside the timing gates. Also, the heavier the masses of the signal particles, the higher possibility they have to be outside the gates than muons. The expected trigger efficiency drops with the increasing mass of the signal particles can be observed in Fig. 5.10.

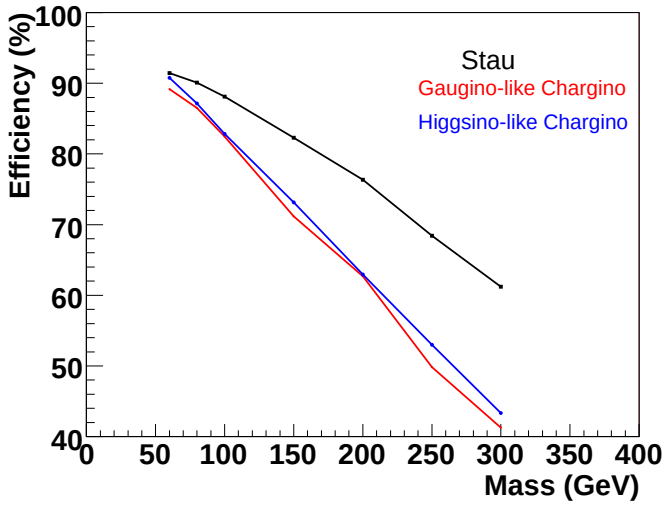

Figure 5.10: The percentage of signal events within the L1 muon trigger for stau (black), gaugino-like chargino (red) and higgsino-like chargino (blue).

5.3.4 Muon p_T Smearing

The p_T resolution of the reconstructed muons in Monte Carlo is found not to match accurately with the one measured in real data events. Further smearing on p_T is required in Monte Carlo. This is done in [48] with $Z \rightarrow \mu\mu$ events. The smearing parameters are determined for a smearing of either the form:

$$\frac{q}{p_t} \rightarrow \frac{q}{p_t} + (A + B_1/p_T) \times Rnd$$

	run < 2×10^5		run > 2×10^5	
	A	B_1	A	B_1
SMT hits ($\|\eta_{CFT}\| < 1.6$)	0.00313	-0.0563	0.00308	-0.0370
SMT hits ($\|\eta_{CFT}\| > 1.6$)	0.00273	-0.0491	0.00458	-0.0550
no SMT hits	0.0509	-0.0916	0.00424	-0.0509

Table 5.5: Default smearing parameters for the parametrization $A + B_1/p_T$.

or:

$$\frac{q}{p_t} \rightarrow \frac{q}{p_t} + (A + B_2 \times p_T) \times Rnd$$

where Rnd is a Gaussian distribution random number with a width of 1 and centered at 0. The fit is performed in two stages. The complete sample is used to determine the smearing at $p_T = 40\,GeV$, which corresponds to the average muon p_T in the sample. By fitting $A_0 = A + B_1/40\,GeV$ or $A_0 = A + B_2 \times 40\,GeV$ while fixing the ratio $R = B/A$, the smearing parameters are derived. The ratio $R = B/A$ is determined by using samples where either both muons have $p_T > 40\,GeV$ or both have $p_T < 40\,GeV$. The resolution is separately determined for three types of muons:

- Muons with SMT hits and $|\eta_{CFT}| < 1.6$
- Muons with SMT hits and $|\eta_{CFT}| > 1.6$
- Muons without SMT hits

η_{CFT} is the detector η in the CFT-detector and a measurement for the number of possible CFT-hits a track could have. Tracks cannot pass through all CFT layers when $|\eta_{CFT}| > 1.6$. The parameters are determined by requiring the fit of the Drell-Yan spectrum returning the same width in data and the smeared MC simultaneously in three samples. The resolutions dramatically changed in data taken in runs before and after the fall shutdown in 2004 with run number < 2×10^5. Therefore, the smearing parameters and resolutions are determined separately for the two data periods, as shown in Table 5.5.

In addition to the width of the Z^0 peak, the fit also returns the peak position. The different momentum scale in the data and the Monte Carlo, is the difference in the position between the data and MC, which is used to correct the MC momenta as an additional scaling factor. The results for

the comparison yield a scaling factor for muon p_T of $S = 0.9995 \pm 0.0010$ and $S = 0.9990 \pm 0.0012$ for pre- and post-shutdown data, where $1/p_T$ has to be scaled by $1/S$. The errors result from the variation of the p_T dependence on the smearing and the statistical uncertainty of the peak position in the data. The latter contributes 0.0006 to the error. The factors are consistent with 1, therefore, no scaling is implemented in the standard smearing.

The above smearing is determined using only $Z \rightarrow \mu\mu$ events. However, this set of smearing parameters strongly depends on the p_T of the muon. Also the multiple scattering term (B) are correlated with the resolution term (A). Further studies have been carried on both $Z \rightarrow \mu\mu$ and $J/\psi \rightarrow \mu\mu$ events [60]. The new smearing formula is now modified to be

$$\frac{q}{p_T} \rightarrow \frac{q}{p_T} + AG_1 + \frac{B\sqrt{\cosh\eta}}{p_T}G_2 \tag{5.1}$$

where G_1 and G_2 are two independent random numbers distributed according to a Gaussian function with a mean value of 0 and a width of 1. The additional resolution from the formula is

$$\frac{\sigma(1/p_T)}{p_T} = \sqrt{A^2 p_T^2 + B^2 \cosh\eta} \tag{5.2}$$

Detailed studies have been done in [60] and show a good agreement between data and smeared Monte Carlo events for both $Z \rightarrow \mu\mu$ and $J/\psi \rightarrow \mu\mu$ events.

5.3.5 Scintillation Counter Efficiency Maps

Due to the detector geometry, the coverage of the scintillation counters is not 100% and the efficiency is not perfect. An efficiency map is designed to measure the efficiency of the scintillation counters in the muon detector. In previous DØ CMSP analysis [28], a Parameterized Monte Carlo Simulation (PMCS) was used to simulate the detector and the response. The PMCS integrated those efficiency maps for the scintillation counters because there was no detector description at all. During the transfering to the full MC in this analysis, we generated new scintillation efficiency maps as one check on our simulaiton.

There are eighteen maps generated based on the detector geometry. In the forward muon detector region, three maps are produced for the south pixel planes in each layer, and three are done for

the north pixel planes. In the central muon detector region, four maps (top, bottom, east and west) are derived for each layer. These maps were obtained using "Tag and Probe" method [61] on a sample consisting of the muons matched with the central track in the entire data and the $Z \rightarrow \mu\mu$ MC samples separately. Each scintillation counter plane was divided into 10 cm $\times$ 10 cm bins. The tag is a track-matched muon with medium quality and the probe is a track-matched muon. The isolated central track was extrapolated to the plane combined with the interaction point information. Then it was determined whether there is a muon with a scintillator hit in that plane. The efficiency of each bin was determined as the number of muons with scintillator hits in that bin divided by the total number of muons in that bin.

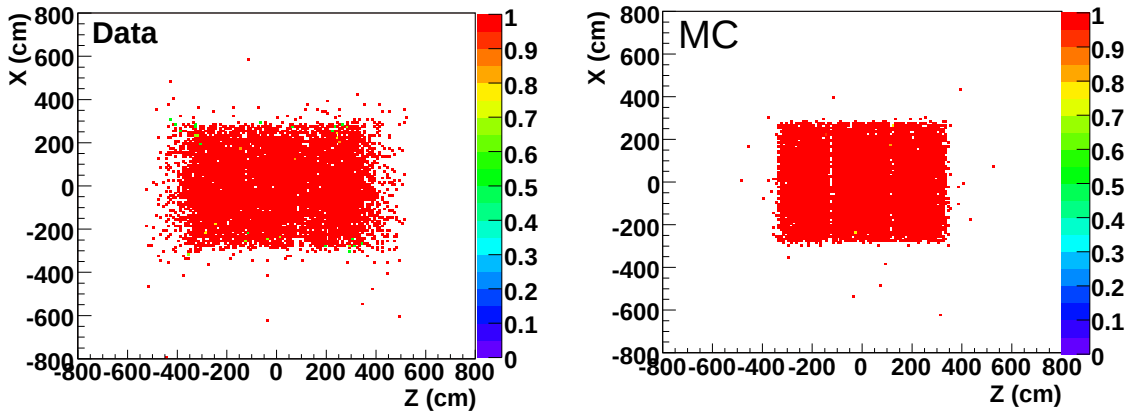

Figure 5.11: Efficiency maps for scintillation counter plane in central A-layer top region.

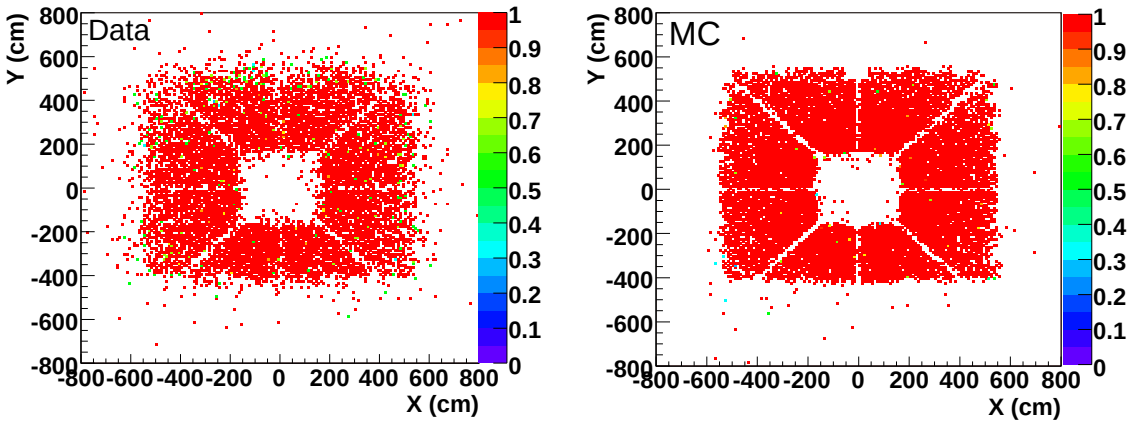

Figure 5.12: Efficiency maps for scintillation counter plane in forward B-layer south region.

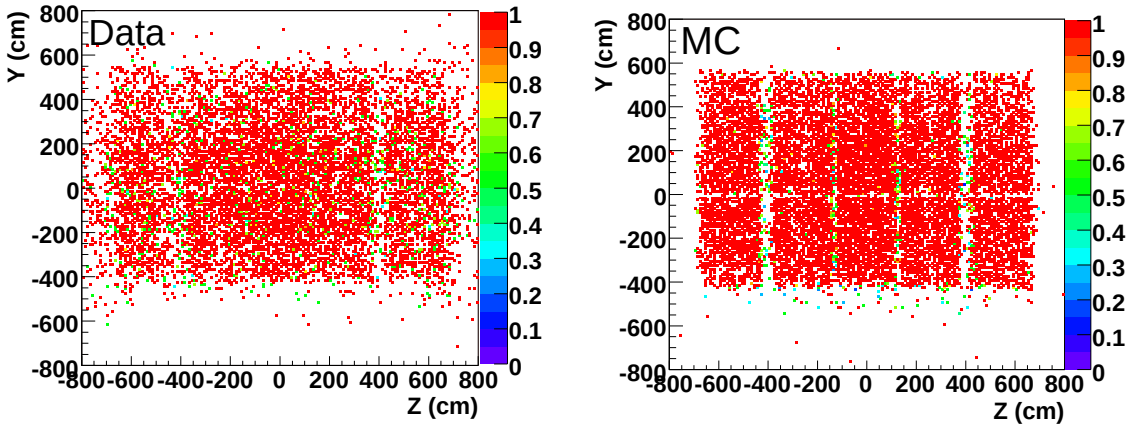

Figure 5.13: Efficiency maps for scintillation counter plane in central C-layer east region.

Figures 5.11, 5.12, and 5.13 show the comparison of the efficiency maps between the real data (top) and MC (bottom) for central A-layer east region, forward B-layer south region and central C-layer east region, respectively. The maps show an agreement between the data and Monte Carlo. Since the efficiency was calculated based on the extrapolated hit position from the central track, the edges may not be as clear as the real counter boundaries. In MC, only $Z \rightarrow \mu\mu$ events were investigated. For the real data, we selected events with one tight muon and the other muon from all possible processes for large statistics. As mentioned above, this study provided a good comparison of the full simulation with the PMCS, but was not used to derived the data/MC scale factors for full simulation.

5.3.6 Data/MC Scale Factors of the Scintillation Counter Efficiency

As mentioned in previous section 5.3.5, the data/MC scale factors for the full simulation are not derived from the scintillation counter efficiency maps. The muon identification quality has included certain requirements on the scintillator hits as listed in section 4.6. To avoid applying the efficiency scale factor twice, we integrated the scintillator hit requirements to the official muon identification quality.

During smearing the Monte Carlo samples, the data/MC scale factor is needed to correct the

muon identification (MuonID). This scale factor is calculated by comparing the muon ID efficiencies between the data and Monte Carlo events. The official MuonID efficiencies are measured by the Muon ID group and available in the "muid_eff" packages within the CAFe framework.

In this analysis, the muons are required to be medium nseg3 muons with at least one scintillator hit in A-layer and one in B- and/or C- layers, which is a tighter requirement than the official medium nseg3 quality. The MuonID efficiencies with this addtional requirement are recalculated with the official package "muo_cert" provided by Muon ID group [62]. The modified efficiencies are obtained from $Z \rightarrow \mu\mu$ event both for the data and Monte Carlo samples.

The Data/MC scale factor can be easily applied in CAFe framework with package "caf_eff_util". When the scale factors are applied to the Monte Carlo events, the event weights are adjusted by the factor $\epsilon_{data}/\epsilon_{MC}$, which varies depending on the properties of the muons, e.g. the muon quality, η, ϕ. Figure 5.14 shows the scale factor as a function of η, ϕ for the special mediumnseg3 muons with two scintillation hits.

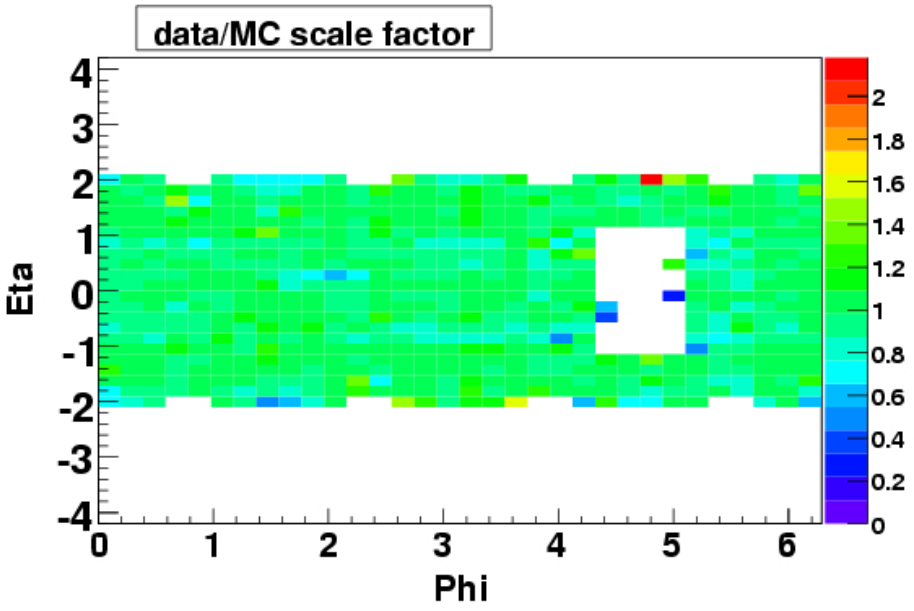

Figure 5.14: The Data/MC scale factor as a function of η and phi for mediumnseg3 muons with at least two scintillator hits.

Chapter 6

Analysis

While the analysis is generally model-independent, we compare the results with predictions from several SUSY models which could result in a charged massive long-lived particles. In this analysis, we use CMSP (charged massive stable particle) to stand for the charged massive long-lived particle. The term "stable" refers to the particles which have a lifetime ($\gtrsim$ 100 ns)long enough to penetrate through the entire detector before decaying. Various supersymmetric models as mentioned in Sections 2.3and 2.4 can predict either the lightest chargino or the lightest stau slepton to be a CMSP.

As mentioned in Section 2.5, the time-of-flight of the particle and the energy deposited in the detector are the two principal distinguishing characteristics for CMSPs. This analysis only uses the timing information in the muon system. We show that meaningful limits can be set without employing the additional information on the energy loss for event selection.

6.1 Experimental Considerations

The CMSPs will lose energy by ionization since they carry electric charge. They will be detected in the muon system after penetrating the entire detector. These particles will travel more slowly than the speed of light due to their heavy mass, while beam-produced muons reaching the outside of the muon detector will be traveling at the speed of light. The signature of the CMSP cascade decays in the detector are model dependent and difficult to simulate accurately. In current analysis, only the pair-production of the lightest staus is considered, and no cascade decays are included. This means that there will be exactly two stable staus in each signal event.

6.1.1 Time-of-flight related variables

Timing information in the muon system will be used to calculate the speed of the particle registering in the muon detector. The DØ muon detector system contains three scintillation counter planes, which can measure the hit times and hit positions. When a particle registers in the muon system, the time of flight and position information can be derived from the scintillator hits associated with the particle. Then the speed of the particle and the error on the speed can be determined based on this hit data. There are certain elements crucial for this analysis:

- Timing in the muon system:

The time needed in the muon system has been adjusted so that light-speed particles are read out with a time of zero. This is accomplished by subtracting a timing value, known as T0, at the front end. Since the T0 is adjusted to be at the center of the trigger gate, the cable length effect was also included. In order to simulate the T0 accurately for each counter, the value is estimated as the time for a light-speed particle to reach the center of the counter.

- Scintillator counter timing resolution:

Not all particles reach the center of the scintillator counters. The signal of such a particle takes different time to be read out compared to those from the center of the counter. This results in a spread in the timing distribution, even for light-speed particles. This spreadof the timing distribution contributes to the timing resolution of the counters as well as the fluctuations of the front end electronics. Since the size of the counter varies depending on the location of the counters, the resolution will be different in different layer regions.

- Speed and speed error for a single layer

The speed for each layer is calculated from the positions of counters which have a scintillator hit. The layer speeds are simply the total distance traveled by the particle divided by the time for the particle to reach the counter. The distance is taken between the scintillator hit position and the z-coordinate of the interaction point. The error in speed can be derived from

$$\sigma_{speed} = v\frac{\sigma_t}{t} \tag{6.1}$$

.

- Average speed (weighted) and speed error

The average speed is calculated with

$$v_{average} = \frac{1}{\sigma^2} \sum_{layer} \frac{v_{layer}}{\sigma^2_{v_{layer}}} \tag{6.2}$$

where $\sigma_{v_{layer}}$ is the speed error in each layer, and σ is the average speed error,

$$\frac{1}{\sigma^2} = \sum_{layer} \frac{1}{\sigma^2_{v_{layer}}} \tag{6.3}$$

In this formula, the higher the measurement accuracy of a layer speed the more it contributes to the final average speed.

- Speed significance and speed significance product

A new variable speed significance is defined as

$$\frac{1 - v_{average}}{\sigma} \tag{6.4}$$

Since there are two particles in each event, another parameter is defined, called the speed significance product, which is the product of the speed significance of each of the pair.

- Speed χ^2

In the reconstruction, it is possible for a muon system hit to be included that is not related to the particle. In order to check whether the times registered in different layers in the muon system are consistent with each other, a χ^2 quantity is defined as

$$\chi^2 = \sum_{layer} \frac{(v_{average} - v_{layer})^2}{\sigma^2_{layer}} \tag{6.5}$$

The quantity is constructed based on the average speed, layer speed and the error on the layer speed. Then χ^2 is normalized by the number of degrees of freedom.

The speed (both layer speed and average speed) in this analysis is calculated in units of c.

6.1.2 Energy loss dE/dx

In the DØ detector, there are principally two sub-detectors which can measure the energy loss of a charged particle.

The first is the Silicon Microstripe Tracker (SMT), which consists of the central tracking system together with the Central Fiber Tracker (CFT). Charged particles travel through the planes of the SMT, deposit energy which registers electric pulse clusters in the system, and the cluster registered by the particle in each plane is called a hit in that plane. The pulse height is proportional to the deposited energy by the particle. The total deposited energy in SMT is the sum of the energy loss in all the planes where there is an associated hit. The material in the SMT detector is the same over the whole system and the thickness of the material in each plane is fixed and uniform. The travel path length of the particle in each plane is then a function of the incident angle. In the d0reco algorithm, the dE/dx value of each track is the average value of the SMT hits associated with the track of that particle. Therefore, the energy loss in the SMT is a function of the incident angle and the velocity of the particle.

The second sub-detector is the calorimeter which measures the energy deposit of the incident charged particle. For muons, the energy loss in the calorimeter is nearly a constant independent of the speed of the incident muon. In the CAF trees, there is a function "eloss" for each muon, which is designed to return the total energy loss of the muon in the calorimeter. However, in the current framework, the return value of this energy loss function is derived from the studies on the Run I data, not the actual value measured in the calorimeter. In principle, the actual energy loss in the calorimeter can be calculated by summing over the calorimeter cells associated along the muon track direction. In this analysis, this information is not included for the final results.

The Silicon Tracker Trigger (STT) is the Level2 (L2) processing system which takes the unsuppressed raw data from the SMT detector as its input. In the STT system, the dE/dx value is derived from the pulse height values of the SMT hits used in the track fit. There are three trigger bits which are not assigned in the STT system. Detailed studies on developing a dE/dx related trigger were performed and are detailed in Appendix B. The studies show that the dE/dx related variables are good candidates for classifying charged massive slow-moving particles from the light-speed muons. However, the current muon triggers already have a good performance on selecting

signal events from the backgrounds. Hence, there is no need to add a new trigger based on dE/dx.

6.2 Event Selection

The "CAFe" framework [50], which takes CAF trees as inputs, is used for the analysis as stated in Section 5.1. Since only direct pair-produced signals are considered, the main goal is to select candidate events with two good "muons". In this analysis, the term "muon" is used to refer to both real muons and CMSPs. The reason is that the CMSPs are not distinguished from muons throughout the standard data collection and reconstruction processes. However, when the CMSPs move too slowly and arrive outside the muon trigger timing gate due to their heavy masses, they do not fire the muon triggers. The effect on the efficiencies of CMSPs from the muon trigger timing gate is stated carefully in sect.5.3.3.

The event selection criteria are developed based on an earlier DØ CMSP study [28] and the studies on the measurement of the cross-section of $Z \rightarrow \mu\mu$[63]. A pair of high p_T muons is required for each event and each muon must have a matched track in the central tracking system. Furthermore, in order to reduce background, at least one of the two muons was required to be isolated. The selection criteria used are listed below:

1) Both muon tracks are required to lie within the geometrical acceptance of the muon chambers. The geometry coverage of the muon system is limited, and that any muon candidates outside the muon chambers should be rejected.

2) Muons detected towards the bottom hole area are rejected. In the central region of the detector, which has $|\eta| \lesssim 1.0$, there are two holes in order to leave enough room for the supporting poles of the calorimeter system. Also, the data communication cables and some power supply cables are routed through these holes. The muon system has poor coverage in these regions, so the muons oriented towards the hole regions are rejected in order to keep the data quality high.

3) Both muons must be of "medium" quality with $\chi^2_\mu/d.o.f.$ of the muon track less than four and must have a matched track in the central tracker. It is possible for particles other than muons to penetrate through the calorimeter and have only a few hits registered in the most

inner A-layer detectors. Such hits could be reconstructed as "muon" tracks with fairly poor quality although they are not real muons at all. In contrast, the real high energy muons and muon-like particles would have much higher possibility to travel through the whole muon system and have hits in the layers outside of the Toroid magnets. The muon quality selection ensures that the muons used in the analysis are good quality muons. The $\chi^2_\mu/d.o.f.$ is the cut on the χ^2_μ of the muon track normalized by the degrees of freedom, which is used to reject the muon tracks constructed from the hits with inconsistent physical positions.

4) For both muons, $p_T \geq 20$ GeV, where p_T is the transverse momentum of the matched central track. This p_T requirement classifies the events with high transverse momentum from the large number of background events with low p_T.

5) The two muons must satisfy between them two of the four possible isolation criteria below, in any combination:

   - $\sum_{cone0.5}(p^\mu_T) < 2.5$ GeV, where $\sum_{cone0.5}(p^\mu_T)$ is the sum of p_T of tracks contained within a cone around the muon of width $\Delta R < 0.5$.
   - $\sum_{halo}(E^\mu_T) = \sum_{cone0.4}(E^\mu_T) - \sum_{cone0.1}(E^\mu_T) < 2.5$ GeV, where $\sum_{cone0.1}(E^\mu_T)$ and $\sum_{cone0.4}(E^\mu_T)$ are sums of the E_T of calorimeter clusters in cones around the muon of width $\Delta R < 0.1$ and $\Delta R < 0.4$, respectively. In formatting these sums, cells in the electromagnetic and fine hadronic calorimeters are considered, but not those in the coarse hadronic calorimeter.

   The isolation criteria are set in order to reject the muons from the meson decays and other non-isolated muons. The isolation cut values are studied and optimized by the muonID group [48].

6) The event was required to fire one of the triggers listed in Table 5.1.

7) Cosmic ray events in reconstruction appear as two essentially back-to-back collinear muons. In contrast, the directly pair-produced CMSP signal particles would travel from the same point however with a large angle between their moving directions. This angle could be large, but will not equal π exactly. To reject the cosmic events effectively, we require that the

pseudo-acolinearity $\Delta\alpha = |\Delta\phi + \Delta\theta - 2\pi|$ is larger than 0.05. The cut value on the pseudo-acolinearity was studied and set by the DØ $Z \rightarrow \mu\mu$ cross-section study group [63].

8) The distance-of-closest-approach (DCA) of the muon with respect to the primary vertex of the event in the $r\phi$ plane can be used to reject those muon candidates that do not originate from the primary vertex. Some examples are the cosmic ray muons and beam halo. Since the accuracy of the DCA is greatly affected by whether there is any measurement in SMT for the central track, the criteria on DCA should be placed separately in two cases depending on the number of SMT hits. So the requirement is that the DCA of the muon must be less than $0.02\,cm$ if there's an SMT hit; or less than $0.2\,cm$ if there is no SMT hit.

   Additionally, the difference between the z coordinates at the DCAs of the two muons should be less than 3 cm. These requirements on the DCA are added in order to make sure that the muon pair in the event oriented from the same primary vertex. Also, this criteria rejects the possibility that one of the tracks is really badly meaured. The DCA requirements use the values set by the the DØ $Z \rightarrow \mu\mu$ cross-section study group [63].

9) Cosmic ray muons are also rejected with the timing requirements. Some cosmic ray events may pass the previous $\Delta\alpha$ cut.

   The cosmic ray events could penetrate through the detector in any direction with any angle. It is not necessary for the cosmic rays to be close to the beam-pipe (actually the primary vertex (PV)) either. This means that cosmic ray muons could have much larger DCAs compared with the beam-produced muons. Those cosmic rays with large DCAs are rejected by the DCA cuts we described previously.

   Also by examining the timing information for the muons, cosmic rays can be rejected as well. There are some commonly used default timing cuts in CAFe framework. The muon must arrive within $\pm 10\,ns$ in the timing gates for each layer where it has a scintillator hit. This has been studied by muon ID group in Ref. [48] and is good enough for most of the analysis in which the normal beam-prompt muons are selected. However, it could reject our signal particles easily since most of the heavy particles would move slowly and arrive much later than the normal muons.

We developed our own cosmic ray muon timing cuts which were obtained from studies with data using four long cosmic runs taken during the Run IIa period. The run numbers for the cosmic runs are 178607, 190908, 212117 and 212692. Most of the cosmic muon-pairs are rejected by requiring both muons to have medium muon quality with matched central tracks, but to study their timing distributions, we relaxed these criteria. The cosmic muon will be reconstructed as an event with a pair of muons.

As the cosmic ray travels into the detector on one side and out of the detector on the other, such events will have scintillation counter timings different from those of particles both produced in an interaction at the center of the detector. Two timing parameters were defined to distinguish the beam-produced muons from the cosmic rays: the absolute value of the difference between A-layer times of the two muons and the C-layer time minus A-layer time for both muons in the events.

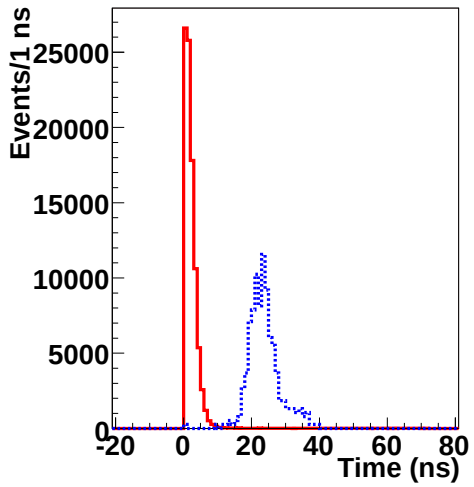

Figure 6.1: The absolute value of the difference between the A-layer time of the two muons in each event comparing beam-produced muons (red solid line) with cosmic data (blue dash line). The histograms in the plots are normalized to have the same number of events.

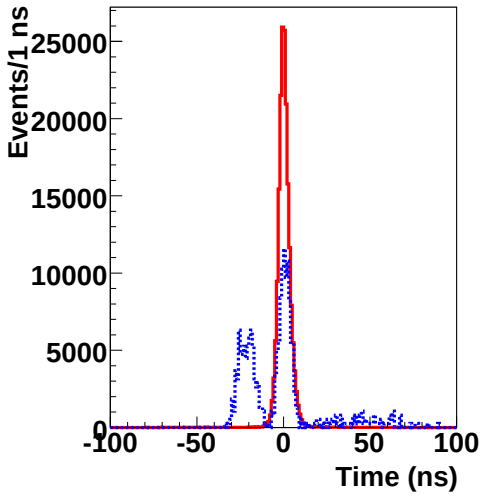

Figure 6.2: The C-layer time minus the A-layer time for both muons in the events comparing beam-produced muons (red solid line) with cosmic data (blue dash line). The histograms in the plots are normalized to have the same number of events.

The timing distributions for both cosmic data and beam-produced muons are compared in Fig. 6.1 and Fig. 6.2. The differences between the beam-produced muons and the cosmic data are used to determine the cut values to reject the cosmic data effectively.

As mentioned earlier, the time registered in the muon system is the actual travel time minus the T0. So for beam-produced outgoing muons, the time for the muon to travel from one layer to another is taken care of by T0. The readout time for outgoing muons should be around zero ns within the scintillator counter resolutions. This designed feature in the registered muon timing explains why the A-layer time difference between the outgoing pair-produced muons is close to zero ns. However, the time difference of one particle travel through the detector from one side to the other will be significantly larger than zero ns.

The time difference between the outer B-/C-layer hit and the inner A-layer hit is defined as: $T_C - T_A$ if there is a C-layer hit; or $T_B - T_A$ if there is only a B-layer hit but no C-layer hit. This results in the small splitting in the first peak near -20 ns for cosmic data in Fig. 6.2, which is the contribution from the reconstructed muon moving from outside the detector towards the center. However, the time difference for the beam produced muon is still around

zeron ns after taking T0 into account. As expected, one reconstructed muon in the cosmic ray event will move in the outgoing direction as it were produced from the beam collision. So the $T_C - T_A$ or $T_B - T_A$ for this muon would have a similar value as the beam-produced muons. In the figure, we do observe the second peak around zero ns for cosmic data , which is mainly for the reconstructed muon moving in the outgoing direction from the center of the detector.

In the central muon system, no scintillation counters are mounted in the top B-layer. The scintillation counters are only placed in the region below the beam-line (i.e. with negative y coordinates) in the side and the bottom region for B-layer. When penetrating through the central muon system, the cosmic rays will have a smaller chance to register in the top/top-side regions than the bottom/bottom-side regions. Most of the cosmic rays travel in the downwards direction through the central muon system, so the reconstructed muons from those cosmic rays will travel more likely in the same direction as the beam produced muons.

To sumerize, the following set of timing selection criteria is used to reject cosmic ray background (cosmic ray muons that can pass through the detector at any time and can be wrongly identified as slow-moving particles). An event is rejected if any of the following conditions is true:

- The distance of closest approach to the PV of either muon is larger than $0.2\,cm$.
- The absolute value of the difference in A-layer times of the two muons is larger than $10\,ns$.
- The C-layer time minus the A-layer time for either muon is less than $-10\,ns$.

10) The timing information from the muon system was then used to calculate the speed of each muon in the event. It is possible that some hits not registered by the muon are grouped into the muon track during the reconstruction process. Those mis-identified hits could have the registered time uncorrelated with other real hits of the muon, although they have close physical positions. Then the calculated speeds of the muons with such hits are not reflecting the real travel velocity of the particle. We developed a selection criterion to ensure that the registered times in the muon detector are consistent with each other. The procedure sequence is performed as following:

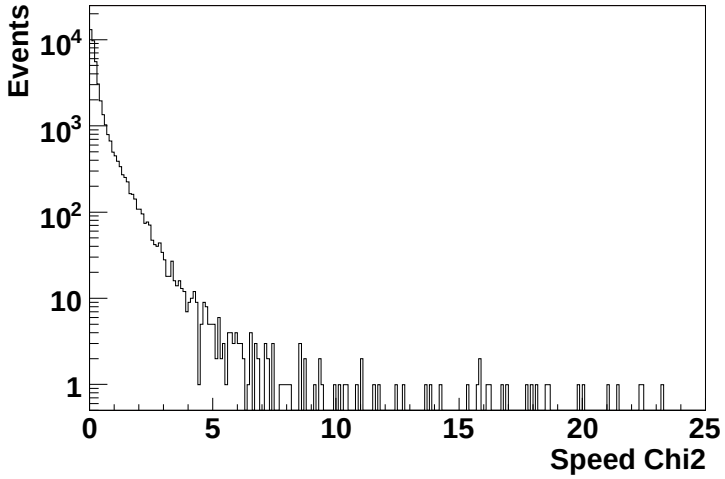

Figure 6.3: Speed χ^2/dof for Z$\mu\mu$ events in real data.

- The central track matched to the muon is extrapolated to the plane containing the scintillator hit.
- The distance between the scintillator hit position and the production position is then obtained. The production point is assumed to be at $x = y = 0$ and the z-coordinate is taken to be the z position at the distance of closest approach to the beam line.
- Due to the timing offset in the muon system, a "T0" is added back to the scintillator time obtained from the readout. This "T0" is calculated as the time for a speed of light particle to travel from the center of the detector to the center of the counter.
- Speed is then calculated in each layer in which the muon has a scintillator hit. The layer speed is simply the total distance traveled by the muon to reach the counter divided by the recorded time for the muon to reach the counter.

The speed χ^2 is defined in Eq. 6.5 in Section 6.1. The χ^2 is normalized by the number of degrees of freedom for each particle in the event. This cut removes the particles whose individual time measurements in different layers are not consistent with each other. The cut on $\chi^2/d.o.f.$ is derived from $Z \rightarrow \mu\mu$ decays in real data, as shown in Fig. 6.3. The value on $\chi^2/d.o.f.$ is chosen to be 4.7 so that most of the Z decay events (99.73%) have both particles passing the selection.

An examination of the data for events with high $\chi^2/d.o.f.$ values supported this conclusion. In a future analysis, this variable should be re-examined and optimized.

11) This selection cut is on the asymmetry of the transverse momenta of the two muons in the event.

The transverse momenta asymmetry is defined as

$$p_T^{asym} = \frac{\left|p_T^1 - p_T^2\right|}{p_T^1 + p_T^2} \tag{6.6}$$

$p_T^{asym} = \frac{|p_T^1 - p_T^2|}{p_T^1 + p_T^2}$ where $p_T^{1,2}$ is the transverse momentum of the first (second) particle in the event.

Since the analysis is concentrating on the pair-produced CMSPs, the transverse momenta of the two particles are expected to be equal or similar. However, the momentum resolution in the central tracker is worse for high momentum tracks than for low momentum ones. For the CMSP search, each of the signal particles has a high momentum, and thus there is a significant probability that the measurement of at least one of the tracks has a large error. These measurement errors can give rise to large uncertainties in the calculated invariant mass of the muon pairs. As we use the invariant mass as a parameter to separate signal from background, we need to reject events with one muon associated with an obviously mis-measured p_T. The new variable p_T^{asym} is designed intentionally to remove such events. We used the $Z \rightarrow \mu\mu$ decays in real data (as shown in Fig. 6.4) to determine the value of the p_T^{asym}. In order to remove those events in the tail of the p_T distribution, we require that most Z decay events should have a reliable measured p_T^{asym} . The final cut value is set to 0.68 so that 99.73% Z decay events pass this cut.

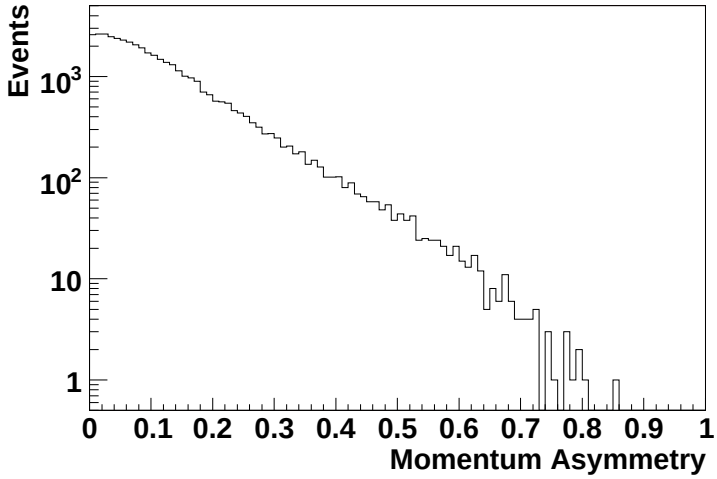

Figure 6.4: P_T Asymmetry for Z$\mu\mu$ events in real data.

The final p_T^{asym} cut value was derived based on the assumption that the muons will have close p_T in the pair-production events, like $Z \rightarrow \mu\mu$. We studied both the generator-level and the reconstruction-level information for the $Z \rightarrow \mu\mu$ MC events. The p_T^{asym} at the generator level, plotted in Fig. 6.5, is expected to be near zero. The events are required to have $p_T > 20. GeV$ for both muons at generator level. The p_T^{asym} at generator level also ends about 0.68, which is close to the cut value we set.

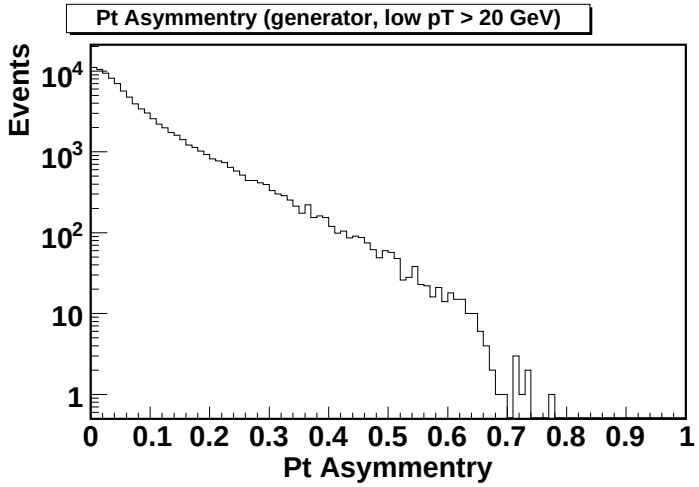

Figure 6.5: P_T Asymmetry for $Z \rightarrow \mu\mu$ MC events at generator level.

Subsequent study of individual $Z \rightarrow \mu\mu$ events has shown that the final cut value is not optimized. Although some rejected events include a particle having an obviously unphysical p_T in real data, there are also a few rejected events with two muons having very different but reasonable measured p_T. In future analysis, this selection criteria should be re-evaluated and perhaps replaced by new variables.

12) Criteria on the variables based on the muon system information, e.g. the speed of the particle calculated with both the timing and the position of the scintillator hit.

The variables calculated from the scintillator timing information in the muon system are used to separate the slow-moving particles from the light-speed muons. In order to take the resolutions of the muon system into account, a new variable is defined in Eq. 6.4. Since the CMSPs will move slowly and arrive at the muon system later than the light-speed particles, the speed significance of the CMSPs will be positive. In contrast, the light-speed particles will have the speed significance as zero within the resolution of the muon system. Figure 6.6 compares the speed significance distributions of the data events and the signal events (100 GeV and 300 GeV CMSP) passing all the previous selection criteria.

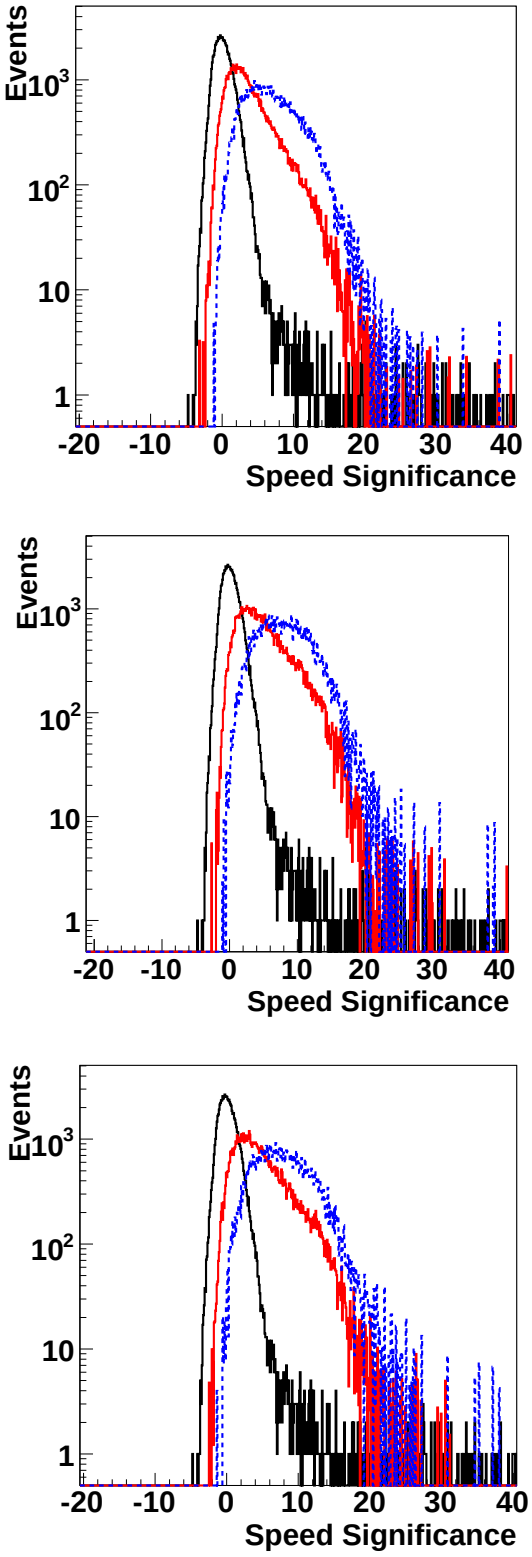

Figure 6.6: Significance distribution of events comparing data (black), 100 GeV CMSP (red) and 300 GeV CMSP(blue). Top plot is for Stau, middle for gaugino-like chargino and bottom for higgsino-like chargino. The histograms in the plots are normalized to have the same number of events.

Similar to the p_T asymmetry cut, the two particles in the the pair-production of the signal events, should have comparable velocity at the generator level. Therefore, the newly defined variable, the speed significance, should be measured with positive values for both candidates. As observed from Fig. 6.6, the speed significance distribution is nearly symmetric, centered at zero for $Z \rightarrow \mu\mu$ events. However, the distributions of the CMSPs are very asymmetric around zero, the positive values being the majority.

Another new variable, the speed significance product, is defined as the product of the significances of the two muon candidates in the events. The speed significance product has the advantage that it includes the information from both muon candidates and takes into account the uncertainty in the measured speeds. The reason that the criteria is not placed on the speed significance product of the muon pair is because the speed significance product is also positive for pairs with two negative speed significance particles. In order to reject most of the $Z \rightarrow \mu\mu$ events which have the measured muon speed close to the light speed, a criteria is applied that qualified events must have positive speed significance values for both particles in the muon pair.

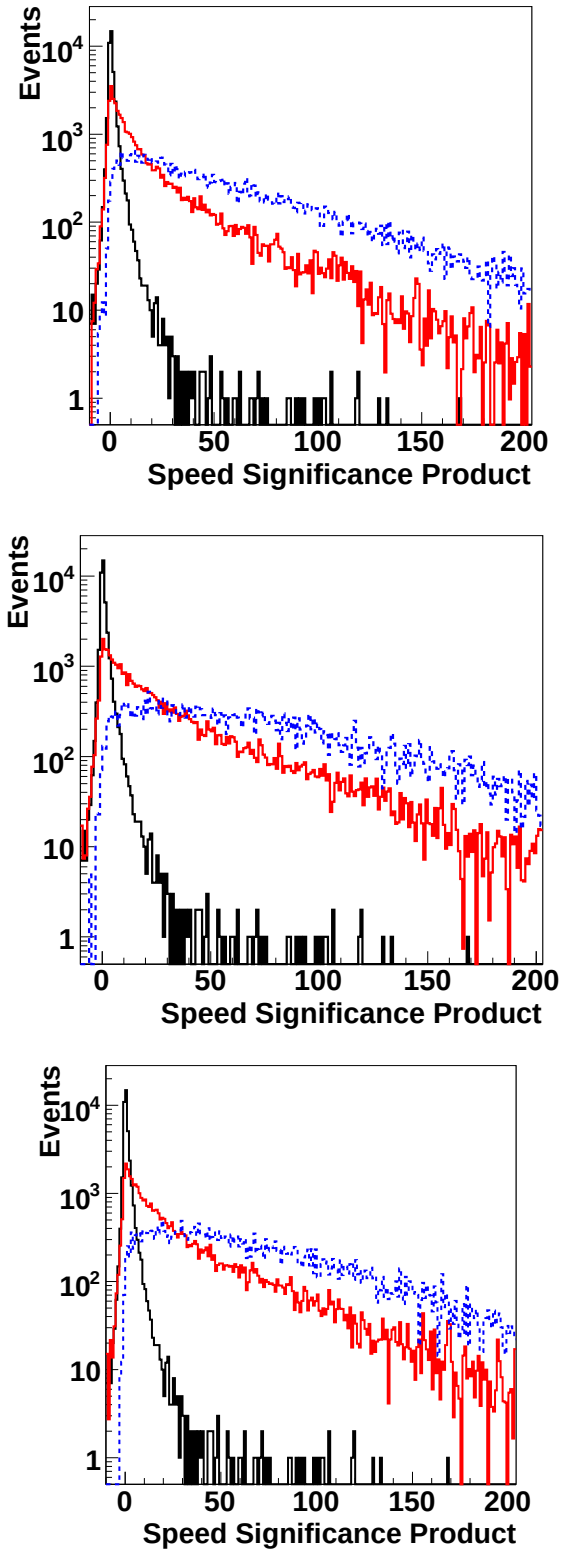

Figure 6.7: Significance product distribution of events comparing data (black), 100 GeV CMSP (red) and 300 GeV CMSP(blue). Top plot is for Stau, middle for gaugino-like chargino and bottom for higgsino-like chargino. The histograms in the plots are normalized to have the same number of events.

The selection efficiencies for all mass points in the three models that were considered are listed in Table 6.1 through Table 6.3.

Mass (GeV)	60	80	100	150	200	250	300
Bottom	98.0%	98.2%	99.3%	99.6%	99.7%	99.8%	99.8%
Medium	85.5%	87.4%	89.3%	90.5%	90.5%	90.0%	89.7%
Nseg3	84.1%	86.0%	87.8%	89.1%	89.0%	88.6%	88.1%
Track	81.7%	83.7%	85.8%	87.5%	87.6%	87.2%	86.8%
χ^2_μ	81.3%	83.4%	85.6%	87.3%	87.4%	87.1%	86.6%
DCA	81.2%	83.4%	85.5%	87.2%	87.4%	87.0%	86.5%
P_T	80.7%	83.1%	85.4%	87.1%	87.3%	87.0%	86.5%
Number	37.4%	39.1%	40.7%	42.2%	41.8%	41.9%	40.8%
Trigger	24.3%	25.4%	26.3%	27.0%	26.5%	26.4%	25.6%
MUID	24.2%	25.2%	26.1%	26.8%	26.3%	26.1%	25.3%
MUTRK	22.7%	23.6%	24.4%	25.0%	24.4%	24.2%	23.4%
L1MU	20.8%	21.3%	21.5%	20.5%	18.6%	16.6%	14.3%
Isolation	20.7%	21.2%	21.4%	20.4%	18.5%	16.5%	14.3%
Δ	20.5%	21.0%	21.2%	20.2%	18.2%	16.1%	13.9%
Cosmic	20.3%	20.8%	21.0%	20.0%	18.0%	16.0%	13.8%
χ^2	20.3%	20.7%	20.6%	19.9%	17.9%	15.9%	13.8%
P_T^{asym}	20.1%	20.3%	20.4%	19.0%	16.6%	14.3%	12.1%
Significance	16.6%	17.7%	18.3%	18.1%	16.2%	14.1%	12.0%

Table 6.1: Selection cut efficiencies for stau signal events.

Mass (GeV)	60	80	100	150	200	250	300
Bottom	90.3%	93.4%	95.1%	96.5%	97.1%	97.3%	97.6%
Medium	62.5%	69.7%	72.2%	74.6%	74.8%	73.7%	73.4%
Nseg3	60.6%	67.7%	70.3%	72.5%	72.8%	71.5%	71.1%
Track	57.6%	64.8%	67.5%	70.1%	70.4%	69.3%	69.0%
χ^2_μ	57.2%	64.4%	67.1%	69.8%	70.1%	69.0%	68.7%
DCA	57.1%	64.4%	67.1%	69.7%	70.1%	68.9%	68.7%
P_T	54.7%	63.6%	66.7%	69.6%	70.0%	68.8%	68.6%
Number	20.0%	24.8%	26.6%	29.1%	29.1%	28.4%	28.0%
Trigger	13.3%	16.4%	17.6%	19.0%	19%	18.4%	18.08%
MUID	13.3%	16.3%	17.5%	18.9%	18.9%	18.3%	18.0%
MUTRK	12.5%	15.4%	16.5%	17.8%	17.7%	17.1%	16.8%
L1MU	11.2%	13.3%	13.6%	12.7%	10.7%	8.5%	6.9%
Isolation	11.1%	13.2%	13.5%	12.6%	10.6%	8.5%	6.9%
Δ	11.1%	13.1%	13.4%	12.4%	10.5%	8.3%	6.7%
Cosmic	11.0%	13.0%	13.3%	12.3%	10.4%	8.2%	6.7%
χ^2	10.9%	13.0%	13.2%	12.3%	10.4%	8.2%	6.6%
P_T^{asym}	10.9%	12.9%	13.1%	12.0%	9.9%	7.7%	6.0%
Significance	9.8%	11.8%	12.3%	11.6%	9.8%	7.6%	6.0%

Table 6.2: Selection cut efficiencies for gaugino-like chargino signal events.

Mass (GeV)	60	80	100	150	200	250	300
Bottom	91.4%	93.9%	95.3%	96.8%	97.4%	97.6%	97.8%
Medium	65.2%	71.5%	73.6%	76.1%	76.9%	75.6%	74.7%
Nseg3	63.4%	69.6%	71.8%	74.2%	74.8%	73.6%	72.6%
Track	60.5%	66.8%	69.1%	71.6%	72.5%	71.4%	70.4%
χ^2_μ	60.0%	66.3%	68.7%	71.3%	72.2%	71.1%	70.2%
DCA	59.9%	66.3%	68.7%	71.3%	72.2%	71.0%	70.1%
P_T	57.7%	65.6%	68.3%	71.2%	72.1%	71.0%	70.1%
Number	21.6%	25.9%	27.8%	30.1%	30.4%	29.9%	29.2%
Trigger	14.3%	17.1%	18.3%	19.7%	19.7%	19.3%	18.8%
MUID	14.3%	17.1%	18.2%	19.6%	19.6%	19.2%	18.6%
MUTRK	13.4%	16.0%	17.1%	18.4%	18.4%	17.9%	17.4%
L1MU	12.2%	14.0%	14.2%	13.5%	11.6%	9.5%	7.6%
Isolation	12.2%	13.9%	14.1%	13.4%	11.5%	9.5%	7.5%
Δ	12.1%	13.8%	14.0%	13.3%	11.3%	9.3%	7.3%
Cosmic	119%	13.6%	13.8%	13.1%	11.2%	9.2%	7.3%
χ^2	11.9%	13.6%	13.8%	13.1%	11.2%	9.2%	7.3%
P_T^{asym}	11.9%	13.5%	13.6%	12.7%	10.6%	8.5%	6.5%
Significance	10.5%	12.3%	12.6%	12.3%	10.5%	8.4%	6.5%

Table 6.3: Selection cut efficiencies for higgsino-like chargino signal events.

Row "Bottom" shows the fraction of signal events after rejecting muons from the bottom hole area. "Medium" requires that the muon must be identified as medium or tight. "Nseg3" means the muon must have segments in both the A-layer and B-/C- layer. "track" requires that the muon must have a matched track in the central tracking system. "χ^2_μ" means that the $\chi^2$of the muon track in the muon system normalized by the degree of freedom must be less than 4. This selection cut is provided in the CAFe processor, which is obtained and released based on the studies done by the muon ID group. "DCA" is the requirement discussed previously: the DCA of the muon must be less than $0.02\,cm$ if there are any SMT hits; or less than $0.2\,cm$ if there are only CFT hits with no SMT hit in the matched central track. "P_T" requires that the transverse momentum of the matched central track must be larger than or equal to 20 GeV. "Number" means that the number of the good muons passing previous selection must be exactly 2. "Trigger" is the average value of the adjusted event weight in Monte Carlo events after applying the di-muon trigger efficiency scale factors. "MUID" and "MUTRK" are those values after the muon ID efficiency re-weighting and the muon track efficiency re-weighting, respectively. "L1MU" denotes the fraction of events with registered times within the muon system L1 trigger gates. "Isolation" requires events passing the isolation cuts. "Δ" requires events passing pseudo-acolinearity cuts. "cosmic" requires that both muons in events must pass the cosmic rejections. "χ^2" requires that events must pass the speed χ^2cut, while "P_T^{asym}" requires that events pass the cut on transverse momentum asymmetry. "Significance" requires both particles to have positive speed significance.

Both the L1 Muon trigger gate efficiency and the selection cut efficiencies are different in three models even for the same mass CMSP. The generator level β of the pair-product CMSPs are compared at the same mass point, which is shown in Fig. 6.8. With the same mass, the stau leptons have higher β and move faster than charginos so that there are more stau leptons firing the trigger gate than the charginos.

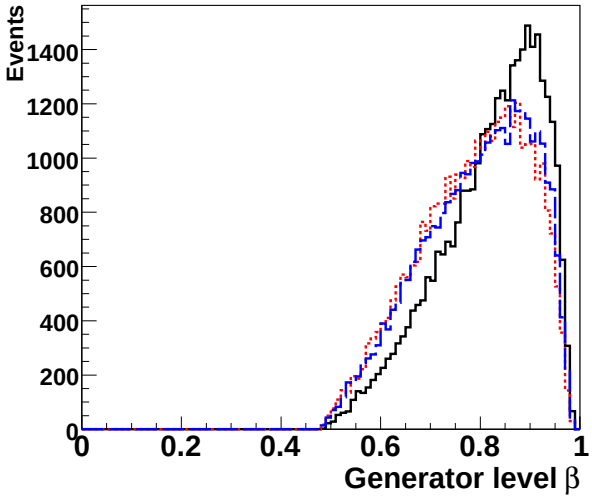

Figure 6.8: The comparison of the generator level β distributions of the pair-produced 100 GeV CMSPs. The black line is for stau leptons, the red dotted line is for the gaugino-like charginos and the blue dashed line for the higgsino-like charginos.

Two additional distributions, the invariant mass and speed significance product of the muon pair in the events shown in Figs. 6.9 and Fig. 6.10 respectively, were plotted to compare the distributions between the real data events and signal samples passing all selection cuts.

The invariant mass of the muon pair in the event is defined as

$$M_{\mu\mu} = \sqrt{(E^1 + E^2)^2 - (p_x^1 + p_x^2)^2 - \left(p_y^1 + p_y^2\right)^2 - (p_z^1 + p_z^2)^2} \tag{6.7}$$

where $p^i_{x,y,z}$ $(i = 1, 2)$ is the momentum component of the particle i in the muon pair along the x, y, z direction, and

$$E^i = \sqrt{m_\mu^2 + (p^i)^2}\ (i = 1, 2) \tag{6.8}$$

is the total energy of the particle i in the muon pair in the event, m_μ is the mass of the muon particle, and p^i is the momentum of the particle i. In d0reco packages, the algorithm cannot classify the CMSPs from the normal muons registered in the muon system. So in the algorithm, the CMSPs will be reconstructed in the same way as the beam produced muons, and the total energy of each particle will be calculated with the muon mass instead.

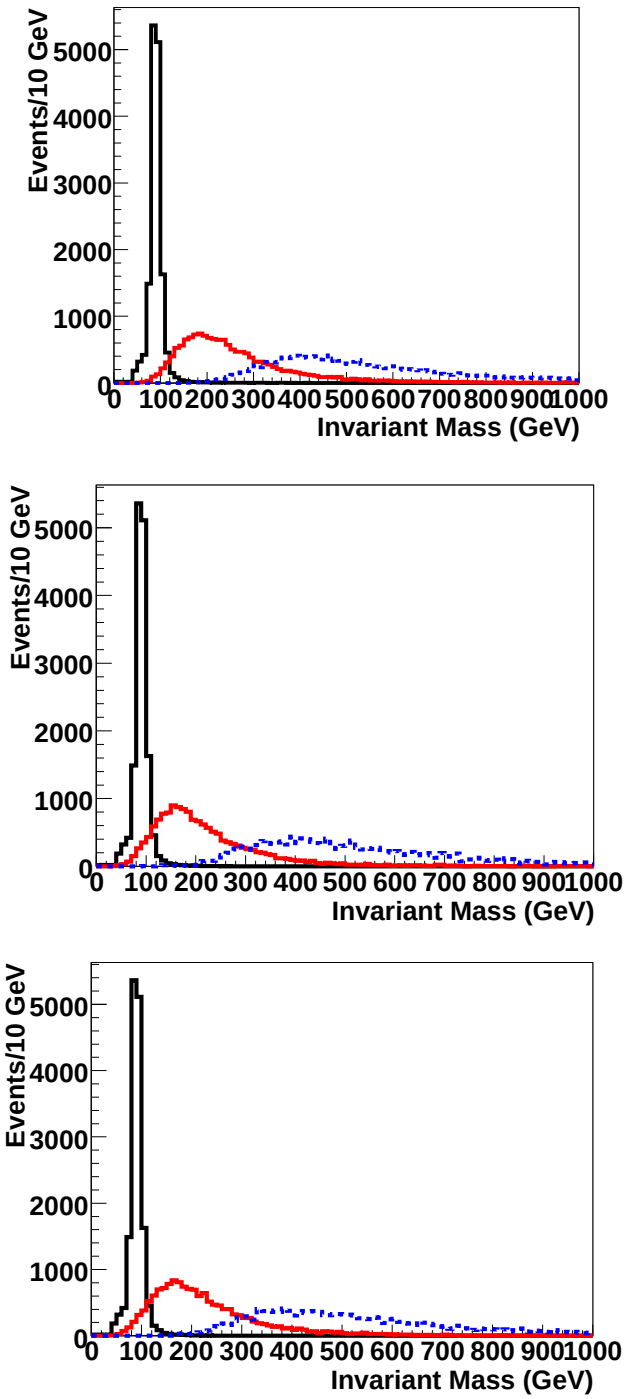

Figure 6.9: The invariant mass distribution of events comparing data (black), 100 GeV CMSP (red) and 300 GeV CMSP(blue). Top plot is for Stau, middle for gaugino-like chargino and bottom for higgsino-like chargino. The histograms in the plots are normalized to have the same number of events.

In the pair production of the signal events, the momenta of the two particles have close values in opposite directions. In other words, the sums of the momenta in all directions are nearly zero. Therefore, the invariant mass of the muon pair in the event mainly depends on the sum of the energies of the two particles. Obviously, the energy of the CMSP will be much larger than that of the normal muon due to the large momentum. This explains why the invariant mass of the muon pair in the event has very different distributions in the real events compared with the CMSP signal events, as shown in Fig. 6.9.

The speed significance product of the muon pair in the events is the direct product of the speed significance of the two muons in the events.

We also examine whether there is any correlation between the invariant mass and the speed significance product of the muon pair in the event. The two values are measured in two independent detector systems and calculated separately. The invariant mass uses the measurements in the central tracking system, while the speed significance product is measured in the muon system. Figure 6.10 shows the speed significance product vs. the invariant mass of the two muons in the event, passing previous selection cuts, for real data, 100 GeV stau and 300 GeV stau samples.

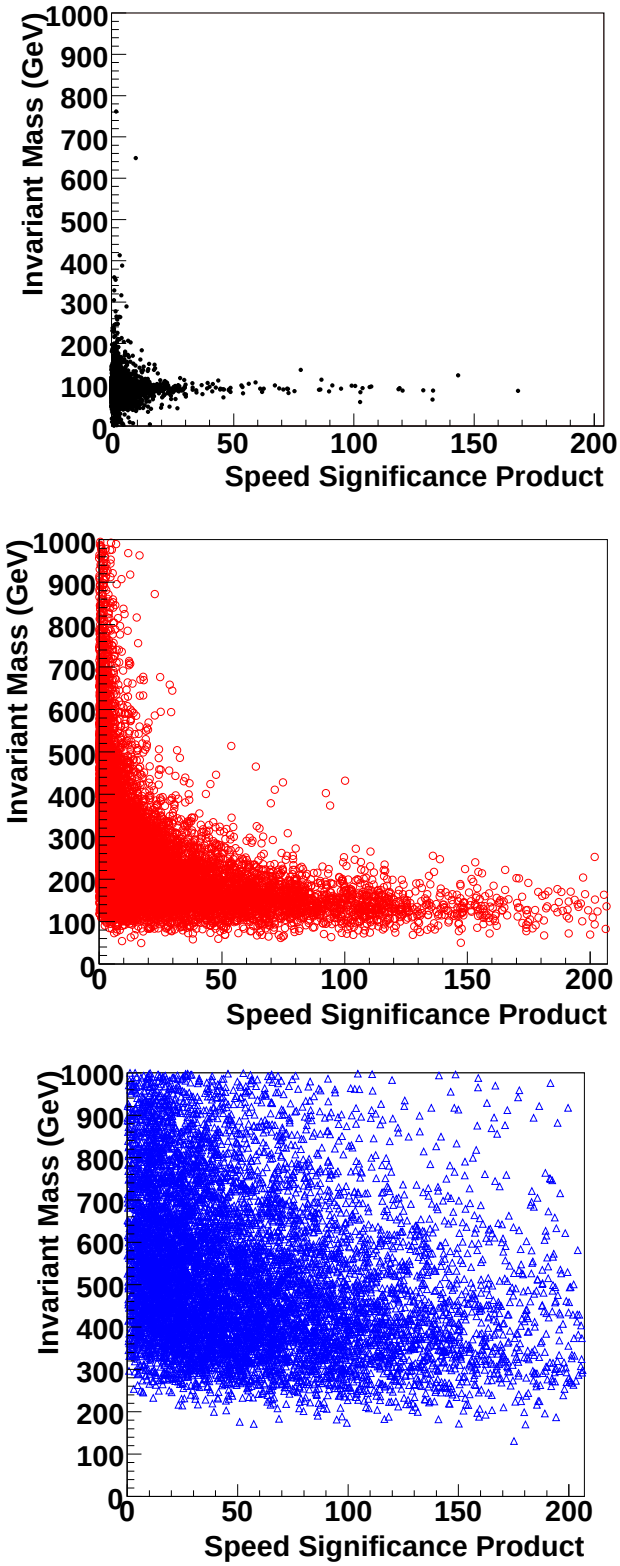

Figure 6.10: The speed significance product distribution vs invariant mass of events comparing data (black points), 100 GeV CMSP (red circles) and 300 GeV CMSP(blue triangles).

The invariant mass and speed significance product of the muon pair in the event are the two key variables we used to discriminate the signals from the backgrounds with the joint likelihood method, which will be discussed in Section 6.4.

6.3 Background Estimation

There is no theory or standard model physics background for our studies. However, due to the limitations of the detector performance, there can be events which have a anomalously large time-of-flight or mis-measured p_T. The mis-measured timing in the muon system will record a large travel time, which results in a small calculated speed and positive speed significance of the particle. Similarly, the mis-measured p_T in the central tracking system will lead to a large invariant mass for the events.

In the events passing the selection criteria, there are events with those mis-measurements. Those mis-measurements lead to the possible mis-classify the background as the signal. We need to estimate the number of such events after applying all the previous selection criteria.

The p_T of the particle is measured in the central tracking system and the time-of-flight is recorded in the muon detector; both systems operate independently of each other. For this reason, the background events can be simulated by combining separate distributions of the invariant mass and of the speed significance product of the muon pair.

The invariant mass distribution for the background is modeled from the data events which have muon candidates with negative speed significance, but pass all the selection criteria. Note that this data sample cannot include any signal events. Since the events are required to have positive speed significance for both muons in order to pass all the selection criteria, there is no overlap of events between the data selection for background simulation and the signal data set. In other words, the data set which is used to simulate the invariant mass of the background events has no contamination from the signal.

Events, which pass all the selection criteria and have an invariant mass within the Z mass peak region (between 70 GeV to 110 GeV), are selected to estimate the speed significance product distribution for the background. The speed significance product of the muon pair for the background

events are simulated by the selected events passing all the selection criteria with invariant mass in Z peak. In this Z peak region, the contamination from the signal is negligible.

There is no overlap of events between these two data sets. Background events are simulated by choosing a random value from each of the above two distributions, the invariant mass and the speed significance product.

There are 100 K background events simulated in the mentioned method. Figure 6.11 is the invariant mass distribution for the simulated background events.

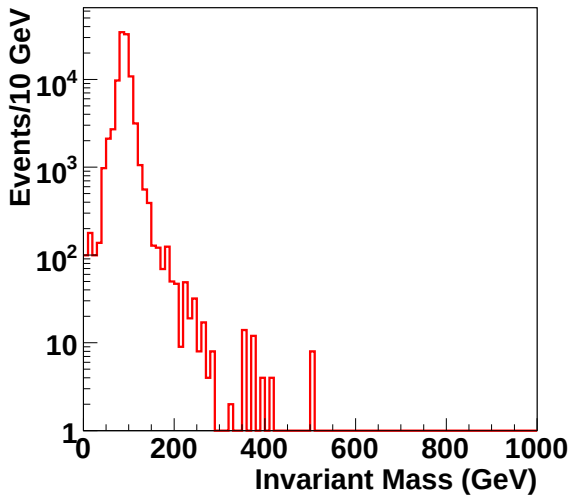

Figure 6.11: Invariant mass distribution of two muons for the 100 K simulated background events.

Figure 6.12 is the speed significance product of the muon pairs for the simulated background events.

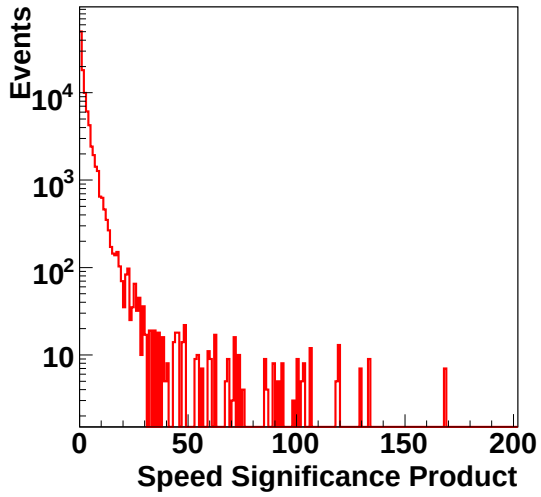

Figure 6.12: The speed significance product of the two muons for the 100 K simulated background events.

Figure 6.13 is the 2-dimensional scatter plot for the invariant mass versus the speed significance product of the simulated background events.

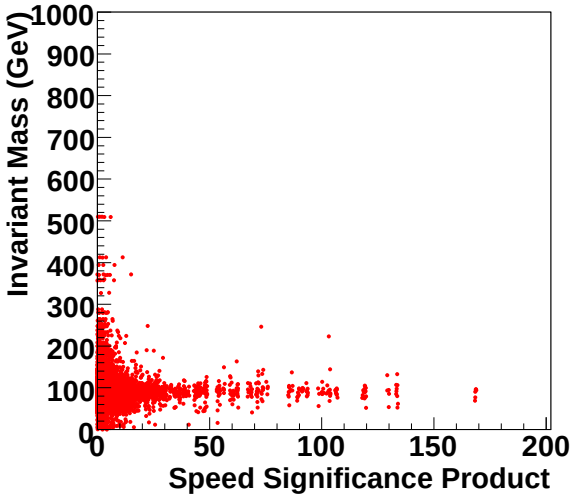

Figure 6.13: Invariant mass vs. speed significance product of the two muons for the 100 K simulated background events.

By construction, there is a correlation between the real data and the data-based simulated back-

ground in the speed significance product distribution, which is not true in the invariant mass of the muon pair. However, by randomly selecting from both templates, drawn from the non-overlapping data sets, the variables are decorrelated for the simulated background events. On the contrary, signal samples have an obvious correlation and peak more strongly at high likelihood values, which are calculated in Section 6.4.

Then the simulated background events are normalized to the number of Z and Drell-Yan events passing all the selection criteria. After the selection criteria, the data samples are completely dominated by the muons from Z and Drell-Yan events. It is reasonable to normalize the estimated number of background events to that of the Z and Drell-Yan events passing all the selection criteria.

6.4 Likelihood Method

The invariant mass and the speed significance product of the muon pair in the events passing all the selection criteria are very different for the Monte Carlo signal samples (stau 300 GeV), which are shown as dotted lines in Fig. 6.14 and Fig. 6.15, compared with those of the simulated background drawn in solid lines, and the real data as dots with error bars.

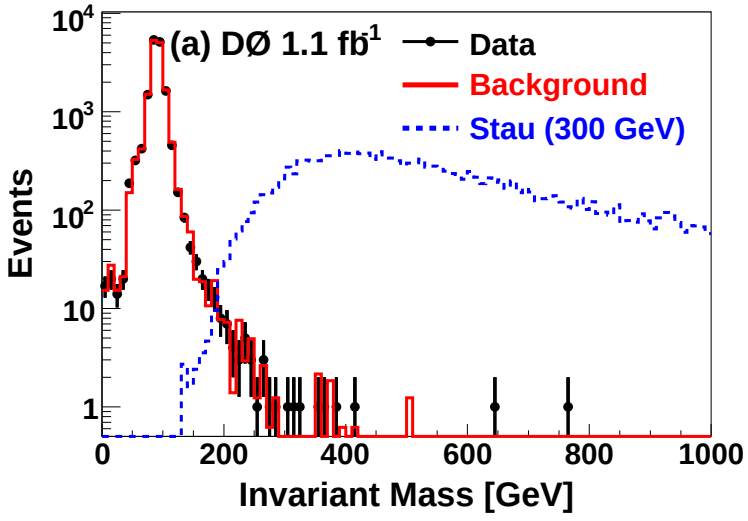

Figure 6.14: Invariant mass distributions of the muon pair for the simulated background (solid line), the 300 GeV stau signal (dotted line), and the data (as dots with error bars) passing the selection criteria.

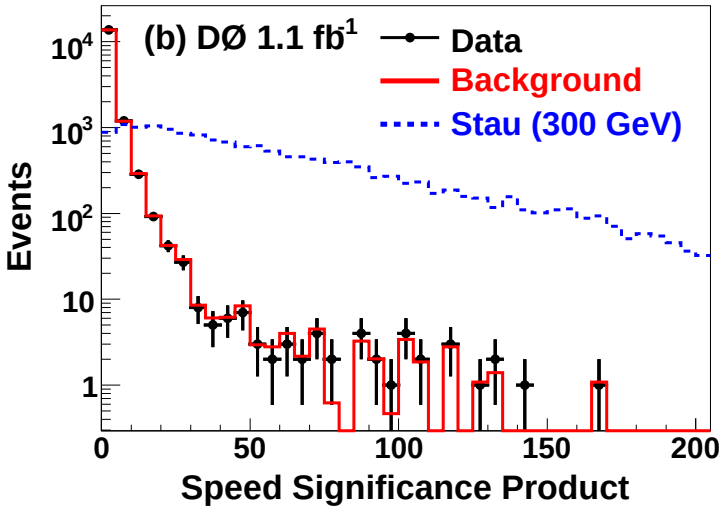

Figure 6.15: Speed significance product distributions of the muon pair for the simulated background (solid line), the 300 GeV stau signal (dotted line), and the data (as dots with error bars) passing the selection criteria.

The likelihood method[64] is used in this analysis in order to discriminate between the background and signal events. The joint likelihood function is constructed based on the two inputs which are the variables calculated for the pair of muons: the muon pair invariant mass and the corresponding speed significance product. The likelihood function is defined as

$$p(x|i) = p_{mass}(x|i) * p_{sig}(x|i) \tag{6.9}$$

where x is the character vector (sig, mass), variable i stands for the different class (background or signal), and the "$mass$" stands for the invariant mass of the muon pair, "sig" for speed significance product of the two muons in the muon pair.

The distributions of the 100 K-simulated background events are used to construct the background probability functions, which then are combined as the background likelihood function. Meanwhile, the signal likelihood function is built based on the two distributions of the muon pairs for each mass point in all three models, separately. In other words, the background probability functions are fixed, however, the signal probability functions vary depending on the mass and model type of the signal samples.

During the construction of the probability functions, it has been observed that the distributions for both the simulated background and the signal samples are discrete, especially at the high value region, while they are continuous at the low end. This arises from the fact that there are not enough events in statistics, particularly with high values. The bins with zero entries in both histograms do not mean that the probabilities for those values are zero. When there are enough statistics, there will be non-zero entries in these bins. So we keep the small bin width at the low region and enlarge the bin width at the high region in order to cover the empty bins without affecting the whole shape.

The discriminant function is defined as

$$g(x) = \frac{S(x)}{S(x) + B(x)} \tag{6.10}$$

where $S(x) = p(x|signal)$ and $B(x) = p(x|background)$ are the likelihood functions for the character vector x, given that the sample is signal or background, respectively. The output of the likelihood discriminant for both simulated background and Monte Carlo signal (stau 100 GeV) samples is shown in Fig. 6.16

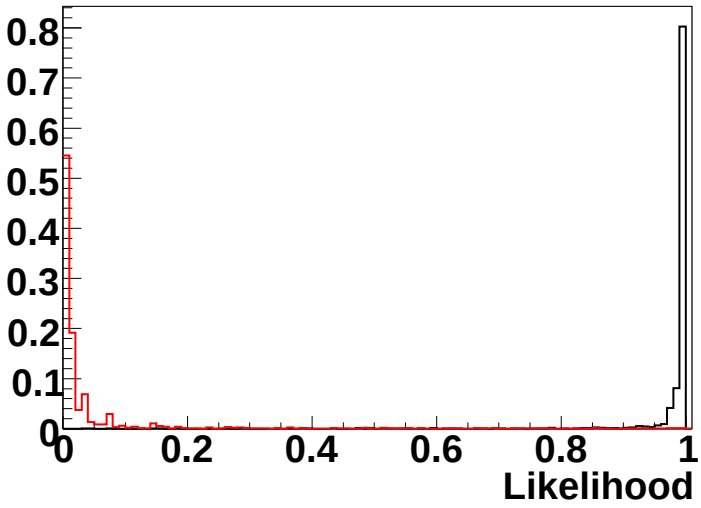

Figure 6.16: Likelihood discriminant output distributions for both simulated background (red line) and MC 100 GeV stau samples (black line).

We construct the expected limit as the object function upon which the cut on likelihood discriminant is optimized. Both the background rejection rate and the signal efficiency are derived for

every cut on likelihood discriminant function from 0 to 1 with a step size of 0.0001. The corresponding statistical uncertainties are also calculated as well as the expected number of background events with known luminosity. The CL95 Bayesian limit fitting code [65] with a flat prior is used to estimate both the expected limit and final observed limit. The expected limits are shown in Figs. 6.17 through 6.20 for cut value optimization.

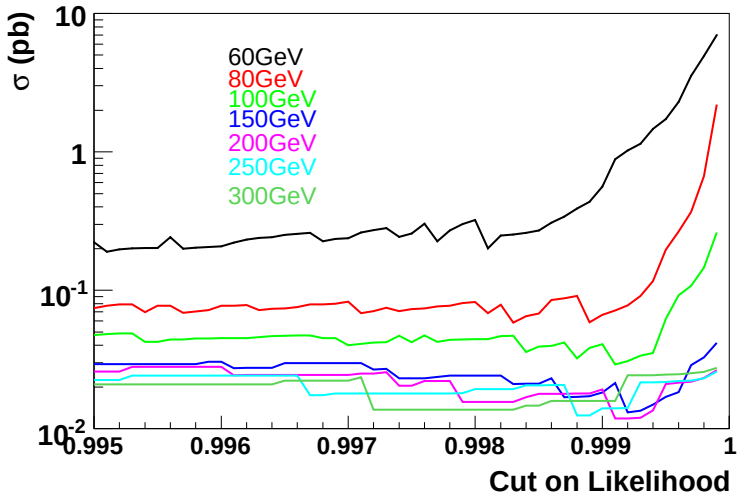

Figure 6.17: Expected limits for cut value optimization for every stau mass point.

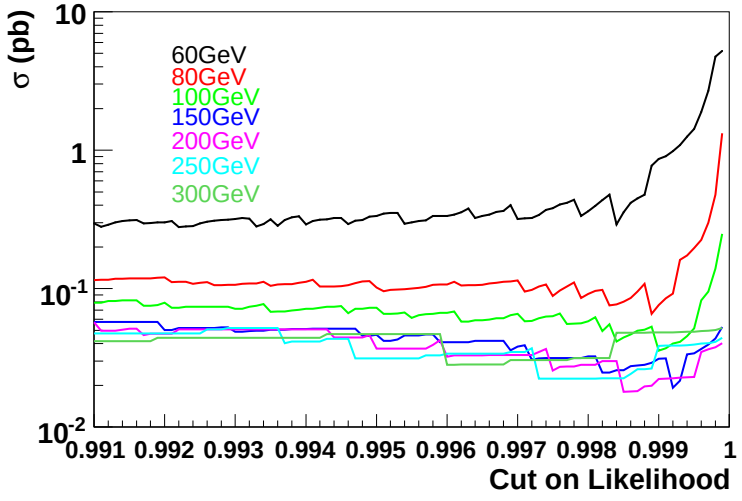

Figure 6.18: Expected limits for cut value optimization for every gaugino-like chargino mass point.

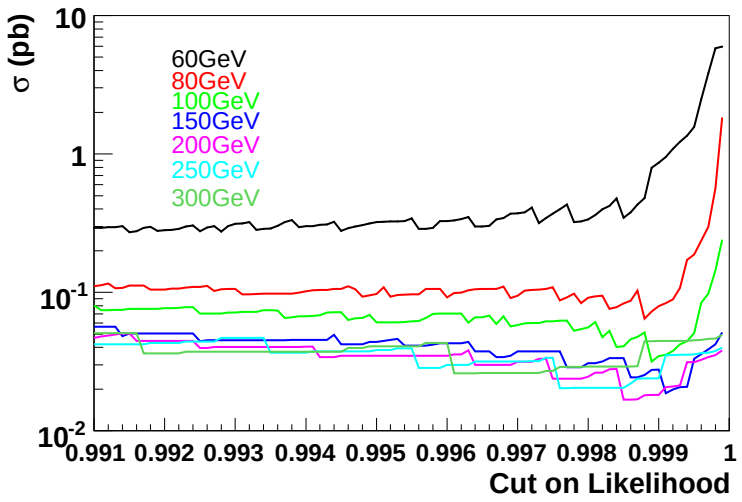

Figure 6.19: Expected limits for cut value optimization for every higgsino-like chargino mass point.

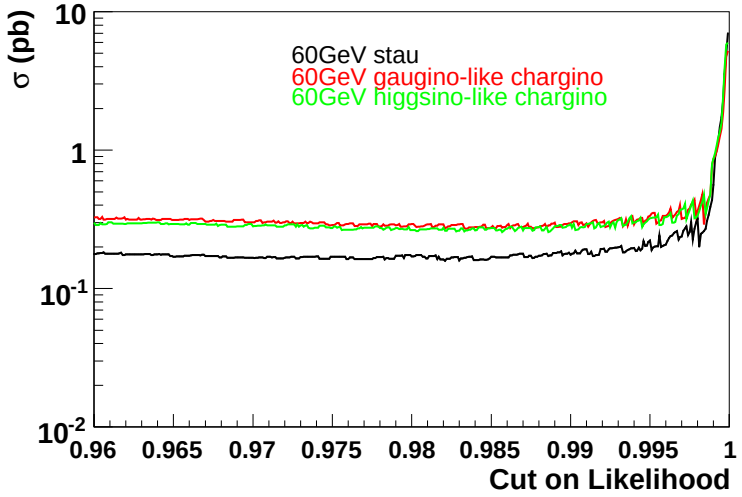

Figure 6.20: Expected limits for cut value optimization for 60 GeV mass point in three models.

The cut value on the likelihood discriminant is determined by finding the minimum expected limit. The luminosity uncertainties were taken into account for the expected limit during the optimization of the cut value on discriminant function. The optimized cut on the likelihood discriminant is shown in Table.6.4 .

Mass (GeV)	Stau	Gaugino-like Chargino	Higgsino-like Chargino
60	0.9838	0.9862	0.9886
80	0.9983	0.9988	0.9988
100	0.9991	0.9990	0.9989
150	0.9992	0.9992	0.9991
200	0.9991	0.9985	0.9985
250	0.9988	0.9973	0.9976
300	0.9972	0.9960	0.9961

Table 6.4: Optimized cut on likelihood discriminant function for every mass point in three models.

6.5 Systematic Uncertainties

The systematic uncertainties arise from different stages of the analysis. We divide them into two categories: systematic uncertainties with the background estimations and those related to the simulation of the signal Monte Carlo samples.

6.5.1 Systematic Uncertainties in Background Simulation

The background is estimated by selecting values randomly from the invariant mass and speed significance product distribution in data. The exact choice of data events used in these distributions could have a systematic effect on the estimated background. To estimate the effect, the criteria used to select the data events are varied. The background is re-estimated with the new random values from the new distributions and fed into the likelihood function. The effect on the number of predicted background events passing the final likelihood cut is taken as the systematic uncertainty.

The speed significance product distribution of the estimated background is obtained using the real data events which have invariant masses in the Z peak region (between 70 and 110 GeV) and passes all the selection criteria. Varying the mass window of the Z peak will affect the predicted number of estimated background events passing the final analysis cut on the likelihood outputs. The changes can be made in two directions: increasing the mass window to be between 60 and 130 GeV, or decreasing to between 80 and 100 GeV.

The invariant mass distribution of the estimated background events is simulated with the real data events which have negative speed significance values for both muons in the muon pair, but pass

all the other selection criteria. The selection on the speed significances of the muon candidates is loosened to require that one muon has negative speed significance while the other one is less than 1.

The changes on the data event selections are applied individually as only one selection criteria is changed at one time. For example, the selection on the events for the invariant mass simulation is kept unchanged when the criteria varies on those for the speed significance product, and vice verse. By isolating the changes on the selection criteria, the systematic uncertainties are studied independently. The difference on the predicted number of background events is normalized by the number before applying the changes on the selection criteria and is considered as the value of the systematic uncertainty. This is done for all the mass points in three models separately because of the different signal distributions.

Mass (GeV)	Uncertainty on Invariant Mass	Uncertainty on Significance Product	Background Uncertainty
60	5.5%	3.5%	6.5%
80	5.3%	5.3%	7.4%
100	9.1%	0.0%	9.1%
150	0.0%	9.1%	9.1%
200	0.0%	9.1%	9.1%
250	0.0%	18.2%	18.2%
300	8.3%	16.7%	18.6%

Table 6.5: Systematic uncertainties on estimated background for stau signals.

Mass (GeV)	Uncertainty on Invariant Mass	Uncertainty on Significance Product	Background Uncertainty
60	11.6%	5.8%	13.0%
80	0.0%	15.4%	15.4%
100	0.1%	20.0%	22.4%
150	18.2%	0.0%	18.2%
200	0.0%	8.3%	8.8%
250	0.0%	27.3%	27.3%
300	0.0%	9.1%	9.1%

Table 6.6: Systematic uncertainties on estimated background for gaugino-like chargino signals.

Mass (GeV)	Uncertainty on Invariant Mass	Uncertainty on Significance Product	Background Uncertainty
60	11.2%	2.6%	11.5%
80	16.7%	8.3%	18.6%
100	25.0%	8.3%	26.4%
150	20.0%	20.0%	28.3%
200	16.7%	16.7%	23.6%
250	0.0%	9.1%	9.1%
300	18.2%	9.1%	20.3%

Table 6.7: Systematic uncertainties on estimated background for higgsino-like chargino signals.

The systematic uncertainties on the predicted background events are summarized in Table 6.5, Table 6.6 and Table 6.7 for every mass point in all different signal models, respectively.

6.5.2 Systematic Uncertainties in Signal Simulation

The main sources for the systematic uncertainties of the signal acceptance are: the uncertainties in the object identification efficiencies, trigger efficiencies, Monte Carlo simulation normalizations, and the uncertainties related to the choice of PDF [66].

There is systematic uncertainty on the muon ID efficiency correction factors. The study was done in [48] and the summarized systematic uncertainty is 0.7%. This is included in the signal systematic uncertainties.

The Monte Carlo signal samples are generated without additional minimum bias overlay events. Since this may affect the signal acceptance, 10 K 100 GeV stau samples are produced especially with one minimum bias event overlayed on each event. The difference between the signal acceptances with and without the minimum bias overlay events is normalized and counted as the systematic uncertainty. The uncertainty on the signal acceptance is found to be less than 0.0002.

The timing smearing of the MC samples, based on the $Z \rightarrow \mu\mu$ data, is not perfect. In particular, the MC fits the timing distributions excellently in the central peak, but is too low in the tails, as seen in Section 5.3.2. An inperfect timing smearing will affect the signal acceptance. To explore this effect, we smeared the signal samples using the timing distributions of the tight muons in $W \rightarrow \mu\nu$ events rather than by the distributions from $Z \rightarrow \mu\mu$ data. Figure 6.21 shows the time distribution of $Z \rightarrow \mu\mu$ events in top/side C-layer using the $W \rightarrow \mu\nu$ sample timing distributions. The MC

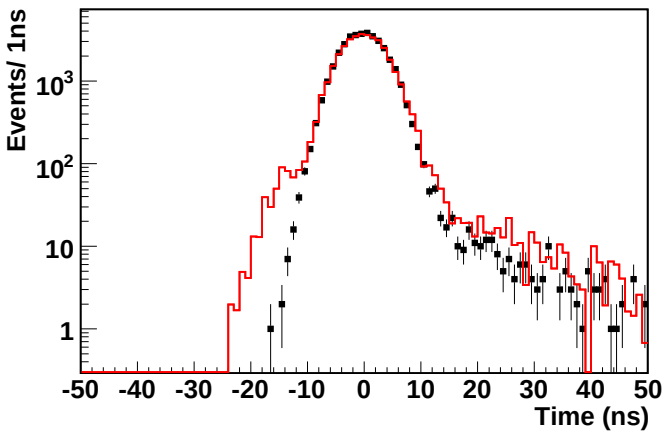

Figure 6.21: Timing smearing comparison plot in central C-layer muon region for Z$\mu\mu$ events in real data (black points with errors) and MC samples (red line) for side/top region (top) scintillation counters. The histograms in the plots are normalized to have the same number of events.

using $W \rightarrow \mu\nu$ timing distributions gives tails that are too large rather than too small as in Figs. 5.6 to 5.9. The difference between the signal acceptances derived from the different timing smearings is considered as a systematic uncertainty on the signals. The result is summarized and shown in Table 6.8.

Mass (GeV)	Stau Uncertainty	Gaugino-like Chargino Uncertainty	Higgsino-like Chargino Uncertainty
60	8.2%	11.6%	12.2%
80	12.0%	12.7%	13.4%
100	6.8%	13.2%	9.4%
150	9.8%	8.4%	8.6%
200	6.2%	7.6%	8.7%
250	6.6%	6.1%	8.3%
300	8.0%	7.7%	8.2%

Table 6.8: The timing smearing uncertainty on signal acceptance for all mass points in three models.

The muon timing trigger gate effects on the signal samples have been studied in Section 5.3.3. The corresponding trigger gate efficiency is defined as the number of events with both two muons inside the trigger gate divided by the total number of all events. The analysis is conducted on the

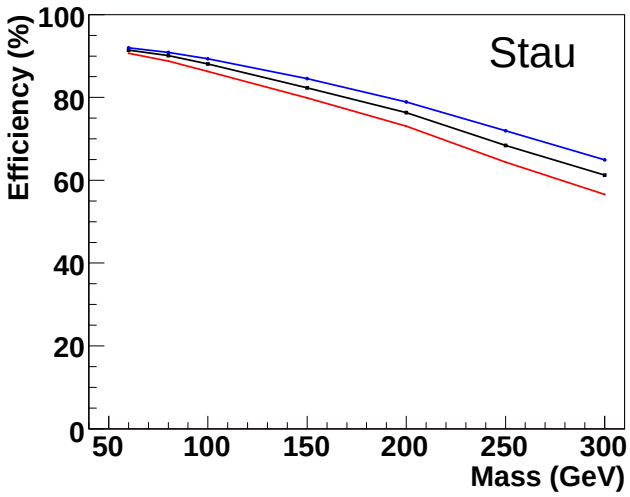

Figure 6.22: Trigger gate efficiency plots for all stau mass points. The black is for the correct trigger gate width; the red is for the trigger gate width narrowed by 2 ns; the blue is for the trigger gate width enlarged by 2 ns.

effects arising from varying the gate width because the width of the trigger timing gate determines the acceptance of the signal events.

The accuracy of the L1 Muon trigger gate width is of the order of 1 ns. This means that in the same layer and octant, the trigger gate width could be different from counter to counter; but the difference between counters should be within 1 ns. The worst scenario which leads to the biggest effect on the signal acceptance would be that all the counters have the half trigger gate width shrink 1 ns at the same time or the total width decrease by 2 ns. The studies were performed with the worst scenario implemented on all the signal samples with all masses in three models. The difference of the relative signal acceptances after the likelihood cut between the narrowed trigger gates and the normal trigger gates is considered as the systematic uncertainty of the trigger gate.

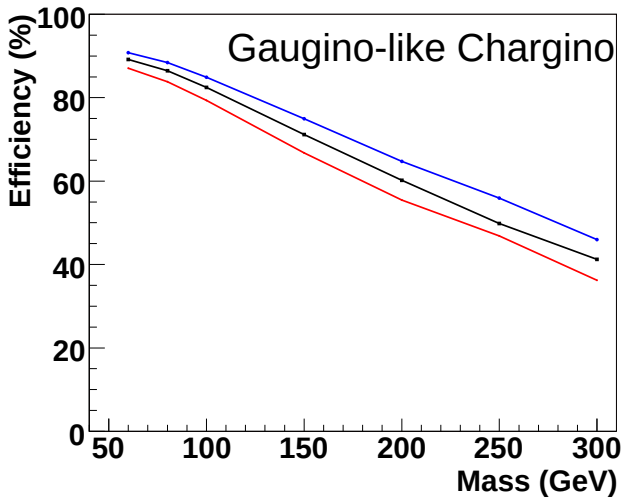

Figure 6.23: Trigger gate efficiency plots for all gaugino-like chargino mass points. The black is for the correct trigger gate width; the red is for the trigger gate width narrowed by 2 ns; the blue is for the trigger gate width enlarged by 2 ns.

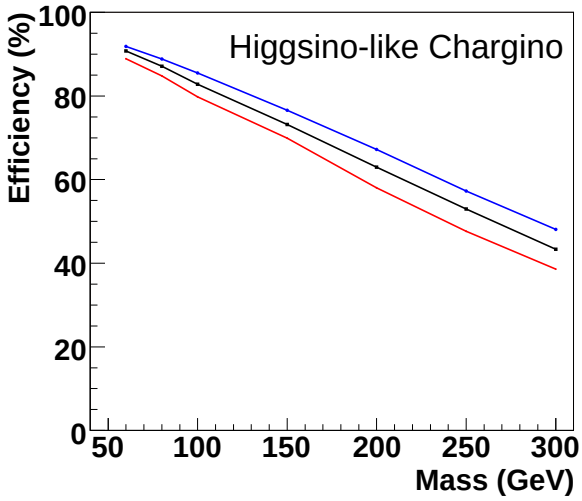

Figure 6.24: Trigger gate efficiency plots for all higgsino-like chargino mass points. The black is for the correct trigger gate width; the red is for the trigger gate width narrowed by 2 ns; the blue is for the trigger gate width enlarged by 2 ns.

Figs. 6.22 through 6.24 compared the trigger gate efficiency for all the mass points in the three models. The uncertainties are normalized by the acceptances with the normal trigger gates and listed in Table 6.9.

Mass (GeV)	Stau (%)	Gaugino-like Chargino (%)	Higgsino-like Chargino(%)
60	0.6	4.5	3.3
80	1.5	5.5	5.3
100	2.8	4.7	5.5
150	3.4	7.5	6.8
200	4.9	8.5	8.6
250	6.6	10.3	10.7
300	8.0	12.5	11.6

Table 6.9: Relative systematic uncertainties in the signal acceptance from the L1 muon trigger gate width uncertainty determined from the MC signal samples.

Based on Table 6.9, we observe that the systematic uncertainties increase steadily with increasing particle mass in all three models. Since there will be more particles moving slowly and having larger time-of-flight with higher particle mass, shrinking the gate width will have a larger effect at high mass points.

The choice of parton distribution function (PDF), which is used to generate the signal samples, can influence the signal acceptance as well. The PDF influences the momentum distribution of the generated signal sample, to which the speed distribution of the signal sample is directly related. The size of the effect is estimated by using the CTEQ6.1M error PDFs. The CAFe package "caf_pdfreweight" (v00-00-03) is used to re-weight the MC events based on the generator level particle information and the error PDFs [66]. The PDF uncertainties for all mass points in the three models are listed in Table 6.10 .

6.6 Results

There are 44,550 events in data passing the first 12 cuts and 15,450 events passing the 13th cut (both particles with positive speed significance). The signal acceptance, background prediction and number of observed events are summarized in Table 6.11 for staus, Table 6.12 for gaugino-like charginos and Table 6.13 for higgsino-like charginos, respectively. The statistical uncertainty on the simulated background is estimated using the procedure stated in [67]. The numbers of the observed events agree well with the predicted background events in most cases.

Mass (GeV)	Stau	Gaugino-like Chargino	Higgsino-like Chargino
60	$+0.4$	$+0.7$	$+0.6$
	-0.3	-0.6	-0.6
80	$+0.12$	$+0.5$	$+0.5$
	-0.2	-0.5	-0.5
100	$+0.1$	$+0.5$	$+0.4$
	-0.1	-0.5	-0.5
150	$+0.2$	$+0.5$	$+0.5$
	-0.3	-0.8	-0.8
200	$+0.4$	$+1.0$	$+0.9$
	-0.6	-1.3	-1.2
250	$+0.8$	$+1.6$	$+1.5$
	-0.9	-1.9	-1.7
300	$+1.4$	$+2.3$	$+2.2$
	-1.5	-2.7	-2.4

Table 6.10: The systematic uncertainty (%) estimated from the PDF for all mass points in three models

Mass (GeV)	Signal Acceptance	Predicted Background	Observed Events
60	$0.0635 \pm 0.0011 \pm 0.0052$	$30.9 \pm 2.2 \pm 1.7$	38
80	$0.0379 \pm 0.0009 \pm 0.0046$	$2.6 \pm 0.6 \pm 0.4$	1
100	$0.0556 \pm 0.0011 \pm 0.0041$	$1.6 \pm 0.5 \pm 0.3$	1
150	$0.1230 \pm 0.0016 \pm 0.0127$	$1.7 \pm 0.5 \pm 0.2$	1
200	$0.1394 \pm 0.0017 \pm 0.0111$	$1.7 \pm 0.5 \pm 0.5$	1
250	$0.1331 \pm 0.0016 \pm 0.0125$	$1.7 \pm 0.5 \pm 0.3$	1
300	$0.1171 \pm 0.0015 \pm 0.0134$	$1.9 \pm 0.5 \pm 0.2$	2

Table 6.11: The signal Acceptance, predicted number of background events and number of observed events for stau search as a function of the stau mass. The first uncertainty is statistical and the second is systematic.

Mass (GeV)	Signal Acceptance	Predicted Background	Observed Events
60	$0.0321 \pm 0.0008 \pm 0.0026$	$23.6 \pm 1.9 \pm 1.4$	24
80	$0.0244 \pm 0.0007 \pm 0.0030$	$1.9 \pm 0.5 \pm 0.3$	1
100	$0.0463 \pm 0.0010 \pm 0.0035$	$1.6 \pm 0.5 \pm 0.3$	1
150	$0.0851 \pm 0.0013 \pm 0.0088$	$1.2 \pm 0.4 \pm 0.1$	1
200	$0.0889 \pm 0.0013 \pm 0.0071$	$1.9 \pm 0.5 \pm 0.0$	1
250	$0.0740 \pm 0.0012 \pm 0.0070$	$1.7 \pm 0.5 \pm 0.3$	1
300	$0.0588 \pm 0.0011 \pm 0.0068$	$1.7 \pm 0.5 \pm 0.1$	2

Table 6.12: The signal Acceptance, predicted number of background events and number of observed events for gaugino-like chargino search as a function of the chargino mass. The first uncertainty is statistical and the second is systematic.

Mass (GeV)	Signal Acceptance	Predicted Background	Observed Events
60	$0.0292 \pm 0.0008 \pm 0.0024$	$17.9 \pm 1.7 \pm 1.1$	21
80	$0.0237 \pm 0.0007 \pm 0.0029$	$1.6 \pm 0.5 \pm 0.3$	1
100	$0.0494 \pm 0.0010 \pm 0.0037$	$1.6 \pm 0.5 \pm 0.3$	1
150	$0.0891 \pm 0.0013 \pm 0.0092$	$1.4 \pm 0.5 \pm 0.1$	1
200	$0.0956 \pm 0.0014 \pm 0.0076$	$1.9 \pm 0.5 \pm 0.0$	1
250	$0.0813 \pm 0.0013 \pm 0.0076$	$1.7 \pm 0.5 \pm 0.3$	1
300	$0.0636 \pm 0.0011 \pm 0.0073$	$1.7 \pm 0.5 \pm 0.1$	1

Table 6.13: The signal Acceptance, predicted number of background events and number of observed events for higgsino-like chargino search as a function of the chargino mass. The first uncertainty is statistical and the second is systematic.

Since the number of observed events is consistent with the predicted background, a 95% confidence level (C.L.) limit on the pair-production cross section is set for each mass point in the three models . An uncertainty of 6.1% on the luminosity is also included in the cross-section limit calculation. Both the systematic and statistical uncertainties are included for the final expected limits and the 95% C.L. limit with the same CL95 Bayesian limit fitting code.

The masses and the couplings in the signal models are computed by SOFTSUSY [68] and the next-to-leading order (NLO) cross section is calculated with PROSPINO[69]. The uncertainty on the cross section is estimated using the prescription in Ref. [66]. The scale uncertainty is estimated by varying the factorization and renormalization scales between Q/2 and 2Q. The PDF uncertainty is estimated using the 40 CTEQ6.1M error PDFs. The renormalization and factorization scale uncertainty and the PDF uncertainty are added in quadrature to obtain the total uncertainty on the signal cross sections.

Mass (GeV)	NLO cross section (pb)	95% CL limit (pb)	Expected Limit (pb)
60	0.069	0.31	0.20
80	0.026	0.10	0.12
100	0.011	0.07	0.07
150	0.0020	0.03	0.03
200	0.00042	0.03	0.03
250	0.00010	0.04	0.03
300	0.000026	0.04	0.03

Table 6.14: Limits and NLO cross section for pair-produced staus.

Mass (GeV)	NLO cross section (pb)	95% CL limit (pb)	Expected Limit (pb)
60	12.900	0.42	0.39
80	3.290	0.16	0.16
100	1.300	0.09	0.09
150	0.221	0.05	0.05
200	0.0509	0.04	0.04
250	0.0131	0.05	0.05
300	0.0035	0.09	0.07

Table 6.15: Limits and NLO cross section for pair-produced gaugino-like charginos.

Mass (GeV)	NLO cross section (pb)	95% CL limit (pb)	Expected Limit (pb)
60	3.000	0.51	0.40
80	0.895	0.17	0.17
100	0.389	0.08	0.08
150	0.0749	0.04	0.04
200	0.0188	0.04	0.04
250	0.0051	0.05	0.05
300	0.0015	0.06	0.06

Table 6.16: Limits and NLO cross section for pair-produced higgsino-like charginos.

The limits and cross sections are summarized in Table 6.14 for stau, Table 6.12 for gaugino-like charginos, and Table 6.16 for higgsino-like charginos. The calculated expected and observed limits, the NLO cross sections, and the corresponding uncertainties on the cross sections are shown in Figs. 6.25 through 6.27 for varying stable stau and chargino masses, respectively.

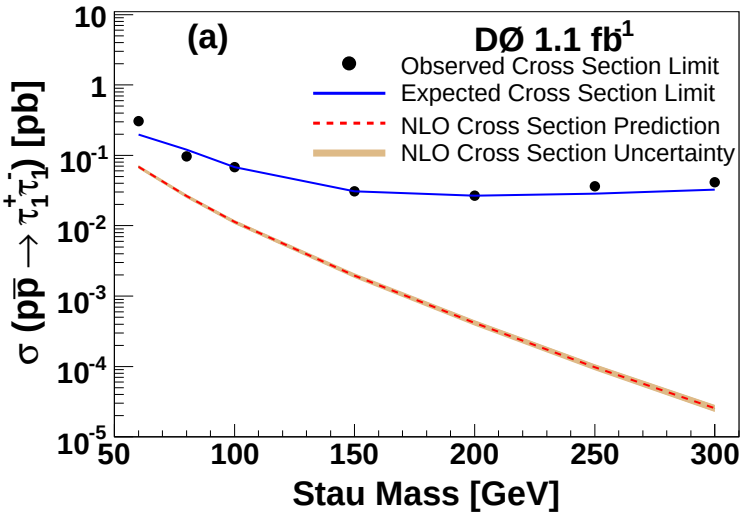

Figure 6.25: 95% CL cross-section limits for staus.

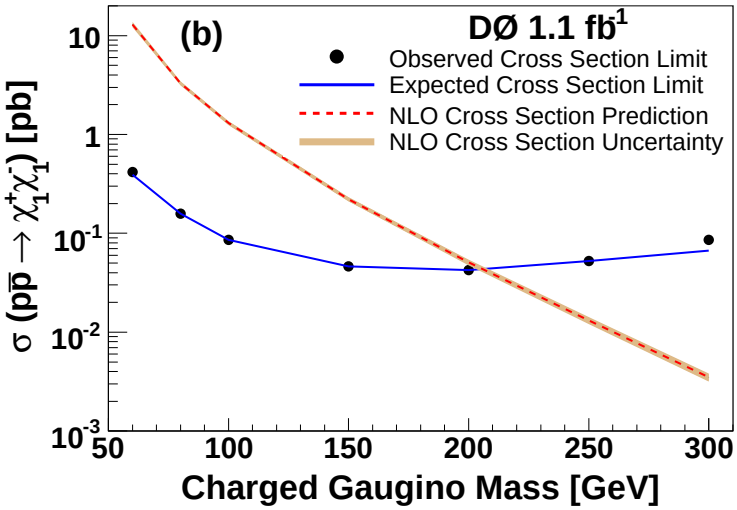

Figure 6.26: 95% CL cross-section limits for gaugino-like charginos.

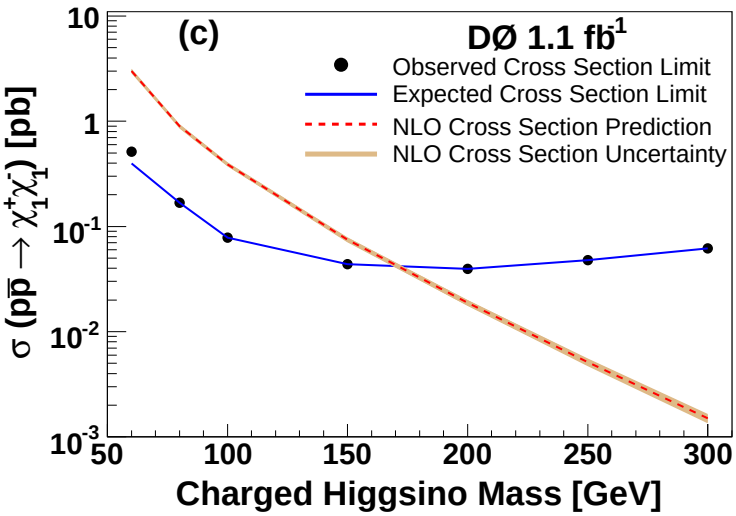

Figure 6.27: 95% CL cross-section limits for higgsino-like charginos.

Using the nominal (nominal -1σ) values of the NLO cross sections with the intersections of the calculated limits, the lower mass limits can be set on pair-produced stable gaugino-like and higgsino-like charginos. The intersections with the lower uncertainty band, the central cross section value, and the upper uncertainty band result in mass limits of 204 GeV, 206 GeV and 208 GeV for gaugino-like charginos and 169 GeV, 171 GeV and 173 GeV for higgsino-like charginos.

Chapter 7

Summary

7.1 Conclusions

A search for charged massive stable particles has been performed with the DØ detector using 1.1 fb^{-1} of data. The speed of the particle has been calculated based on the time-of-flight and position information in the muon system. The present research is limited to direct pair-production of the charged massive long-lived particles. We do not consider CMSPs that result from the cascade decays of heavier particles. In this analysis, the exact values of the model parameters of the entire supersymmetric particle mass spectrum, relevant for cascade decays, are not important.

We found no evidence of the signal. 95% CL cross-section upper limits have been set on the pair-productions of the stable scaler tau lepton, the gaugino-like charginos, and the higgsino-like charginos. The upper cross section limits vary from 0.31 pb to 0.04 pb, for stau masses in the range between 60 GeV and 300 GeV. We use the nominal value of the theoretical cross section to set limits on the mass of the pair produced charginos. We exclude the pair-produced stable gaugino-like charginos with mass below 206 GeV, and higgsino-like charginos below 171 GeV, respectively. Although the present sensitivity is insufficient to test the model of the pair produced stable staus, we do set cross section limits which can be applied to the pair production of any charged massive stable particle candidates with similar kinematics.

These are the most restrictive limits to the present on the cross sections for CMSPs and the first published from the Tevatron Collider Run II. The manuscript has been published by Physical Review Letters in April 2009 [70] and is available at arXiv as [71].

Bibliography

[1] D. Griffiths, *Introduction to Elementary Particles*. New York, USA: Wiley, 1987.

[2] S. Novaes, "Standard model: An introduction." hep-ph/0001283.

[3] S. Glashow, "Partial symmetries of weak interactions," vol. 22, 1961.

[4] S. Weinberg *Phys. Lett.*, vol. 12, 1967.

[5] A. Salam, *Elementary Particle Physics*. N. Svartholm (Almqvist & Wiksell), 1968.

[6] S. Martin, "A supersymmetry primer." hep-ph/9709356.

[7] T. Kaluza *Preus. Acad. Wiss.*, vol. K1, 1921.

[8] O. Klein *Z. Phys.*, vol. 37, 1926.

[9] N. Arkani-Hamed, S. Dimopoulos, and G. Dvali, "The hierarchy problem and new dimensions at a millimeter," *Phys. Lett. B*, vol. 429, 1998. hep-ph/9803315.

[10] L. Randall and R. Sundrum, "A large mass hierarchy from a small extra dimension," *Phys. Rev. Lett.*, vol. 83, 1999. hep-th/9906064.

[11] `http://www.physics.washington.edu/users/strasslr/hv/hv.htm`.

[12] M. Strassler and K. Zurek, "Echoes of a hidden valley at hadron collider." hep-ph/0604261.

[13] M. Strassler and K. Zurek, "Discovering the higgs through highly-displaced vertices." hep-ph/0605193.

[14] G. F. Giudice and R. Rattazzi *Phys. Rep.*, vol. 322, 1999.

[15] M. Dine and A. Nelson *Phys. Rev D*, vol. 48, 1993.

[16] M. Dine, A. Nelson, Y. Nir, and Y. Shirman *Phys. Rev. D*, vol. 53, 1996.

[17] B. C. Allanach, M. Battaglia, G. A. Blair, M. Carena, A. De Roeck, A. Dedes, A. Djouadi, D. Gerdes, N. Ghodbane, J. Gunion, H. E. Haber, T. Han, S. Heinemeyer, J. L. Hewett, I. Hinchliffe, J. Kalinowski, H. E. Logan, S. P. Martin, H. U. Martyn, K. T. Matchev, S. Moretti, F. Moortgat, G. Moortgat-Pick, S. Mrenna, U. Nauenberg, Y. Okada, K. A. Olive, W. Porod, M. Schmitt, S. Su, C. E. M. Wagner, G. Weiglein, J. Wells, G. W. Wilson, and P. Zerwas, "The snowmass points and slopes: Benchmarks for susy searches," *European Physical Journal C*, vol. 25, p. 113, 2002.

[18] S. Martin, S. Morettim, J. Qian, and G. Wilson, "Direct investigations of supersymmetry: subgroup summary report." FERMILAB-CONF-01-371-T.

[19] C. Chen, M. Drees, and J. Gunion *Phys. Rev. D*, vol. 55, 1997.

[20] J. Gunion and S. Mrenna *Phys. Rev. D*, vol. 62, 2000.

[21] M. Fairbairn, A. Kraan, D. Milstead, T. Sjostrand, P. Skands, and T. Sloan, "Stable massive particles at colliders." hep-ph/0611040.

[22] C. Amsler and et. al., "Review of particle physics," *Physics Letters B*, vol. 667, 2008. `http://pdg.lbl.gov`.

[23] M. Byrne, C. Kolda, and P. Regan *Phys. Rev. D*, vol. 66, 2002.

[24] P. Smith and et. al. *Nucl. Phys. B*, vol. 206, 1982.

[25] ALEPH, DELPHI, L3, and O. collaborations, "note lepsusywg/02-09.2." `http://lepsusy.web.cern.ch/lepsusy/www/gmsb_summer02/lepgmsb.html`.

[26] ALEPH, DELPHI, L3, and O. collaborations, "note lepsusywg/02-05.1." `http://lepsusy.web.cern.ch/lepsusy/www/stable_summer02/stable_208.html`.

[27] D. Acosta and et. al. *Phys. Rev. Lett.*, vol. 90, 2003.

[28] M. Eads and D. Hedin, "A search for charged massive stable particles at dø." DØ internal Note #4747.

[29] http://www.fnal.gov/.

[30] http://www-bd.fnal.gov/runII/index.html.

[31] http://www-bdnew.fnal.gov/operations/rookie_books/rbooks.html.

[32] D. collaborations, S. Abachi, and et. al., "The DØ detector," *Nucl. Instrum. Methods Phys. Res. Sect. A*, vol. 338, 1994.

[33] D. collaborations, V. Abazov, and et. al., "The upgraded DØ detector," *Nucl. Instrum. Methods Phys. Res. Sect. A*, vol. 565, 2006.

[34] http://keyhole.web.cern.ch/keyhole/detectors/Delphi.html.

[35] V. Abazov and et. al., "The muon system of the Run II DØ detector," *Nucl. Instrum. Methods Phys. Res. Sect. A*, vol. 552, 2005.

[36] R. Angstadt and et. al., "The DZERO Level 3 data acquisition system," *IEEE Transactions on Nuclear Science*, vol. 51, 2004.

[37] A. Garcia-Bellido and et. al., "The DZERO Level 3 DAQ system: Operation and upgrades," *proceeding of IEEE Real-Time Conference, 15th IEEE-NPSS*, 2007.

[38] A. Khanov, "HTF: histogramming method for finding tracks. the algorithm description.." DØ internal note #3778.

[39] G. Borissov, "Status of D0 Track Reconstruction." presented at All DØ meeting, Feb. 14, 2003.

[40] G. Borissov, "Ordering a Chaos or ... Technical Details of AA Tracking." presented at All DØ meeting, Feb. 28, 2003.

[41] A. Schwartzman and C. Tully, "Primary Vertex Reconstruction by Means of Adaptive Vertex Fitting." DØ internal note #4918.

[42] A. Kumar and et. al., "Electron Likelihood Study." DØ internal note #4769.

[43] "Comparison of H-Matrices for electron identification in D0 Run II." DØ internal note #3745.

[44] G. Blazey and et. al., "Run II Jet Physics." DØ internal note #3750.

[45] A. Harel, "Jet ID Optimization." DØ internal note #4919, Version 1.1.

[46] J. Group, "Jet Energy Scale Determination at D0 Run II." DØ internal note #5382.

[47] http://www-d0.fnal.gov/phys_id/jes/public_RunIIa.

[48] P. Calfayan, T. Gadfort, G. Hesketch, V. Lesne, M. Owen, R. Strohmer, V. Sharyy, and B. Tuchming, "Muon identification certification for p17 data." DØ internal note #5157.

[49] http://www-d0.fnal.gov/computing/algorithms/muon/muon_algo.html.

[50] http://www-d0.fnal.gov/Run2Physics/cs/caf/.

[51] http://root.cern.ch/.

[52] R. Hauser, "Common analysis format tutorial," 2005. DØ collaboration week, June 16, 2005.

[53] http://www-d0.fnal.gov/Run2Physis/cs/caf/Packages.200902.html.

[54] http://www-d0.fnal.gov/Run2Physics/cs/skimming/fixPass2p170903.html.

[55] https://plone4.fnal.gov/P1/D0Wiki/physics/top/howto-lumi.

[56] http://www.cplusplus.com/reference/.

[57] http://en.wikipedia.org/wiki/C\%2B\%2B_standard_library.

[58] T. Sjostrand, L. Lonnblad, S. Mrenna, and P. Skands, "Pythia 6.323." hep-ph/0308153.

[59] R. Brun and et al., 1993. CERN Program Library Long Writeup W5013.

[60] M. Arthaud, F. Deliot, B. Tuchming, V. Sharyy, and D. Vilanova, "Muon momentum oversmearing for p17 data." DØ interal note #5444.

[61] E. Nurse and P. Telford, "Measurement of cross section times branching ratio for $z \rightarrow \mu\mu$ in ppbar collision at 1.96 tev." DØ internal note #4689.

[62] F. Deliot and B. Tuchming, "muo_cert package." DØ internal note #XXXX.

[63] A. Bellavance, K. Harder, G. Hensel, G. Hesketh, N. Khalatyan, A. Lobodenko, D. Onoprienko, and H. Schellman, "Measurement of $p\bar{p} \rightarrow \mu\mu$ yield in the z mass region for dø run iia data." DØ internal Note #5269.

[64] R. Duda, P. Hart, and D. Stork.

[65] V. Buescher, J.-F. Grivaz, J. Hobbs, A. Kharchilava, G. Landsberg, J. Linnemann, H. Prosper, and S. Soldner-Remhold. DØ internal Note #4629.

[66] V. Buscher, J.-F. Grivaz, T. Nunnemann, and M. Wobisch. DØ internal Note #4618.

[67] M. Paterno. DØ internal Note #2861.

[68] B. Allanach. hp-ph/0104145.

[69] W. Beenakker, M. Klasen, K. M, T. Plehn, M. Spira, and P. M. Zerwas *Phys. Rev. Lett.*, vol. 83, 1999.

[70] V. Abazov and D. collaboration, "Search for changed massive stable particles with the d0 detector," 2009.

[71] V. Abazov and D. collaboration, "Search for changed massive stable particles with the d0 detector," 2008. `http://arxiv.org/abs/0809.4472`.

[72] Y. Xie, "Daq shifter tutorial: Level3/daq," 2005. presented at Shifter Tutorial, April 26th, 2005.

[73] J. BackusMayes, "Daq shifter tutorial: Level3/daq," 2009. presented at Shifter Tutorial, January 27th, 2009.

[74] "L3daq what-to-do-when webpage." `http://www-d0online.fnal.gov/www/groups/l3daq/shifter/wtdw.html`.

[75] "problems.txt." http://www-d0online.fnal.gov/www/groups/daq/Problems.txt.

[76] D. Cutts and G. Landsberg, "Detection of long-lived particles in run ii with d0," 1999.

[77] http://root.cern.ch/root/html/TLimit.html.

Appendix A

Level 3 Data Acqusition System

The Level 3 data acquisition system (L3 DAQ) has been introduced in Section 3.2.8. The components of the system are classified into two categories, the hardware and the software [72, 73]. The single board computers (SBCs), computer farm nodes, the routing master, and the network serve as the hardware. The software consists of the programs running on the hardware: the L3 supervisor, the Routing Master and the event builder on the SBCs. There are also several monitoring programs written in the JAVA language: the monitor server code, daqAI, uMon, fuMon, and DAQ Dialog.

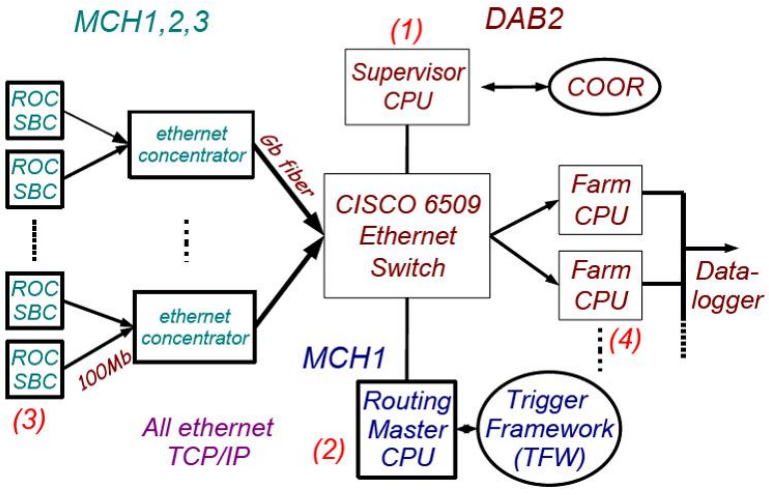

Figure A.1: Data flow chart for L3 DAQ system.

The working flow of the DAQ system is shown in Fig. 3.10 together with the trigger system at DØ. Figure A.1 is the data flow chart of the L3 DAQ system. The data chunk from the sub-detector systems are collected on SBCs. The Routing Master (RM) routes data chunks to the farm nodes via Ethernet. The L3 supervisor software communicates with COOR, sends run information to the RM, groups farm nodes for different running purposes and sends trigger programming information to them.

A.1 Hardware

As mentioned above, the single board computers (SBCs), computer farm nodes, and the Routing Master are the main components of the hardware.

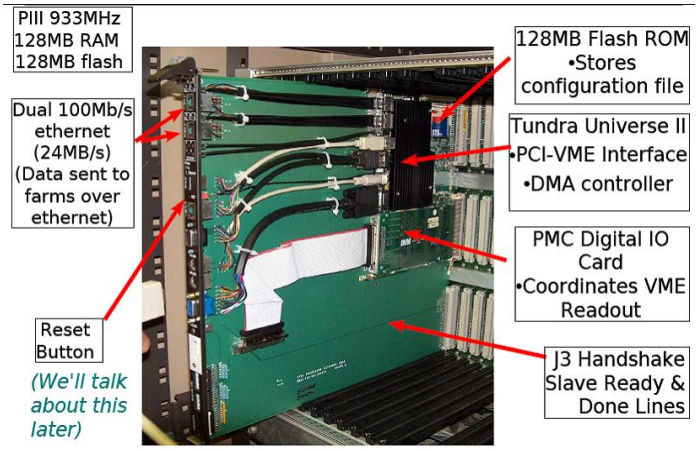

Figure A.2: Picture of a typical working single board computer (SBC) mounted in the adapter board.

In Fig. A.2, a typical working SBC is shown mounted in the adapter board. The SBC has a Pentium III processor with both a 128 MB RAM and a 128 MB compact flash card. Each SBC has two Ethernet ports, that are configured in one the three different ways in the running SBCs. Fifty SBCs, with average data loads less than 12 KB per event fragment, have just one single 100-Mb Ethernet interface configured. There are thirteen crates, each with typical data loads above 12 KB, operating with two 100-Mb Ethernet interfaces. Three crates, with even larger fragment sizes around or beyond 20 KB, have the Gb fiber connections directly to the main Cisco switch. The Gb cards are installed on those three SBCs.

The Routing Master (RM) is housed in a special SBC, and has been upgraded from the usual VMIVME 7750 to a VMIVME 7805 with a faster Pentium 4M processor running at 1.7 GHz. Now the RM decisions are made within 1 ms. The CPU will be running at its maximum only when the input rate is 1.4 KHz, however, the maximum design input rate for the L3DAQ is only 1 KHz.

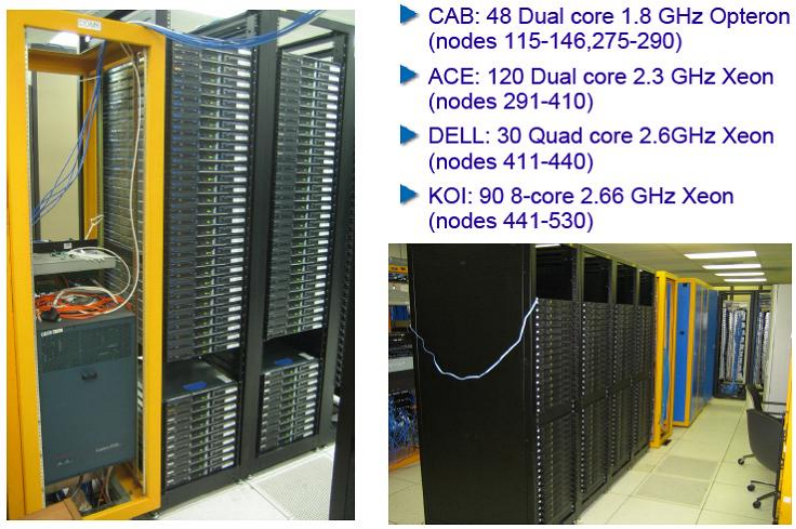

Figure A.3: Picture of the running farm nodes.

The L3 farm has grown from the original 82 computers in 2004 to the current 288 computers. The increased number of nodes is necessary to cooperate with the increased instant luminosity. There are four groups of farm nodes which are divided by the computer types. Before being included in the farm, new nodes are installed with the operating systems and have the burn-in test run on them. The system installation and the burn-in test originally were carried by our own L3 DAQ group. After 2006, the tasks were transferred to the Fermilab Computing Divisions for better efficiency. Due to the limited sources (electricity, cooling system, floor supporting, and the physical space) at DØ, we only keep the latest farm nodes in the farm. The older farm nodes are removed from the farm, although they are still functional.

A.2 Software

The L3 DAQ system is designed so that multiple runs are allowed to operate simultaneously. The run taking real-collision data is called “primary run”, which has the highest priority. In primary runs, all the SBCs reading from the working detector crates should be included so that the information of the event is complete. Between stores, some sub-detector systems, like the calorimeter, need to collect data for calibration purposes, for which only part of the SBCs and several farm nodes are needed. Such runs are called “secondary runs”, which can be performed at the same time when other SBCs and farm nodes are used to take zero-bias events. Sometimes, other sub-detector systems may also need to test and develop their software, which requires a stand-alone SBC in the special test-stand and maybe also a few farm nodes. This type of test run is also classified as a “secondary run”, and can even be performed during the routine operation in the store. The L3 supervisor takes the charge of configuring the necessary SBCs and associated farm nodes for different routine groups.

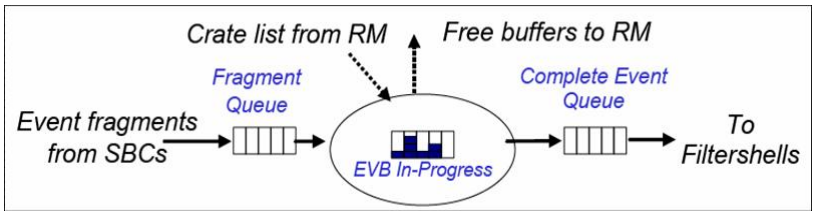

Figure A.4: Schematic illustration of the event builder program running on farm nodes.

These capabilities allowed us to conduct equipment upgrades. We have several SBCs configured specially in order to take the test type secondary runs. One SBC was set up for the SMT and STT system, and another one was set up for the L1 Muon system. There was one SBC setup on the first floor of the movable counting house and used when upgrading the L1 CALTRACK triggers. The SBCs for the L1 Muon system and the trigger upgrades were setup by me. We also keep one SBC in our own test-stand on the second floor of the fixed counting house. This special SBC serves for our normal SBC maintenance and development.

Farm nodes communicate with the RM, receiving the crate list from the RM and reporting back the number of their current available buffers. Once all the fragments for an event have arrived at the farm node, they are collated into a complete event by the event builder. Then the complete events

are queued in shared memory buffers for further processing by the L3 filter process. The L3 filter process also runs on the farm nodes, and checks whether the complete events fire the L3 triggers. Once the L3 triggers are fired, the event will be sent to the data-logger and recorded onto tapes at Feynman computing center. If no L3 triggers are fired, an event is discard. There are more than one filter shell running at each farm node, and the number of the filter processes has been optimized to increase the capacity for each type of node.

A.3 Monitoring

Monitoring programs are developed for better performance of the system, which check the system status at every moment. The monitoring processes are user friendly graphic interfaces and are built on the JAVA language. There are three main monitoring programs on the different hardware: one for all SBCs and the RM, one for all the farm nodes, and one for the L1 and L2 front-end electronics, which are the uMon, fuMon, and DAQ Dialog, respectively. Those graphic interfaces are normally displayed on the DAQ shifter's consoles, and they also can be viewed on other machines easily. We discuss them in detail separately.

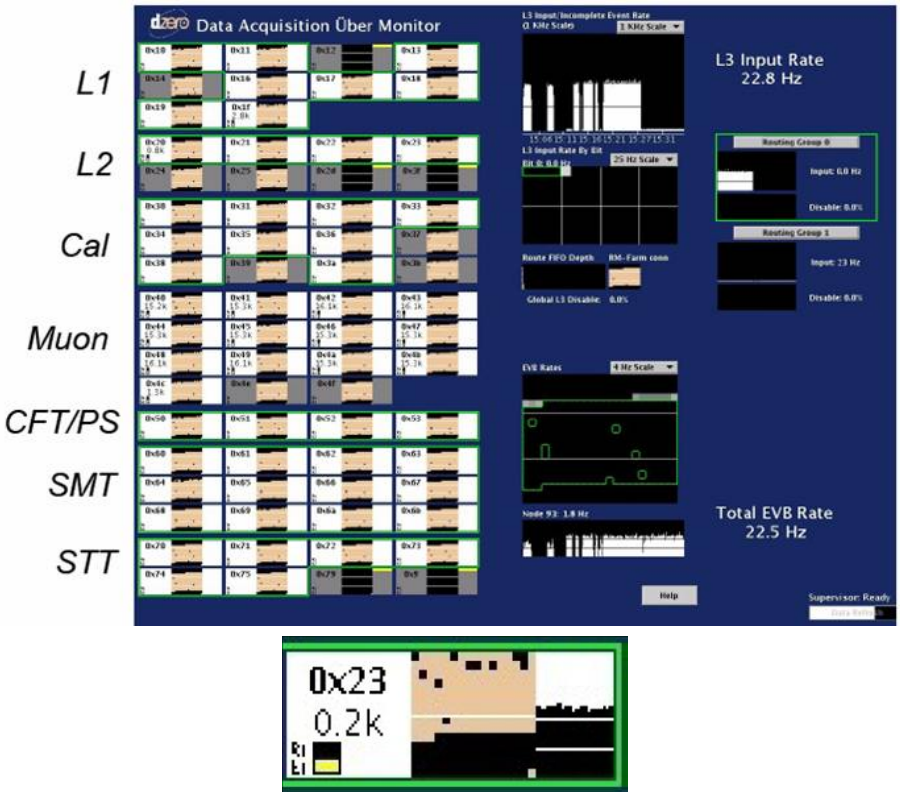

Figure A.5: Picture of the uMon monitoring graphic interface. Top is for all the SBCs and RM, and bottom is for each SBC.

Program "uMon" is designed for monitoring the running status of all the SBCs, the RM, and the L3 supervisor program. A picture of the graphic interface is shown in Fig A.5 (top). On the left side of the uMon interface, all the SBCs in the corresponding crates are grouped into seven subgroups, which are L1, L2, Calorimeter, Muon, CFT and PreShower, SMT, and STT. In the middle of the uMon interface, the input rate to L3 is displayed at the top, and below this is the display of the used trigger bits. Next are the smaller displays of the routing FIFO queue, the farm node and RM connections, and the global L3 disable rate. At the bottom of the middle column, the event build rate is shown in color for each farm node on the bigger readout, and by choosing a particular node, the event build rate can be viewed for the last five minutes updating every second in the smaller readout below. On the upper right side of the interface, different routing groups are listed with their own input rates and disable percentages on L3. On the right bottom, the total event builder rate is summed over the whole farm and the status of the supervisor is progressively displayed.

For every SBC in each crate, there is an icon with all the associated information as shown in the bottom of Fig. A.5. The icon can be divided into three areas: left, middle and right side. On the left side, the crate number in hex is listed at the top, then is the fragment transfer rate in bits. The two colored bars are the two queues running on the SBC. The black color stands for the routing queue with information from the RM, while the yellow one is the event fragment received. When the number in these two queues is mis-matched, the fragment for this event will be discarded and the background color for this crate will turn to red from the default white. The connections between each farm node and the SBC are shown in the middle of the icon. Beige means a good connection, while black means no connection. At the right bottom corner of this group is the connection with the RM. If the box is colored white, it means that the SBC has live connection with the RM. However, black means no connection with the RM. On the right side, the input rate to the SBC from the crate back-plane is updated every second.

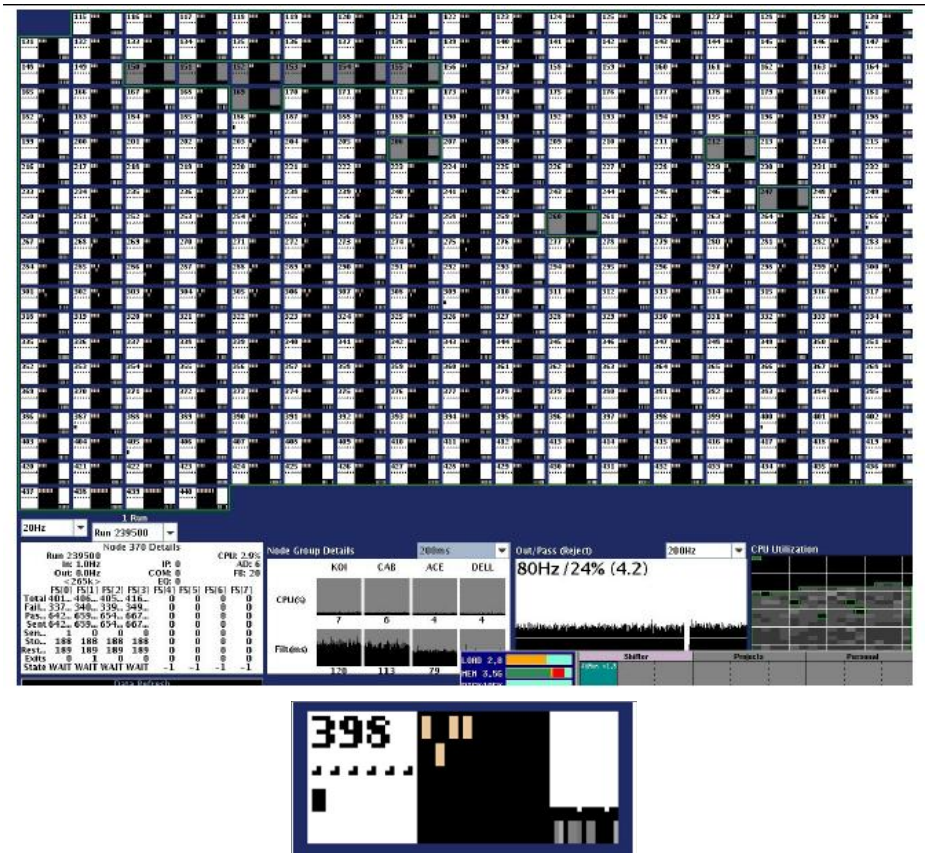

Figure A.6: Picture of fuMon monitoring graphic interface. Top is the picture for all the farm nodes, and bottom is the unit picture for each farm node.

Program “fuMon” is developed for monitoring the running status of all the farm nodes, their performance, and the status of the L3 filter shells, as shown at the top of Fig. A.6. All the running farm nodes are listed at the top of the display. The nodes in the same routing group are bordered with green lines. By choosing different routing groups when there are multiple runs, the nodes associated with that group will be inside the green lines. This can be done by clicking the button on the left side below the farm nodes and selecting the run. By clicking the individual icon for each farm node, detailed information of its performance will be displayed in the left bottom corner of the interface. The listed information includes the run number in which the farm node is included, the CPU usage, the input and output rate, and the filter shells, etc. The graphs to the right of the list are the CPU and filter shell performance, displaying the averages for the four farm node types. Moving further right, the output event rate is displayed summed over the whole L3 farm. In the right bottom corner, the CPU usage for each node is plotted again in a 2D gray scale histogram. This 2D plot gives another direct view of the handling of each farm node in different types.

The icon for each farm node is displayed in the bottom of Fig. A.6. Similar to the icon of the SBCs, it is also divided into three major regions. The left side includes the number of the farm node, which is the label index, the number of available free filter shells on the node, and a black bar showing whether there is filtered events in the queue to the next stage. In the middle, beige boxes stand for the event status. There are in total four possible statuses of the built event. They are waiting, filtering, flattening and sending, corresponding to rows top to bottom, respectively. White is the default background for each node, which means that the node is running smoothly. When the node is not active, the background color will be gray and may need to be examined. If the expected fragment from the SBC is missing, the farm node will show the red alert color. If the farm node is busy processing events, it will have a warning blue color. Those colors provide useful information for maintenance and development.

The DAQ DIALOG is a simple graphic interface, which monitors the front-end electronic status. This tool releases the front-end busy information at both the L1 and L2. When the front end read-out is too busy, the disable rate will rise up and the color of the crate will turn to red as an alert for the SBC crate.

A.4 Maintenance and Homepage

The maintenance work is carried by our group of L3 DAQ experts, including the work both on the hardware and the software development. The main goal is to keep the data taking process running healthily even at the current high instantaneous luminosity.

During the routine operation, there is a chance that some part of the system is mulfunctioning. Most simple problems will be taken care of by the daqAI program, while our "what-to-do-when..." web-page [74] provides additional details. The "problem.txt" [75] is another good resource place for both shifters and experts to identify similar symptoms and find the corresponding solutions. We also provide 24/7 on call expert coverage, and the help of the monitoring tools, the DAQ shifter can provide our on-call experts the symptoms clearly and easily. This enables us to solve the problems quickly during the stores.

Appendix B

Studies on the energy loss at DØ detector

The energy deposit of the particle in the DØ detector can be measured in several sub-detector systems. One is the Silicon Micro-strip Tracker (SMT) as part of the central tracking system, and another is the calorimeter. The Silicon Tracker Trigger (STT) is designed to identify collisions consistent with the production of the b-flavored particles. It is the Level2 (L2) processing system which takes the unsuppressed raw data from the SMT detector as its input. STT also takes input from the L1 central track trigger (CTT) based on the central fiber tracker (CFT) system. However, the energy deposited in the CFT is not measured, and therefore cannot be used for triggering or event selection. In the STT system, the interesting events can be identified initially in 100-200 μs for later study and triggering. The dE/dx value is derived from the pulse height values of the SMT hits used in the track fit, and is stored in the data output.

There are three trigger bits which are not assigned in the STT system. The capabilities are preserved for adding selection criteria on the energy deposit in the SMT read-out. The possible Level 2 dE/dx trigger would be a good means to classify the slow moving particles from the light speed ones, independent of other criteria such as the TOF or track isolation [76]. Studies have been carried out investigating the candidate L2 dE/dx trigger. Since there are at most 3 trigger bits available, the value(s) derived from dE/dx have to be in a range [0, 7].

A full simulation of the STT was originally designed to be used in the design phase of the STT for algorithm testing. It can also be used for different signal and background simulations to test the selection efficiency for the trigger criteria. The full DØ trigger simulation (trigsim) is a single program providing a standard framework for including the individual trigger element code. In this

framework, the data format transferred between the trigger elements is specified; the time ordering of the trigger levels and the data transfers are simulated. The simulator code is written in C++, and can be run on both real DØ data and the simulation samples. Furthermore, it can be run either as part of the full DØ trigger simulation or in a stand-alone mode. The internal structure mimics the sextant and sector part of the actual STT. The output data can be created in the format as those sent to the L2 and L3 online.

A study on dE/dx in the SMTwas undertaken with both $Z \rightarrow \mu\mu$ real data as background and the simulated CMSP signal samples in the STT trigsim framework. The real data samples are in their raw data format without the reconstruction process.

The energy loss is represented by the number of ADC counts in each layer of the SMT in the range [0, 255]. This 8-bit integer number is converted to an integer number for simplicity. Figure B.1 is the total energy deposit measured in ADC counts from hits in four SMT layers.

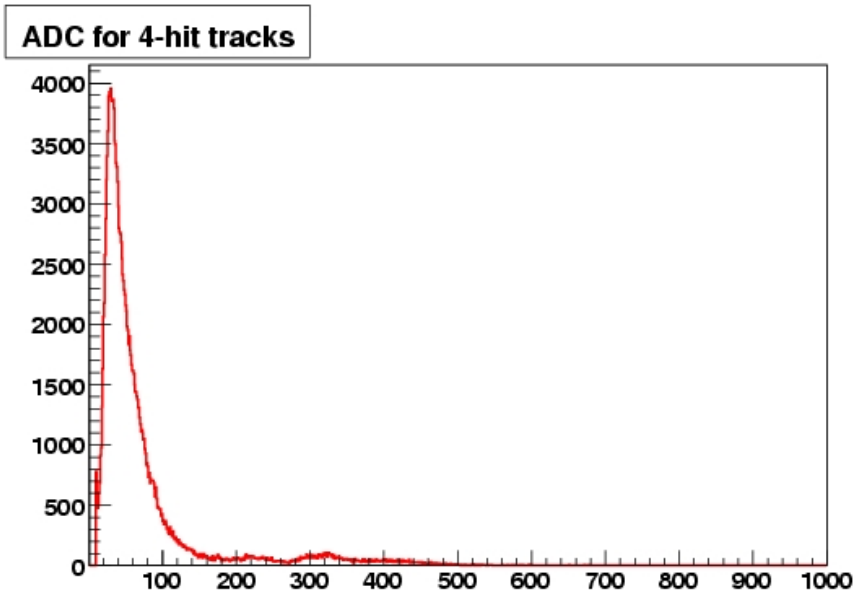

Figure B.1: The total energy deposit measured in ADC counts in four SMT layers.

A new 3-bit number is defined as the "slowness" of a particle, which stands for how slow it travels. The larger the value of the slowness, the slower the particle moves. The slowness has to

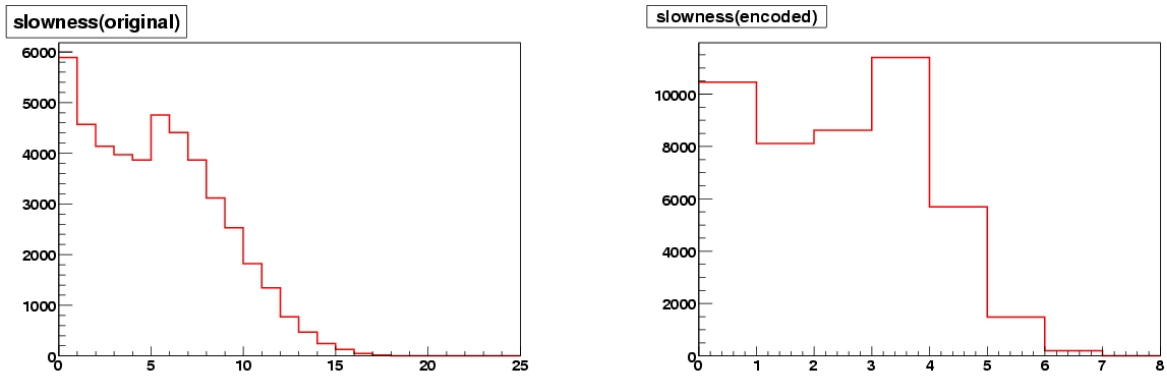

(a) (b)

Figure B.2: The total energy deposit in the SMT layers. (a) The original sum of the slowness, and (b) the encoded sum of the slowness.

be a 3-bit integer, because there are only three bits left in the STT output to Level2/Level3. The procedure to calculate the slowness of each particle is the following:

1. Find the central track with SMT hits which is associated with good quality muon objects.
2. Get the energy loss in the SMT for each track and convert it to an integer with value [0, 7].
3. Select the energy loss measured in three (out of four) SMT hits.
4. Encode the total energy loss into another 3-bit integer number with value [0, 7].

The energy loss is recorded in at most four SMT layers, before the Layer 0 is installed at DØ Run IIb period. And there are at least three SMT hits measuring the energy loss. The total energy loss for the particle is summed over only three SMT hits. When there are four ADC values, we reject the one with the highest value and keep the lowest three. The total energy loss then has a value in [0, 21], which exceeds the maximum of a 3-bit integer. Hence, this number has to be converted to a final 3-bit integer between 0 and 7 with another encoding algorithm. Figure B.2 shows (a) the original sum of the slowness, and (b) the encoded one over three SMT hits.

The $Z \rightarrow \mu\mu$ MC samples are compared with the muons in the recorded real data events. Figure B.3 shows that there is some discrepancy between the distributions of the real data and the MC samples. This indicates that further smearing should be applied to the MC samples in order to better describe the detector responses.

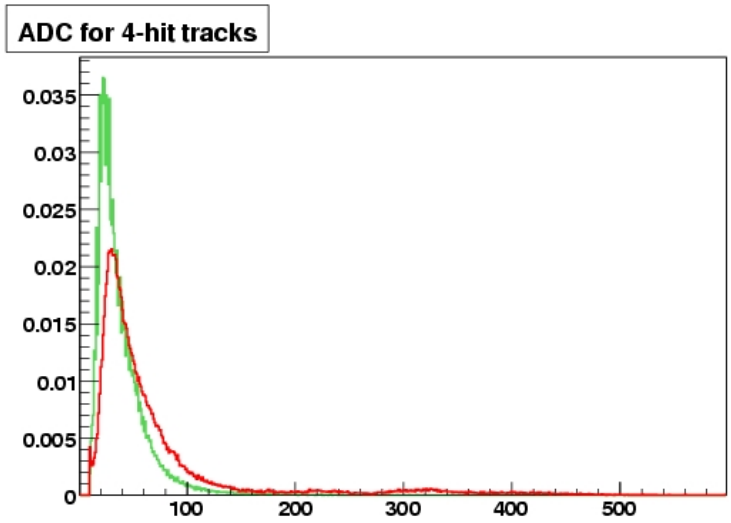

Figure B.3: Comparison of the energy deposit distributions of the $Z \rightarrow \mu\mu$ events in the real data (red line) and the MC samples (green line).

Several smearing methods have been tested. The main goal is to reduce the discrepancy between the data and the MC samples. Figure B.4 compared two different smearing methods, the Gaussian smearing and the Uniform smearing. The Gaussian smearing agrees well with the real data in the high ADC count region; the Uniform smearing is a better description in the low ADC count range. The Gaussian smearing is chosen for continuing analysis.

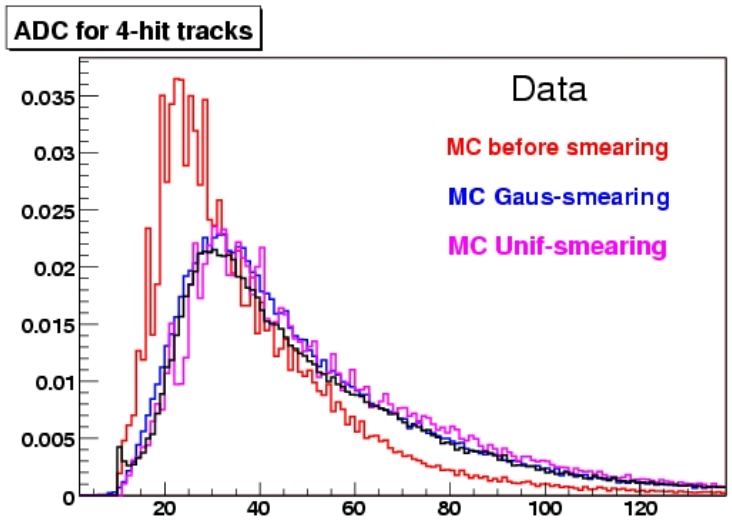

Figure B.4: The comparison of the energy deposit distributions of the $Z \rightarrow \mu\mu$ events in the real data (black line), the unsmeared MC samples (red line), the smeared MC samples with the Gaussian distribution (blue line), and the smeared MC samples with the Uniform distribution (pink line).

The CMSP samples are generated with the customized D0STAR. Since the stopping power is highly dependent on the velocity of the particle, the single CMSP samples with fixed velocity (or $\beta = v/c$) are generated with different particle mass.The slowness of each track is encoded as stated above into a 3-bit integer number between 0 and 7. The CMSP signal samples are generated with 100 GeV mass and $\beta = 0.4,\ 0.5,\ 0.6,$ and 0.7. The $Z \rightarrow \mu\mu$ MC events are compared with the CMSP signal samples as shown in Fig B.5.

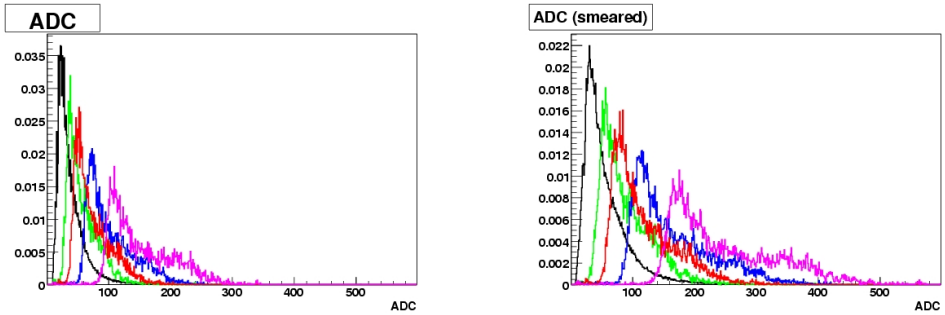

(a) (b)

Figure B.5: Comparison between the $Z \rightarrow \mu\mu$ MC samples and the single stau events of 100 GeV mass with different β. (a) The ADC distributions without any smearing to the MC samples, and (b) the distributions after applying the Gaussian smearing. The $Z \rightarrow \mu\mu$ events are shown in black, with $\beta = 0.7$ in green, $\beta = 0.6$ in red, $\beta = 0.5$ in blue, and $\beta = 0.4$ in pink.

The encoded slowness is compared and shown in Fig. B.6. We observe that the slowness distributions are very different between the $Z \rightarrow \mu\mu$ events and the stau signals. The large separation between the normal muons and the staus indicates the possibility of a selection criteria on the slowness.

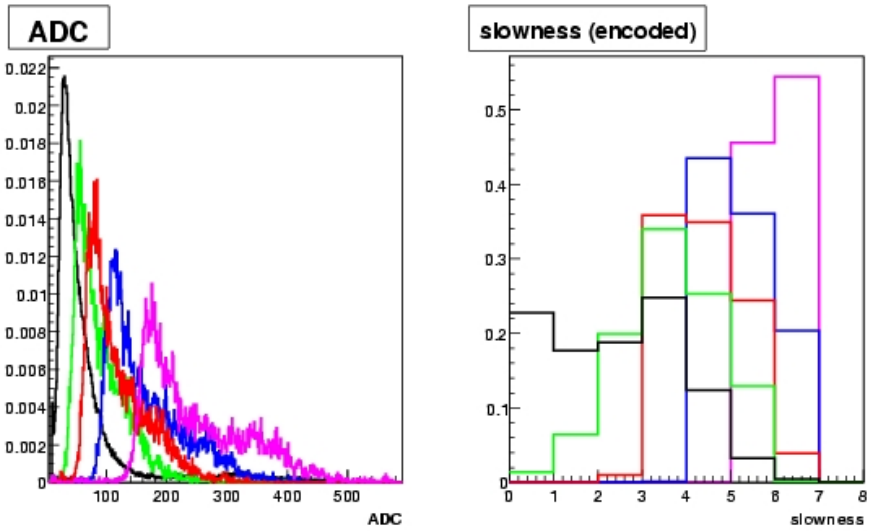

Figure B.6: Comparison between the $Z \rightarrow \mu\mu$ MC samples and the smeared single stau events of 100 GeV mass with different β. The $Z \rightarrow \mu\mu$ events are shown in black, with $\beta = 0.7$ in green, $\beta = 0.6$ in red, $\beta = 0.5$ in blue, and $\beta = 0.4$ in pink.

An efficiency study has been done on a slowness cut. A cut on the slowness can help classify the CMSP signal particles from the normal muons. The cut efficiency is defined as the number of particles greater than the cut value divided by the total number of the particles associated with a central track containing the SMT hits.The efficiencies of different cut values are shown in Fig. B.7. This efficiency comparison shows the expected features of the slowness cut, which are to effectively reject the normal muons while keeping the CMSP signals at high efficiency.

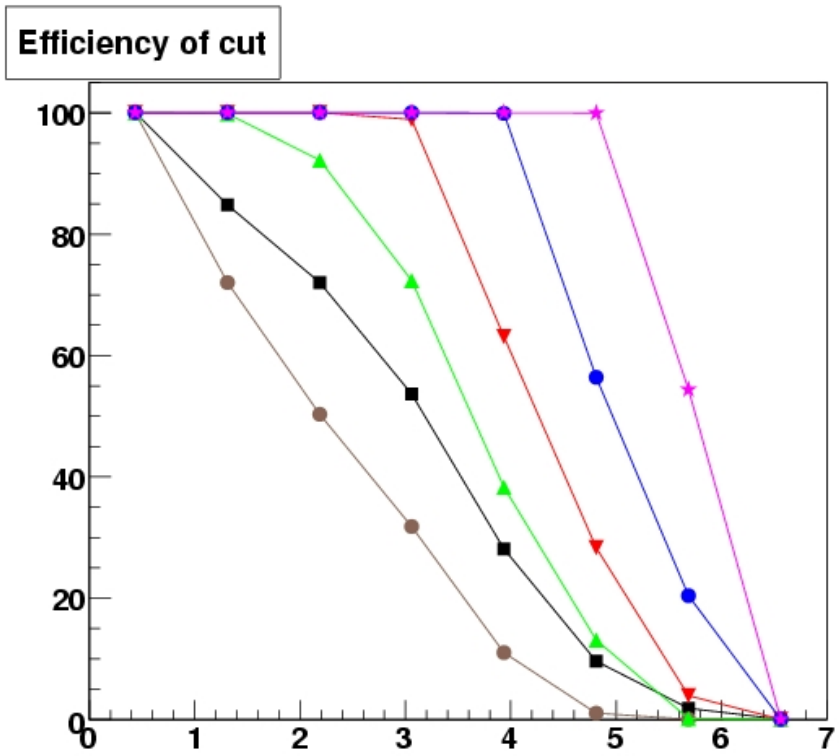

Figure B.7: The efficiency of the slowness cut for the $Z \rightarrow \mu\mu$ data events, $Z \rightarrow \mu\mu$ MC samples and single stau events of 100 GeV mass with different β. All MC samples are smeared with the Gaussian function. The $Z \rightarrow \mu\mu$ data events are shown in black; the $Z \rightarrow \mu\mu$ MC samples are in dark brown; the green line is for $\beta = 0.7$; the red line is for $\beta = 0.6$; the blue line is for $\beta = 0.5$; and the pink line is for $\beta = 0.4$.

The study in this Appendix has proved that the energy loss, dE/dx, in the SMT system is a powerful tool for identifying the particle type. Also, the new variable, slowness, can be used for developing additional triggers at L2 and L3.

Appendix C

Cross study

Further study was performed on the limit calculators using the same likelihood discriminant function. The main purpose of this study is to certificate the DØ Bayesian limit fitting code.

In ROOT, there is also a class, "TLimit", defined to compute the 95% C.L. limits [51, 77]. TLimit is an algorithm that uses the likelihood ratio semi-Bayesian method. It contains three classes, "TLimitDataSource", "TLimit", and "TConfidenceLevel".

TLimitDataSource is the input format for TLimit, which is a set of histograms. The histograms are one-dimensional histograms with float-type values as input, and are defined as "TH1F" in ROOT. Signal, background and data histograms are wrapped and formed into a channel. Different systematic uncertainties can be added as additional channels individually.

TLimit is the actual algorithm. After taking the TLimitDataSource, a set of Monte Carlo experiments are run and the limits are computed. The inputs are fluctuated according to the systematic channels if necessary.

The output is in the form of TConfidenceLevel. After the time-consuming program completes, the output is stored in a TFile for further processing. A set of values (CL_s, CL_b, CL_{s+b}, ...) is generated.

In our study, the 95% confidence level cross limits on the pair production cross-section were calculated using the CL_s method for each stau mass point.

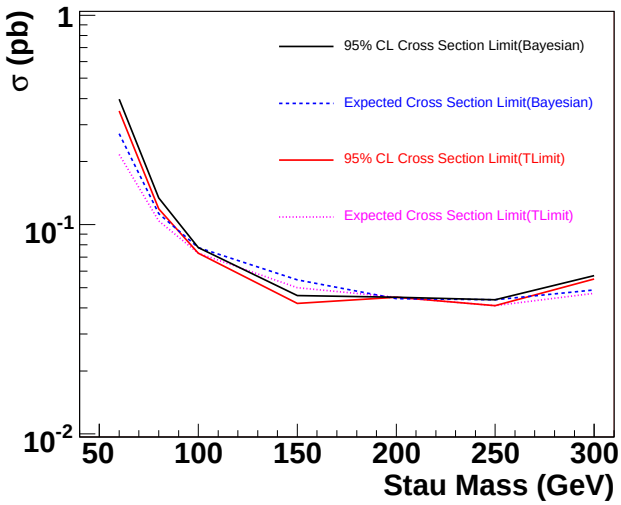

Figure C.1: The 95% Confidence Level limit on the cross-section of the pair production comparison between the CL_s method and the Bayesian limit calculator of both expected and observed limits for all stau mass points.

The background estimation, signal acceptance and the uncertainties are the same as used in the Bayesian limit calculator. Both the expected and observed limits are calculated, and are shown in Fig. C.1 . The limits obtained by the two methods give consistent results.